Investigation of Nanoparticles and Interface Effects on Organometal Halide Perovskite Solar Cells Fabricated by Wet Process

INVESTIGATION OF NANOPARTICLES AND INTERFACE EFFECTS ON ORGANOMETAL HALIDE PEROVSKITE SOLAR CELLS FABRICATED BY WET PROCESS

A DISSERTATION
SUBMITTED TO THE DIVISION OF MATERIAL SCIENCE
IN PARTIAL FULFILLMENT OF THE REQUIREMENTS FOR THE
DEGREE OF DOCTORATE IN PHILOSOPHY

by

MD. SHAHIDUZZAMAN
REGISTRATION NO.: 1323132008
ADVISOR: DR. TETSUYA TAIMA

GRADUATE SCHOOL OF NATURAL SCIENCE & TECHNOLOGY
DIVISION OF MATERIAL SCIENCE
KANAZAWA UNIVERSITY
KAKUMA, KANAZAWA, JAPAN
SEPTEMBER, 2016

INVESTIGATION OF NANOPARTICLES AND INTERFACE EFFECTS ON ORGANOMETAL HALIDE PEROVSKITE SOLAR CELLS FABRICATED BY WET PROCESS

Ph.D. THESIS

by

MD. SHAHIDUZZAMAN

GRADUATE SCHOOL OF NATURAL SCIENCE & TECHNOLOGY
DIVISION OF MATERIAL SCIENCE
KANAZAWA UNIVERSITY
KAKUMA, KANAZAWA, JAPAN

SEPTEMBER, 2016

Dissertation

Investigation of Nanoparticles and Interface Effects on Organometal Halide Perovskite Solar Cells Fabricated by Wet Process

Graduate School of Natural Science & Technology

Kanazawa University

Major Subject: Division of Material Science

School Registration No.: 1323132008

Name: Md. Shahiduzzaman

Chief Advisor: Associate Professor Tetsuya Taima

Abstract

Hybrid organometal halide perovskites such as methylammonium lead iodide ($CH_3NH_3PbI_3$) are attracting considerable attention as energy-efficient light absorber materials for photovoltaic applications owing to their solution processability, tunable bandgap, strong absorption coefficients, and cost effectiveness. The control of morphology and crystallization are the main challenges encountered in perovskite-based thin films and affect the quality of the resulting film. We have approached new method to tune morphology of perovskite and applied interlayer control method in order to improve power conversation efficiency (PCE) of perovskite solar cells. This thesis presented two different approaches, which are aimed at contributing to the development of planar heterojunction (PHJ) perovskite solar cells.

(1) We prepared $CH_3NH_3PbI_3$ nanoparticles (NPs) for the first time using a simple spin-coating method by incorporating a small amount (1~10 wt %) of an ionic liquid (IL) 1-hexyl-3-methylimidazolium chloride in 25 wt % solution of $CH_3NH_3PbI_3$ in N,N-dimethylformamide (DMF) onto the compact-TiO_x/ITO substrates to control size and shape of NPs. Compact-TiO_x films were prepared by chemical bath deposition (CBD) according to the procedure described by Kuwabara *et al.* (*Organic electronics* 11, **2010**, 1136). The $CH_3NH_3PbI_3$ NP thin films were uniform and free of pin holes, and the excellent morphology was due to the addition of IL. The small-sized $CH_3NH_3PbI_3$ NPs (~350 nm) with superior optical absorption properties have been obtained with 3 wt % of IL in the medium, as compared to the other compositions with wt % of 1, 7 and 10. As a result, a maximum PCE of 2.81% was obtained with the solar cell using 3 wt % of IL in a solution. The effect of viscosity of varying ILs have also been investigated. Low viscosity of ILs together with completely dissolve in $CH_3NH_3PbI_3$ solution were playing a significant role in controlling the morphology of resulting NPs.

The preliminary results are promising for the fabrication of PHJ solar cells based on $CH_3NH_3PbI_3$ NPs using a device configuration of ITO/TiO_x/ $CH_3NH_3PbI_3$ NPs/ spiro-OMeTAD/Ag. We also expect that the results will open a pathway towards a better understanding for the fabrication, modification and enhancement of the performance of

solar cells with $CH_3NH_3PbI_3$ NPs. In the present case, we assume a hindering effect followed by impact on charge dissociation, transport, and/or recombination on the device performances due to the residual IL content remained on the $CH_3NH_3PbI_3$ NP films.

(2) Taima *et al.* (*Jpn. J. Appl. Phys*. 54, **2015**, 08KF05) have developed interlayer control method and employing it in efficient polymer based organic solar cells. Considering this, I have applied this method to PHJ perovskite solar cells.

We fabricated PHJ type perovskite solar cells with enhanced efficiency by introducing fullerene (C_{60}) interlayers with thicknesses of 0, 3, 7 and 10 nm between air-stable amorphous compact TiO_x and $CH_3NH_3PbI_3$ layers. The modified morphology obtained by inclusion of C_{60} improved the surface energy properties of the cells in terms of enhanced photocurrent. Atomic force microscopy (AFM) verified the correlation between the surface energy and phase morphology of the PHJ solar cells. The introduction of a C_{60} interlayer between $CH_3NH_3PbI_3$ and TiO_x layers increased the content of photogenerated charge carrier sites, as well as lowering the accumulation and trapping of photogenerated charges at the TiO_x interface. The optimum thickness of C_{60} interlayer was 7 nm, for which a maximum PCE of 9.51% was obtained.

Keywords: Nanoparticles; Ionic liquid; Spin-coating method; Organometal halide perovskite; $CH_3NH_3PbI_3$; Interlayer; Fullerene (C_{60}).

Acknowledgements

I wish to express my indebtedness, sincere appreciation and deepest sense of gratitude to my respected supervisor Dr. Tetsuya Taima, Associate Professor, Institute for Frontier Science Initiative (InFIniti), Kanazawa University, Japan for his highly valued supervision, solemn instruction, constructive criticism, valuable suggestions and constant encouragement during the entire period of this research work and in the preparation of this dissertation.

I cherish the desire to thank Dr. Kohshin Takahashi, Professor, Graduate School of Natural Science and Technology, Kanazawa University, Japan for inspiring me to do very hard work on research during my doctoral study.

I accord my heartily reverence to Dr. Takayuki Kuwabara, Associate Professor, Graduate School of Natural Science and Technology, Kanazawa University, Japan for his whole-hearted co-operation, encouragement and enthusiastic suggestion throughout my research work.

I would like to acknowledge to Dr. Makoto Karakawa, Associate Professor, Institute for Frontier Science Initiative (InFIniti), Kanazawa University, Japan for his inspiration and co-operation.

I express my sincere gratitude to the former and current members of the Taima and Takahashi Lab for their support and sharing with me the studying time in the lab.

I would like to thank Dr. Mahabubur Rahman for his kind advice and inspiration of my research of the doctoral program.

My thanks will go to Dr. Mizanur Rahman for his encouragement and advice from the beginning of my research in JAPAN.

I highly acknowledge Dr. Ismail Md. Mofizur Rahman for his kind support and help during my doctoral study.

I am especially indebted to my wife Nayeema Afroz Sultana for her tireless help and heartiest co-operation that kept and keeping me focused to the objective.

I also would like to thank my parents, parents-in-law, brothers and sisters for their endless love and understanding for all hard and happy moment of my life.

In fine, all praises go to Almighty Allah, the omniscient and the most merciful.

Md. Shahiduzzaman
September 2016

Dedicated to

My Parents, parents-in-law, and beloved wife

Table of Contents

Abbreviation and Symbol

Abbreviation

$CH_3NH_3PbI_3$	Methylammonium lead iodide
PHJ	Planar heterojunction
NP, NPs	Nanoparticle, Nanoparticles
nm	nanometer
IL	Ionic liquid
wt%	Weight percent
DMF	N,N-dimethylformamide
CBD	Chemical bath deposition
PCE	Power conversion efficiency
Spiro-OMeTAD	2,2',7,7'-tetrakis(N,N-di-p-methoxyphenylamine)-9,9'-spirobifluorene
CO_2	Carbon dioxide
OPV	Organic photovoltaic
DSSCs	Dye sensitized solar cells
HTM	Hall transporting material
ETA	Electron transporting activity
ITO	Indium tin oxide
ZnO	Zinc oxide
CuI	Cupper iodide
CuSCN	Copper (I) thiocyanate
NREL	National renewable energy laboratory
ASTM	American society for testing and materials
AM0	Air Mass Zero
AM1.5G	Reference solar spectral irradiance of ASTM G-173-03
EQE	External quantum efficiency

IQE	Internal quantum efficiency
IPCE	Incident photon–to–electron conversion efficiency
SEM	Scanning electron microscopy
NW, NWs	Nanowire, Nanowires
MAI	Methylammonium iodide
IPA	Isopropanol
$MAPbI_3$	Methylammonium lead iodide
TiO_2	Titanium dioxide
3D	Three-dimensional
HRTEM	High resolution transmission electron microscopy
FFT	Field effect transistor
UV-Vis	Ultraviolet-visible
Al_2O_3	Aluminium oxide
AFM	Atomic force microscopy
IoT	Internet of Things
HMImCl	1-hexyl-3-methylimidazolium chloride
PbI_2	Lead iodide
$TiOSO_4$	Titanium (IV) oxysulfate
H_2O_2	Hydrogen peroxide
EDX	Energy-dispersive X-ray spectroscopy
XRD	X-ray diffraction
FTIR	Fourier Transform Infrared Spectroscopy
IRRAS	Infrared Reflection Absorption Spectroscopy
RMS	Root mean squire
RT	Room temperature
[TBAM][CL]	Tetrabutylammonium chloride
[BMIM][CL]	1-benzyl-3-methylimidazolium chloride

[AMIM][CL]	1-allyl-3-methylimidazolium chloride
[EMIM][AC]	1-ethyl-3- methylimidazolium acetate
[EMIM][TFSI] imide	1-ethyl-3- methylimidazolium bis (trifluoromethanesulfonyl)
[DMIM][CL]	1, 3-didecyl-2-methylimidazolium chloride
$[P_{6,6,6,14}][DCA]$	Trihexytetradycyl phosphonium dicyanamide
PCBM	[6,6]-phenyl-C_{61}-butyric acid methyl ester
LUMO	Lowest unoccupied molecular orbital
HOMO	Highest occupied molecular orbital
C_{60}	Fullerene
FF	Fill factor

Symbol

µL	Microliter
Pa	Pascal
J-V	Current densities versus voltage
J_{sc}	Short-circuit current density
V_{oc}	Open-circuit voltage
η	Viscosity
ηIL	Viscosity of IL
x_c	Mole fraction of DMF
M	Molar
h	Hour
eV	Electro volt
(**θ**) / °	Contact angle

mA/cm^2	Milliampere /square centimeter
$mJ\ m^{-2}$	Mega joule per square metre
J_{MPP}	Voltage maximum power point
V_{MPP}	Current maximum power point

List of Figures

List of Tables

Chapter One:
General Introduction to Organometal Halide Perovskite Solar Cells

"I'd put my money on the sun and solar energy. What a source of power! I hope we don't have to wait until oil and coal run out before we tackle that."

- Thomas Edison, March 1931[1]

Energy is taken into account to be the blood of the planet owing to the actual fact that all activities of physical object require energy. There are two types of energy sources, including long run energy (eternal energy) such as solar energy or earth heat, and the other created from alternative energy and preserve in biomass and endured a chemical and physical transition like charcoal, petroleum, fossil fuel…These all energy sources will be ready to use subsequently, but it can be expected to run out quickly in the long run at the present demand of energy. Moreover, using these energy sources continuously leads to the CO_2 emission that damages the surroundings and sustainable development. Therefore, considering sustainable environment, a replacement strategy and research should be devoted to solve the energy and environmental issues. All over the world,

researchers are doing their best to choose green energy sources broadly and practically obtainable to switch using oil and charcoal.[2, 3]

Solar cells can be used as a potentially alternative energy source that are able to directly convert the incident solar radiation into electricity, together with no noise, pollution or moving parts, making them robust, reliable, and long lasting. Solar cells provided long-duration power supply effectively for satellites and space vehicles.[4]

The majority of research on solar cells focused on silicon-based assemblies, which is used as light absorber and the charge transporter. However, the high processing costs and toxicity of the chemicals that have been involved in the preparation scheme discouraged its wide application. Although researchers are working to minimize the issues, there have been continuous efforts on developing solar cells using alternative materials, mostly using organic components, such as, perovskite and dye-sensitized solar cells (DSSCs).[5] Hybrid organometal halide perovskites exhibit considerable attention as energy-efficient light-absorbing materials for photovoltaic applications due to strong absorption coefficients, long electron-hole diffusion lengths, tunable band gap, high charge carrier mobilities, solution processable, and cost-effective.[6-9]

1.1 Perovskite and Perovskite Solar Cells

Perovskite has been considered as a calcium titanium oxide ($CaTiO_3$) mineral that named as Russian Geographical Society founder Lev Perovskiti. The general chemical formula of perovskite structure refers to ABX_3 that has the same crystallographic structure as perovskite (mineral). The large inorganic atomic cation B (positively charged

cations) occupied in the center of a cube and faces of the cube area unit engaged by a small atom X (negative charge anion).

Organometal halide perovskite solar cells devices are produced with the following combination of materials:

- A = Organic cation - methylammonium $(CH_3NH_3)^+$
- B = Inorganic cation - lead (Pb^{2+})
- X_3= Halogen anion – chloride (Cl^-)/ iodide (I^-)

Perovskite crystal structure is shown in Fig. 1.1.

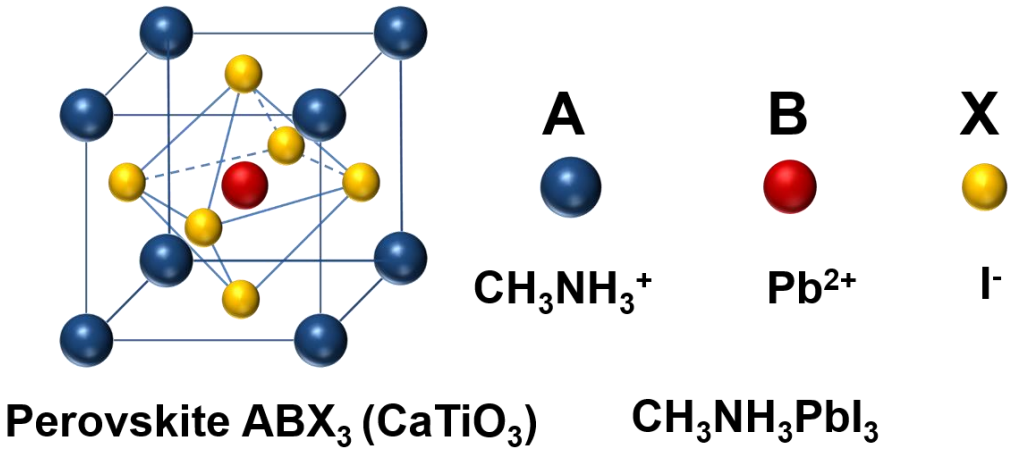

Figure 1.1. Schematic illustration of perovskite crystal structure

Among organic-inorganic perovskite-structured semiconductors, most common light-absorbing material is methylammonium lead iodide ($CH_3NH_3PbI_3$). It has high charge carrier mobility and lifetime in which allowing light-generated electrons and holes to transport far enough distances to be extracted as current, in terms of losing their energy as heat within the cell.[10]

1.1.1 Working principal of perovskite solar cells

Figure 1.2 present the schematic illustration of the working principle of a perovskite solar cells. In the case of following perovskite solar cells, electron transporting layer and hole transporting layer can be referred as ETL and HTM, respectively. Indium tin oxide (ITO)-patterned glass substrates are used as a conducting transparent electrode. Gold (Au) is also used as a contact electrode.

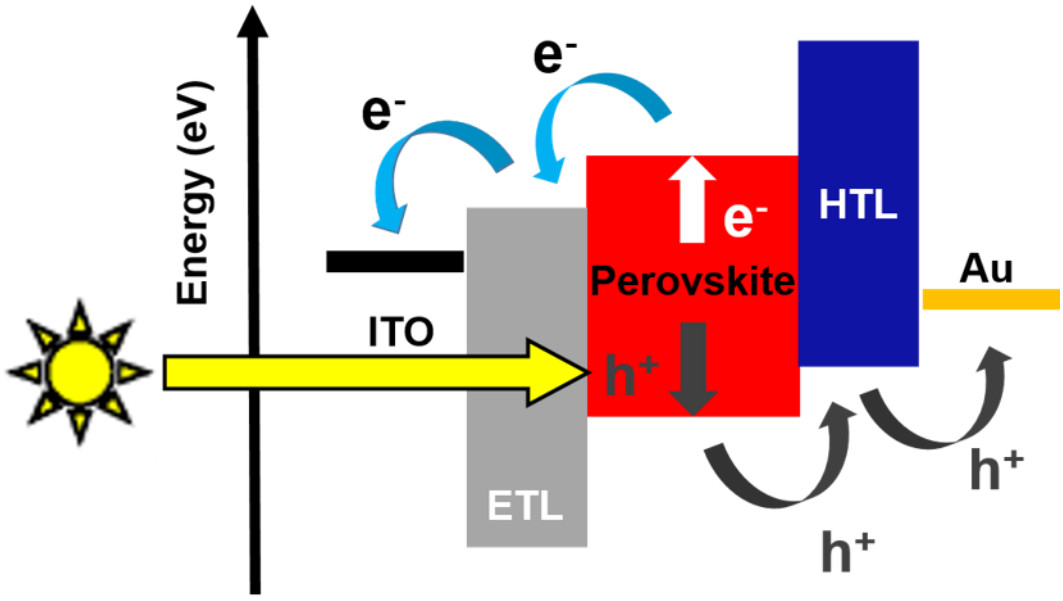

Figure 1.2. Schematic of the working principle of a perovskite solar cells

Working principle of perovskite solar cells consist four steps: light absorption, charge separation, charge transport, and charge collection. Light travelling through conducting transparent electrode onto a perovskite layer (photosensitive layer) to generate excitations named as electron-hole pairs (e^{-}/h^{+}). The charged molecules (electron-hole) diffuse and separate through the charge-conducting layers to their corresponding electrodes, thus producing electricity. Organometal halide perovskite

($CH_3NH_3PbI_3$) exhibits itself both electron and hole properties. Hence, perovskite solar cells can be fabricated both as p-n and p-i-n junction. Perovskite solar cells are usually involved with two structures such as mesoporous and planar heterojunction. Mesoporous metal oxide (e.g., Al_2O_3, TiO_2) layer usually is used to collect more electrons. High temperature processing is required to fabricate mesoporous layers. On the contrary, planar heterojunction cells have attracted more interest for flexible solar cells since their fabrication does not require high-temperature process.

1.1.2 Notable achievements to date

The efficiency of perovskites as a light-absorber material with 3.8%[11] power conversion efficiency (PCE) was first reported by Kojima in 2009. Park *et al.*[12] have further improved the PCE to 6.5% in 2011. Park, Grätzel and colleagues reported perovskite solar cells with a PCE of 9.7%[13] was fabricated by introducing spiro-OMeTAD as a hole transporting material (HTM). Almost at the same time, Snaith *et al.*[14] also reported perovskite solar cells together with spiro-OMeTAD. The combined efforts of Seok and Grätzel group[15] reported PCE of 12% using nanoporous TiO_2 scaffolding. The further enhanced efficiency of 12.3% reported using similar structures and mixed-halide $CH_3NH_3PbI_{3-x}Br_x$ perovskites[16]. Improved morphology was obtained using two-step method and TiO_2 scaffolding by Grätzel group.[17] Snaith *et al*. showed similar results without using TiO_2 scaffolding. Liu *et al.* reported planar heterojunction solar cells with efficiency of 15.7% by employing ZnO nanoparticle layer[18] as electron collection layer (ECL). Notable perovskite solar cells performance has also been achieved by using inorganic HTM such as CuI[19] and CuSCN.[20] An efficiency of 15.6%[21] has been obtained

by employing low-temperature processed ECL of graphene/TiO_2 nanocomposites. Furthermore, efficiency of 15.9%[22] has been achieved by combining tiny TiO_2 nanoparticles along with a titanium diisopropoxide bis(acetylacetonate) binder perovskite solar cells. Besides, Yang *et al*.[23] reported with a PCE of 19.3% was fabricated by employing interface engineering.

During the past few years, the encouraging discovery has been continued further to achieve a notable 22.1% conversion efficiency until the date[24], and will be expected to rise towards 25% in the near future[25]. Noticeably, the perovskites provide a promising pathway to explore next-generation photovoltaic together with higher performance of solar cells.

1.1.3 Photovoltaic efficiency records

The prompt performance enhancement of organometal halide perovskite solar cells have opened a new pathway to rising star of the photovoltaics world and showed interest to the academic research community. Figure 1.3 presented a graph that used the information from National Renewable Energy Laboratory (NREL) solar cells efficiency chart.

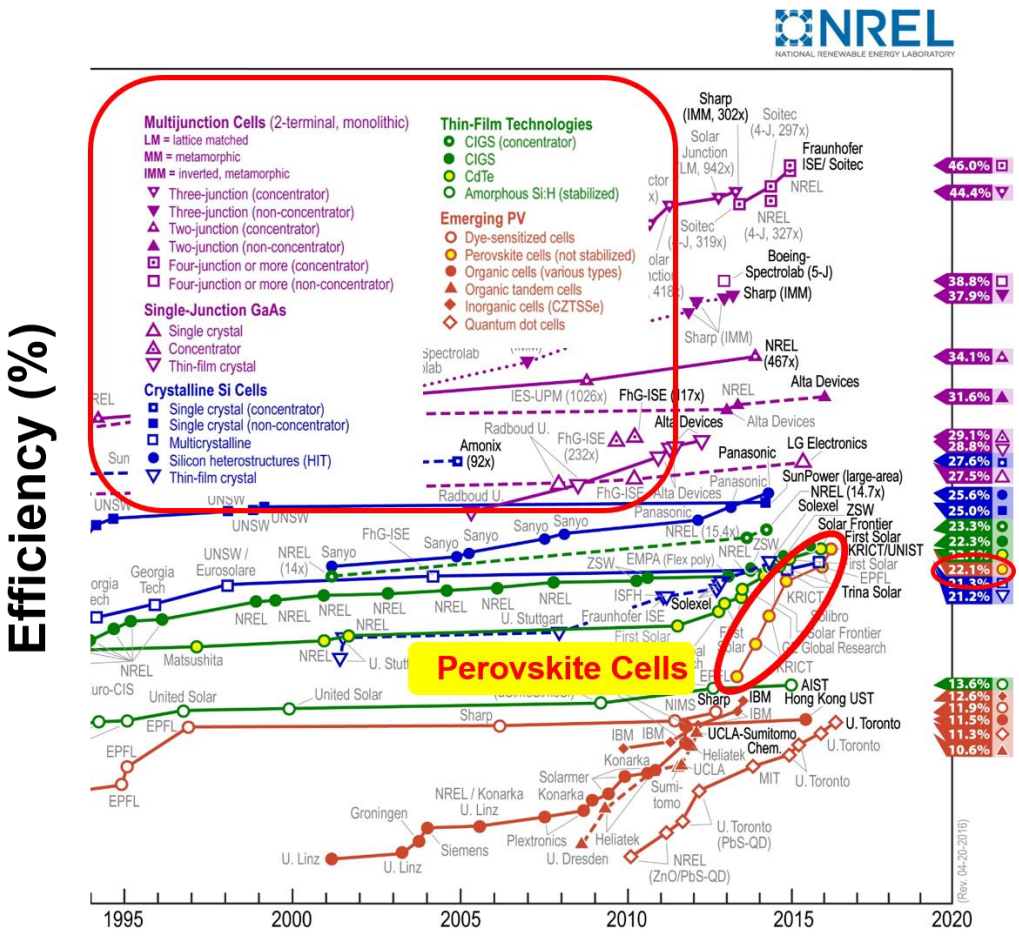

Figure 1.3. Solar cells efficiency chart

This graph showed the comparison of conversion efficiency over the recent years between perovskite solar cells and other technologies. The encouraging discovery of perovskite solar cells will be continued to rise further remarkable performances over the coming years.

1.1.4 Commercialization challenges

The present performance of perovskite solar cells showed a promising interest of multiple attempts to commercialize photovoltaic products in upcoming years. The high-performance perovskite solar cells contained a key component of lead (Pb) that could be influenced against the taking care of such products in consumer.

In terms of cost, perovskites may compete with CdTe photovoltaic thin-film solar cells. The higher-performance of perovskites have typical drawbacks together with CdTe, specifically dependence on an environmentally hazardous heavy metal. Currently, photovoltaic modules are released from the regulation of European Union on the use of Restriction of Hazardous Substances (RoHS), at least for large, fixed, professionally installed systems.

Without this exemption, CdTe solar cell modules would have no risk that met the demand of RoHS. The maximum permitted concentration of products, which is limited to 0.01% or 100 ppm for cadmium (Cd) by weight in any uniform layer. Considering the CdTe modules, perovskite modules may be promising of multiple attempts to commercialize in upcoming years because the RoHS limit on Pb in a uniform layer is ten times higher than that of Cd.

1.2 Solar Cells Characterization

1.2.1 Reference solar spectral irradiation

Solar spectrum is the most important aspects of solar cells characterization that is engaged to evaluate the performance of a photovoltaic device. Solar spectrum irradiance is standardized by the American Society for Testing and Materials (ASTM). The spectrum outside zero atmosphere is referred to as Air Mass Zero (AM0). By employing AM0, satellites and high-flying aircraft are usually characterized. The AM0 can be considered for the extraterrestrial irradiance. Figure 1.4 showed that the solar radiation spectrum.[26] The integrated spectral irradiance is 1366.1 W/m^2 for the standardized of AM0.

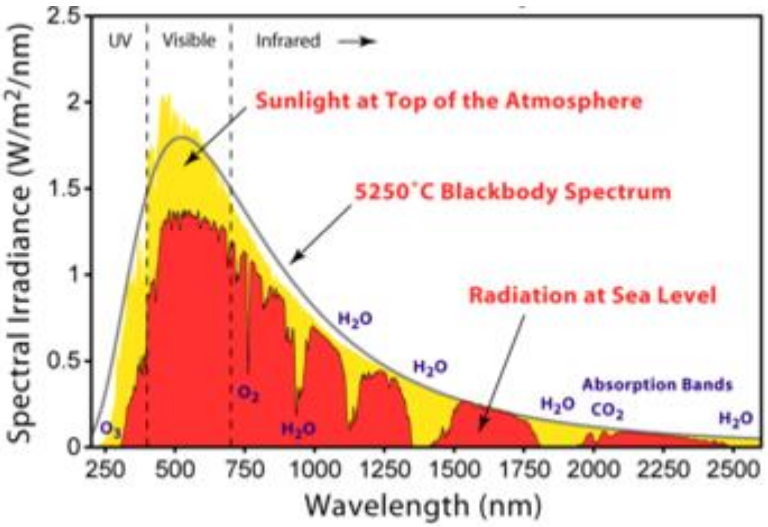

Figure 1.4. Solar radiation spectrum

Solar irradiance is reduced due to absorption and scattering processes, while passing through the atmosphere. The Earth surface receiving solar spectrum irradiance is defined by the ASTM G-173-03 named as AM1.5G. This represents the solar zenith

angle of 48.19°, which is corresponding to an Air Mass of 1.5 and for specific atmospheric conditions. The integrated spectral irradiance is 1000.4 W/m^2 for the standardized of AM1.5G.

1.2.2 Current-voltage characteristics

Current density *versus* voltage (*J*–*V*) characteristics of the photovoltaic devices are measured at AM 1.5G illumination (Fig. 1.5) in order to evaluate of the solar cells performance.

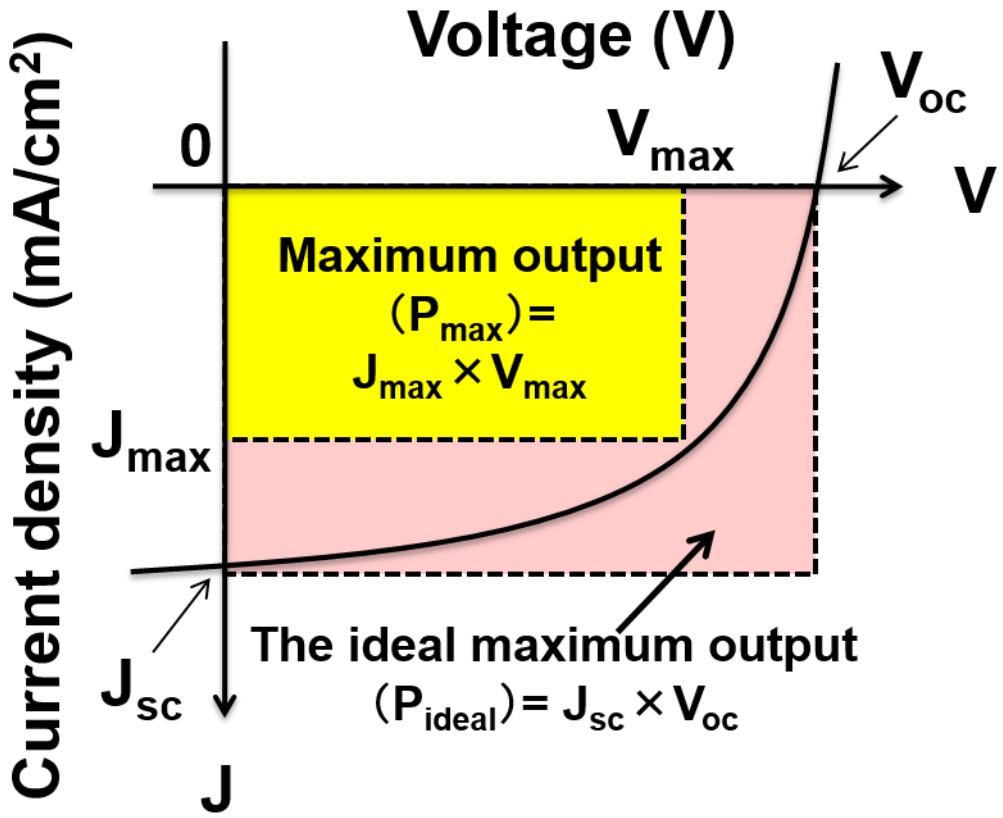

Figure 1.5. Schematic illustration of current-voltage measurement of a solar cells

The short-circuit current density (J_{sc}) is the current density through the solar cells, while the voltage of solar cells is zero ($mAcm^{-2}$). J_{sc} is directly depend on the light intensity (number of photons). The open-circuit voltage (V_{oc}) is the maximum voltage from a solar cells device, when the current is zero (V). The current density at the time of the maximum output of the element ($mAcm^{-2}$) is defined as J_{max}. The aximum output when the voltage of the device (V) is also defined V_{max}, The maximum output of the element P_{max}: $P_{max} = J_{max} \times V_{max}$ (wcm^{-2}). The energy of the incident light (AM1.5G) E = 100 ($mWcm^{-2}$). Fill factor (FF) is referred as the ratio of the maximum power of the solar cells to the product of V_{oc} and J_{sc}.

Fill factor (FF) = $J_{max} \times V_{max}/(J_{sc} \times V_{oc})$……..1.1

Power conversion efficiency (PCE) is also referred as the ration of solar-energy output from the solar cells to input energy from the sun. From the *I-V* curve, all the parameters such as J_{sc}, V_{oc}, FF, and PCE are determined.

Power Conversion Efficiency (PCE)
= P_{max}/E
= $J_{max} \times V_{max}$/E
= ($J_{sc} \times V_{oc}$) × FF/E……1.2

1.2.3 Quantum efficiency measurements

The term quantum efficiency (QE) of a solar cell is measured in terms of a function of wavelength and represents the fraction of an incident photons that converted into

electrons of the external circuit. Two types of QE of a solar cells are existed: the external quantum efficiency (*EQE*) and the internal quantum efficiency (*IQE*). The *EQE* is also defined as the incident photon-to-electron conversion efficiency (*IPCE*), considering the number of photons that are emitted from the solar simulator and that hit the photosensitive area of the solar cells. *IPCE* value depends on the absorption of light (photons) and the collection of charge carriers. When a photon has been absorbed and has generated an electron-hole (e^-/h^+) pair, these charge carriers will be separated and collected at the interface of the junction. Charge recombination can be avoided to have good devices. Charge recombination influences a drop in *IPCE*. The *IPCE* value is calculated with the known photon flux J_0 of the solar simulator according to Equation 1.3, where J_{sc} is the short-circuit current density and *e* the elementary charge.

$$IPCE = J_{sc}/eJ_0 \quad \text{.....1.3}$$

1.3 Review on Perovskite Nanoparticles Solar Cells

Hybrid organometal halide perovskite solar cells have made an impressive improvement in the last couple of years, mainly by their high PCE over 22% until the date. Perovskites have also shown potential for application in various fields like superconductors,[27] sensors,[28] fuel cells,[29] ferroelectric,[30, 31] photocatalysis,[32] batteries,[33, 34] and thermoelectrics.[35] Semiconductor nanostructures have opened the door for the utilization of nanocrystalline pigments as enticing light-weight harvesters, that have the subsequent characteristics: a) The nanostructure of the light absorbent material layer possesses sub-wavelength features attributable to quantum size effects, which results in

very low reflection and accumulated photon absorption and provides higher cell efficiency without the necessity for additional antireflection coatings; b) The large surface areas of nanotextured materials permit efficient energy conversion and charge–carrier recombination.[36] Among semiconductive materials, low-dimensional layered compounds are intensely investigated as a promising candidate for organic–inorganic-based perovskites.[37] Complex-shaped perovskite nanoparticles (NPs) is one-dimensional (nanowires, nanotubes, and nanorods), two-dimensional (nanodiscs, nanoplatelets, and nanosheets), or alternative complicated nanostructures shapes including rod-sheet heterogeneous NPs, for example.

Up to now, there are several reports on quantum wells,[38, 39], wires [40], and dots [41] synthesized from organic-inorganic perovskite compounds. Whereas varied synthetic approaches are used to prepare nanoscale perovskite materials, those supported chemical synthesis provide the foremost versatility in terms of the manipulation of the characteristics of individual particles, together with size, shape, and structure or surface properties.

Chemical synthetic techniques area unit advantageous for large-scale tailored production of anisotropic perovskite NPs, which may be promptly assembled into nanostructured bulk perovskite materials with highly efficient properties for practical applications. Many chemical synthetic strategies are developed to organize complex-shaped metal perovskite NPs, as well as the hydrothermal/ solvothermal techniques [42-44] and wet chemical synthesis[45] method are frequently used. On the other hand, researchers

are interested in developing thin-film perovskite materials by easy, efficient, and precise techniques as an alternate to chemical synthesis.

In this review, we would like to overview of the perovskite nanostructures based solar cells from the following aspects: perovskite nanostructures fabrication method, and their physical properties. Future outlook for perovskite nanostructures as an energy harvesters will also be briefly discussed.

1.3.1 Fabrication method of perovskite nanostructures

1.3.1.1 Spin-coating method

Spin coating is a common, cheap, simple, and precise film production method, in which a centrifugal force is used to produce uniform solution-processed thin films. Centrifugal force causes a dispersion to spread uniformly across a substrate, which is followed by evaporation of the solvent to yield a thin particle film.[46] Shahiduzzaman *et al*.[47, 48] reported the preparation of $CH_3NH_3PbI_3$ NPs for the first time using a simple spin-coating method by incorporating a small amount (1~10 wt %) of an ionic liquid (IL) 1-hexyl-3-methylimidazolium chloride in 25 wt % solution of $CH_3NH_3PbI_3$ in N,N-dimethylformamide (DMF) onto the compact-TiO_x/ITO substrates. The $CH_3NH_3PbI_3$ NP thin films were uniform and free of pin holes, and the excellent morphology was due to the addition of IL. The small-sized $CH_3NH_3PbI_3$ NPs (~350 nm) with superior optical absorption properties have been obtained with 3 wt % of IL in the medium, as compared to the other compositions with wt % of 1, 7 and 10. As a result, a maximum PCE of 2.81% was obtained with the solar cell using 3wt % of IL in a solution.

Recently, Im *et al.*[49] stated an efficient $CH_3NH_3PbI_3$ ($MAPbI_3$) nanowire (NWs) perovskite solar cells with the enhanced efficiency of 14.71% by employing two-step spin-coating technique as shown in Fig. 1.6a~d.

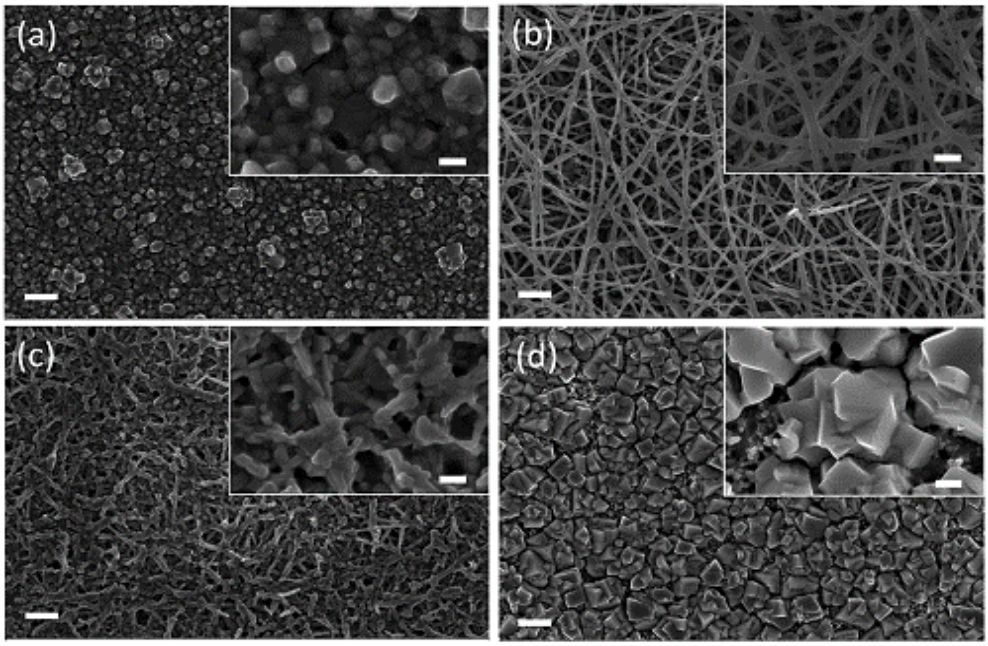

Figure 1.6. Plane-view SEM images of $MAPbI_3$ NWs formed by two-strep spin coating method using the solution of MAI in IPA (35 mg/5 mL) with (a) 10 μL of, (b) 50 μL of DMF, (c) 100 μL of DMF, and (d) without DMF. $MAPbI_3$ was deposited on a 100 nm thick mesoporous TiO_2 (diameter of about 40 nm) layer. Scale bars represent 1 μm (200 nm in insets). Reprinted with permission.[49] Copyright 2015, ACS.

As can be revealed from SEM images that the NW morphology completely depends on aprotic solvents and small quantity of DMF in IPA is confirmed to play a significant role in promoting growth of $MAPbI_3$ peroskites. The NW film horizontal conductivity was higher than that of bulk cuboid film. The charge separation and conductivity is better in NW structure. Therefore, the higher device performance is expected for the uniform NW structured film.

Moreover, Schmidt *et al.*,[50] demonstrated that the synthesis of methylammonium lead bromide ($CH_3NH_3PbBr_3$) NPs with the diameter size of 6 nm by a straightforward spin-coating technique on a quartz substrate. The NPs were prepared simply by spin-coating technique that mixture of $CH_3NH_3PbBr_3$ in the presence of oleic acid and octadecene as shown in Fig. 1.7. To isolate the NP core, the longer chain alkyl ammonium cation might play an significant role as a better capping ligand, while methylammonium cation with NPs might be helpful in the NPs based solar cell application.[51]

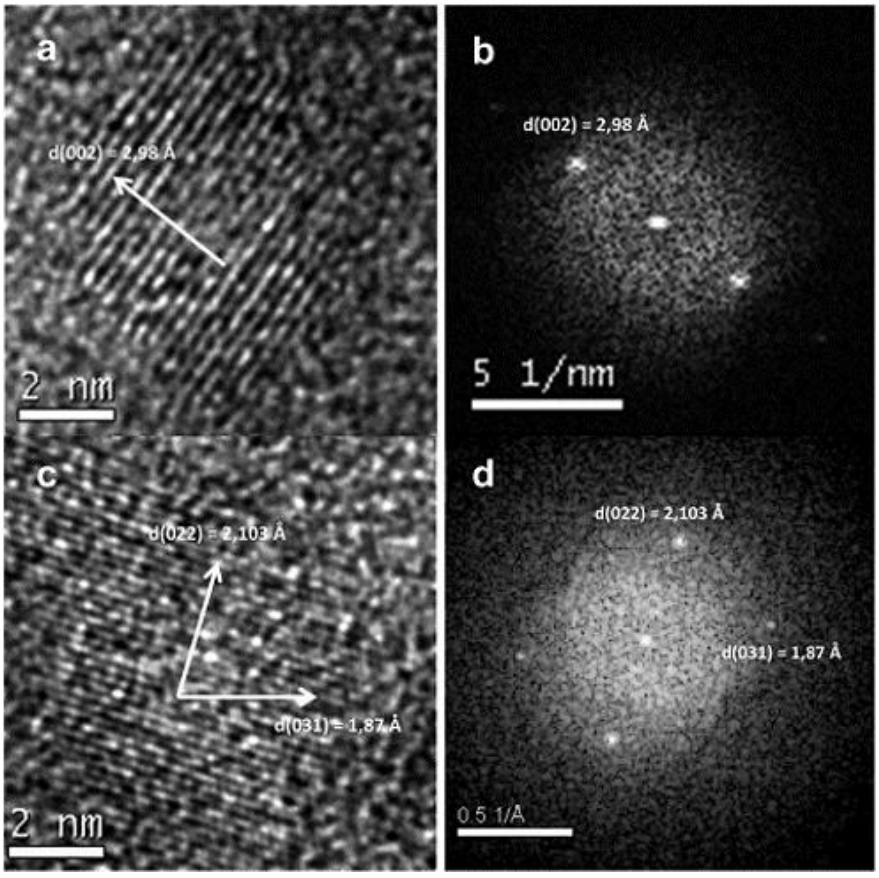

Figure 1.7. HRTEM images of individual nanoparticles from POA_2 (a and c) and their corresponding FFT analyses (b and d). Reprinted with permission.[50] Copyright 2014, ACS.

Kojima *et al.* [52] reported that the fabrication of $CH_3NH_3PbBr_3$ NPs using a simple spin-coating technique by incorporating a (1~10 wt%) of precursor solution under UV-light irradiation onto a mesoporous media. The cross-section of high-resolution SEM images of $Al_2O_3/CH_3NH_3PbBr_3$ film evidently shows $CH_3NH_3PbBr_3$ NPs with the diameter of 5 nm were deposited on spherical Al_2O_3 as shown in Fig. 1.8. The Al_2O_3 paste was spin-coated onto a quartz glass substrate and annealed at 500 ˚C for 1 h. The resulting 1 μm thick amorphous film was obtained as confirmed by SEM observations. Other semiconductor materials pastes such as SnO_2, TiO_2, and ZrO_2 were prepared for comparison by using the same method. A precursor solution (CH_3NH_3Br and $PbBr_2$ in DMF) was spin-coated on the Al_2O_3 film.

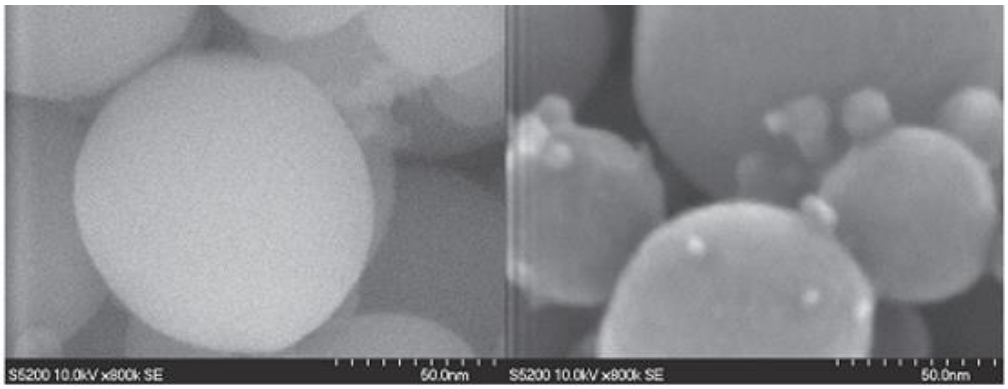

Figure 1.8. High-resolution SEM images for $CH_3NH_3PbBr_3$ nanoparticles. Left image: bare Al_2O_3 surfaces. Right image: deposited $CH_3NH_3PbBr_3$ crystals prepared with 1 wt% precursor solution. Reprinted with permission.[52] Copyright 16-093.

1.3.1.2 Slip-coating method

$CH_3NH_3PbI_3$ NWs with the diameter of 50 and 400 nm and length up to 10 μm were fabricated by a low-temperature solution process employing a slip-coating method.[53] The small amount of spin-coating solution ($CH_3NH_3PbI_3$ in DMF) was dropped onto a glass slide and covered it with a second microscope slide. The residual mixture solution formed a uniform liquid film between the glass slides (Fig. 1.9a−c). The 20 μL of the same saturated solution was applied to prepare thicker wires. Solvent evaporation from the uncovered surface resulted in an instantaneous yellow to brown-red color change. All the process were performed at room temperature.

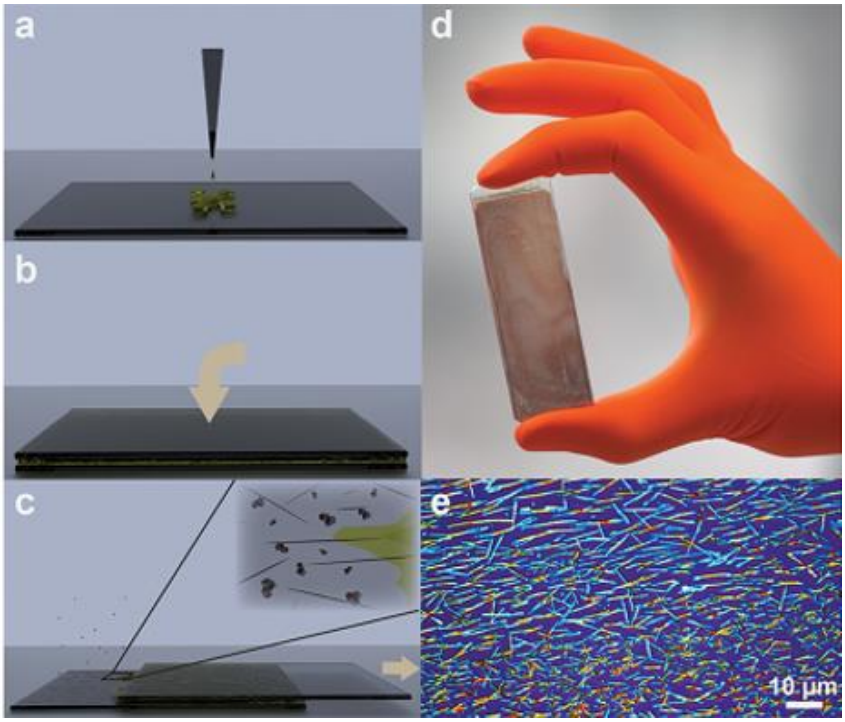

Figure 1.9. Schematic illustration of the low temperature slip-coating process for the fabrication of filiform lead-methylamine iodide perovskite thin films (a−c). Photo of the coating formed on a microscope glass slide (d). Optical microscopy image of filiform crystallites grown on SiO_2/Si substrate (e). Reprinted with permission.[53] Copyright 2014, ACS.

1.3.1.3 Chemical vapor deposition (CVD) method

Ha *et al*.[54] reported for the first time the fabrication of $CH_3NH_3PbI_3$ nano-platelets with the dimension of 5-30 µm using van der waals epitaxial growth followed by thermally intercalating methylammonium halides on muscovite mica substrate. The growth of PbI_2 nano-platelets was fabricated on muscovite mica substrate employing van der Waals epitaxy in a vapor transport chemical deposition system.[55-57] After this, as-grown PbI_2 nano-platelets are transformed to $CH_3NH_3PbI_3$ by a gas–solid hetero-phase reaction in the presence of methylammonium halide molecules. Optical and SEM images of lead halides grown on muscovite mica substrate are shown in Fig. 1.10. Besides, the resultant $CH_3NH_3PbI_3$ platelets with an electron diffusion length of over 200 nm fabricated by this promising method, which is approximately two twofold higher than the conventional solution spin-coating film.

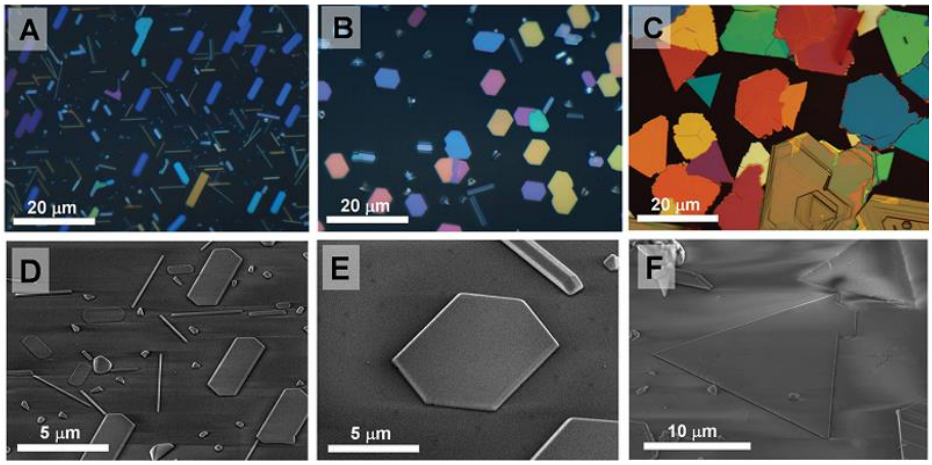

Figure 1.10. Morphological characterizations of lead halides nano-platelets as-grown on muscovite mica substrate: a) Optical (above) and SEM (below) images of lead halides: A,D: $PbCl_2$; B,E: $PbBr_2$; C,F: PbI_2. Reprinted with permission.[54] Copyright 2014, WILEY.

1.4 Conclusions

In this review, we have given an overview of the progress in nanostructured perovskite solar cells. Fabrication methods such as solution process, were shown to influence morphologies and crystal growth of the perovskite materials, thus impacting on the resultant energy conversion efficiency. The controlled morphologies of various perovskite nanostructures and their high electron mobility enable interfacial charge separation and fast electron transport which improve the charge collection efficiency in solar cells.

1.5 Future Outlook

Energy harvesting is the process of electronically capturing and accumulating energy from a range of energy sources considered wasted or unusable for any practical purpose. Semiconducting $CH_3NH_3PbI_3$ NPs are potential candidates for electronics and optoelectronics applications and can be highly efficient owing to its excellent electrical and optical properties, cost effectiveness, solution processability, tunable bandgap, and strong absorption coefficients. In order to get alternative power systems using ambient energy harvesting sources (radiant, thermal and mechanical) is a clear target for perpetual powering or recharging of the Internet of Things (*IoT*) devices as shown in Fig. 1.11. As for solar radiation, perovskite NPs based technology has the potential to increase solar conversion efficiency to more than 25 % in the very near future instead of 20 % for state-of-the-art cells. Solar energy can only be harnessed when it is daytime and sunny. Therefore, harvesting ambient thermoelectric and piezoelectric nanogenerator energy

offers alternative solution to powering IoT devices and could provide enough energy to extend the lifetime of these devices. The large surface areas of nanostructured materials allow efficient energy conversion, and charge–carrier recombination.

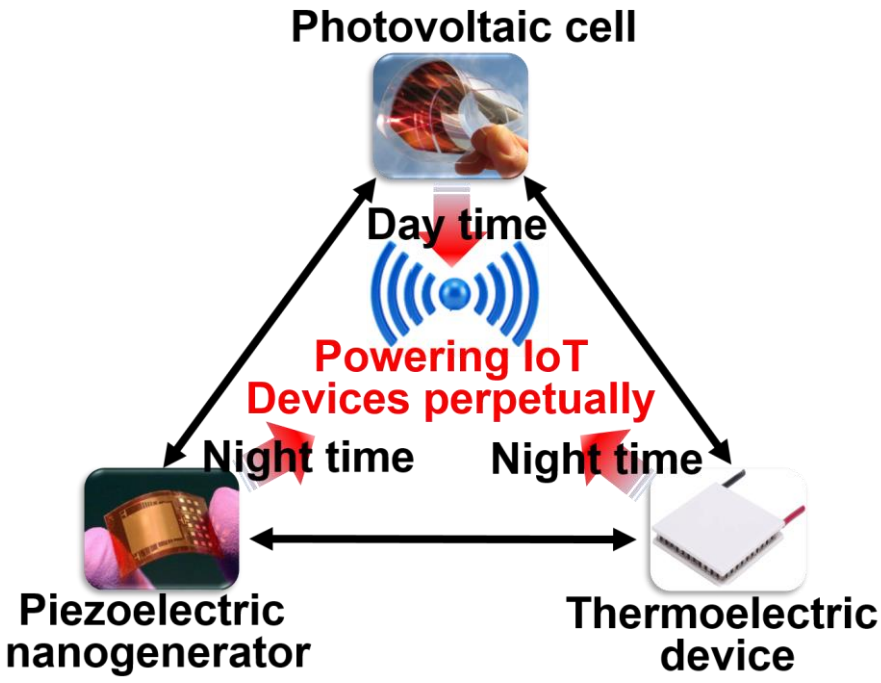

Figure 1.11. Schematic diagram of powering IoT devices at all hours.

Hence, the development of energy harvesting technologies using $CH_3NH_3PbI_3$ NPs is essential for powering the IoT devices perpetually.

<This page is intentionally left blank to indicate the chapter break>

Chapter Two:
Ionic liquid-assisted growth of methylammonium lead iodide spherical nanoparticles by a simple spin-coating method and photovoltaic properties of perovskite solar cells

The following chapter describes ionic liquid-assisted growth of $CH_3NH_3PbI_3$ spherical nanoparticles employing a simple spin-coating technique and their use in perovskite solar cells.[47]

2.1 Introduction

Perovskites show potential for application in multiple fields such as superconductors,[27] sensors,[28] fuel cells,[29] ferroelectric,[30, 31] photocatalysis,[32] batteries,[33, 34] and thermoelectrics.[35] Semiconductor nanostructures have opened the door for the use of nanocrystalline pigments as attractive light harvesters, which have the following characteristics: a) The nanostructure of the light absorber layer possesses sub-wavelength features because of quantum size effects, which results in very low reflection and increased photon absorption and provides higher cell efficiency without the need for additional antireflection coatings; b) The large surface areas of nanotextured materials allow efficient energy conversion and charge–carrier recombination.[36] Among semiconducting materials, low-dimensional layered compounds have been intensely investigated as a promising candidate for organic–inorganic-based perovskites.[37] Complex-shaped perovskite

nanoparticles (NPs) can be one-dimensional (nanowires, nanotubes, and nanorods), two-dimensional (nanodiscs, nanoplatelets, and nanosheets), or other complex shapes such as rod-sheet heterogeneous NPs. To date, there have been many reports on quantum wells,[38, 39] wires,[40] and dots[41] synthesized from organic–inorganic perovskite compounds. While numerous synthetic approaches have been used to prepare nanoscale perovskite materials, those based on chemical synthesis offer the most versatility in terms of the manipulation of the characteristics of individual particles, including size, shape, and structure or surface properties. Chemical synthetic techniques are advantageous for large-scale tailored production of anisotropic perovskite NPs, which can be readily assembled into nanostructured bulk perovskite materials with highly efficient properties for practical applications. Several chemical synthetic methods have been developed to prepare complex-shaped metal perovskite NPs, including the hydrothermal/ solvothermal method[42-44] and wet chemical synthesis.[45] However, researchers are interested in developing thin-film perovskite materials by simple, cost-effective, and precise techniques as an alternative to chemical synthesis. Spin coating is a common, cheap, simple, and precise film production method, in which a centrifugal force is used to produce uniform solution-processed thin films. Centrifugal force causes a dispersion to spread uniformly across a substrate, which is followed by evaporation of the solvent to yield a thin particle film.[46]

Schmidt *et al.*,[50] reported the synthesis of methylammonium lead bromide NPs by a simple spin-coating method on a quartz substrate with the objective of

fabricating nanostructured organic lead halide perovskite for use in the solar cells. Moreover, $MAPbI_3$ nanowires have been prepared by a low-temperature solution process using a simple slip-coating method[53] for solar cells. Control of morphology and crystallization are the main challenges encountered in perovskite-based thin films and affect the quality of the resulting film. The morphology of non-homogeneous thin films can limit device performance because of electrical shorting, or effects on charge dissociation/transport/recombination.[58-60] Therefore, an easy scalable efficient approach to fabricate homogeneous perovskite films with controlled morphology for use in perovskite solar cells needs to be developed.

In the present study, we use a simple spin-coating technique to fabricate uniformly distributed spherical NPs of $MAPbI_3$ in the presence of the ionic liquid (IL) 1-hexyl-3-methylimidazolium chloride (HMImCl), which is introduced to control morphology. HMImCl has a high boiling point, extremely low vapor pressure, high ionic conductivity, and excellent electrochemical and high thermal stability.

2.2 Experimental

2.2.1 Chemicals

Lead iodide (PbI_2, purity 98%) was purchased from Tokyo Chemical Industry (Tokyo, Japan), while titanium (IV) oxysulfate ($TiOSO_4$, purity 99.99) and 1-hexyl-3-methylimidazolium chloride (HMImCl, purity 97%) were from Sigma Aldrich (St. Louis, MO, USA). Hydrogen peroxide (H_2O_2, purity 35%) and N,N-

dimethylformamide (DMF, purity 99.5%) were supplied by Kanto Chemical (Tokyo, Japan).

2.2.2 Instrumentation

The scanning electron microscopy (SEM) and Energy-dispersive X-ray spectroscopy (EDX) (SU1510, Hitachi High-Tech, Tokyo, Japan) were used to analyse to analyse the surface morphology and elemental mapping. Surface morphology was further investigated by atomic force microscopy (AFM; SII SPI3800N, Seiko, Japan). Ultraviolet-visible (UV-Vis) absorption spectra of perovskite films were measured using an absorption spectrophotometer (U-3310, Hitachi, Tokyo, Japan). X-ray diffraction (XRD) patterns of the prepared films were measured using an X-ray diffractometer (SmartLab, Rigaku, Japan) with an X-ray tube (Cu Kα, $\lambda = 1.5406$ Å). A further analysis of the films was performed using Fourier Transform Infrared Spectroscopy (FTIR) with Infrared Reflection Absorption Spectroscopy (IRRAS) (FT/IR-6300, Jasco, Tokyo, Japan).

2.2.3 Methods

2.2.3.1 Substrate cleaning

Indium tin oxide (ITO)-patterned glass substrates purchased from Techno Print Co., Ltd. (Saitama, Japan) were treated with oxygen plasma for 20 min prior to use.

2.2.3.2 Preparation of compact-TiOx films by chemical bath deposition (CBD)

Compact-TiO_x layers were prepared in aqueous solutions of $TiOSO_4$ (1.6 g) and H_2O_2 (0.17 g) at 80 °C via CBD.[61, 62] The chemical bath was purchased from AS-One (EO-200, Tokyo, Japan). The deposited compact-TiO_x films were heated on a hot plate (ND1, AS-One, Tokyo, Japan) at 150 °C for 1 h to obtain amorphous films.

2.2.3.3 Preparation of $MAPbI_3$ NCs by spin coating

Lead iodide (PbI_2) (0.144 g) and methylammonium iodide (MAI) (0.05 g) were mixed in anhydrous DMF (615 µL) at 2.89:1 molar ratio by shaking (VMR-5R, AS-One) at room temperature (RT) for 30 min to produce a clear $MAPbI_3$ solution with a concentration of 25 wt %. PbI_2 was dehydrated under vacuum at 450 °C for 3 h prior to use. Methylamonium lead iodide (MAI) was synthesized in our laboratory. A compact-TiO_x layer (30 nm) was deposited on ITO-coated glass substrates using CBD technique as described earlier. The DMF solution of $MAPbI_3$ (25 wt%) were spin coated on top of the amorphous compact- TiOx layer at 3000 rpm. During spin coating, the color of the film changed from transparent to peach. The film was left to dry at RT for 30 min to allow slow solvent evaporation, followed by annealing on a hot plate at 100 °C for 10 min, giving a $MAPbI_3$ film with a thickness of 200 nm. The whole process was performed in an N2-filled glove box.

2.2.3.4 Preparation of $MAPbI_3$ NPs by spin coating

$MAPbI_3$ NPs were prepared using the same spin-coating technique as that described in preparation of $MAPbI_3$ NCs, except that 1 wt % HMImCl was also included in the 25 wt % $MAPbI_3$ solution in DMF.

2.2.3.5 Solar cell fabrication using $MAPbI_3$ NPs

The hole-transporting layer (HTM) was produced using 2,2′,7,7′-tetrakis (N,N-di-p-methoxyphenylamine)-9,9′-spirobifluorene (spiro-OMeTAD) via spin-coating at 4000 rpm over the $MAPbI_3$ NPs layer. The spiro-OMeTAD in chlorobenzene (0.058 M) was prepared using 4-tert-butylpridine (0.19 M), and lithium bis (trifuluoro- methylsulfonyl) imide (0.031 M), tris [2-(1H-pyrazol-1-y1)-4-tert-butylpyridine] cobalt (III) tris [bis(trifluoromethysulfonyl) imide] (5.6×10^{-3} M) as dopants.[63, 64] The films were left on a hot plate for annealing in the glove box at 70 °C for 20 min. The films were then placed in a vacuum chamber and 100 nm thick silver electrodes were deposited on the spiro-OMeTAD layer with a pressure at around 2.83×10^{-4} pa. The active device area was 4 mm^2. The current densities versus voltage (*J-V*) characteristics of the cells were analyzed under simulated AM 1.5G solar illumination with Keithley 2401 Digital Source Meter.

2.3 Results and discussion

2.3.1 Morphology, composition, structure, and absorption of $MAPbI_3$ NPs

The chemical structure of HMImCl is shown in Fig. 2.1a. We introduced 1 wt % of HMImCl to the solution of $MAPbI_3$ in DMF as a morphology-controlling additive. The IL-doped solution of $MAPbI_3$ was a homogeneous clear yellow-orange, because no aggregate or NPs were observed in it (Fig. 2.1b). The process

used to fabricate $MAPbI_3$ films with/without IL via spin coating is schematically illustrated in Fig. 2.1c.

Figure 2.2a–b reveal that the films processed without IL have incomplete surface coverage and are composed of non-uniform large crystals with a ribbon-like shape. These observations are similar to those in a previous report by Xiao *et al.*,[65] which confirms that the non-uniformity in the perovskite film was caused by the rapid evaporation of DMF during spin coating. In contrast, uniform $MAPbI_3$ NPs with a well-controlled spherical shape and an average diameter of 540 nm were observed when 1 wt% IL was added to the spin-coating solution (Fig. 2.2c–d).

This observation is further confirmed by the AFM analysis (Fig. 2.3a, b). The Root-mean-square (RMS) roughness for the perovskite films with and without IL were, 23.4 and 76.1 nm, respectively. These data support the formation of a smooth uniform NP film by inclusion of an IL in the spin-coating solution.

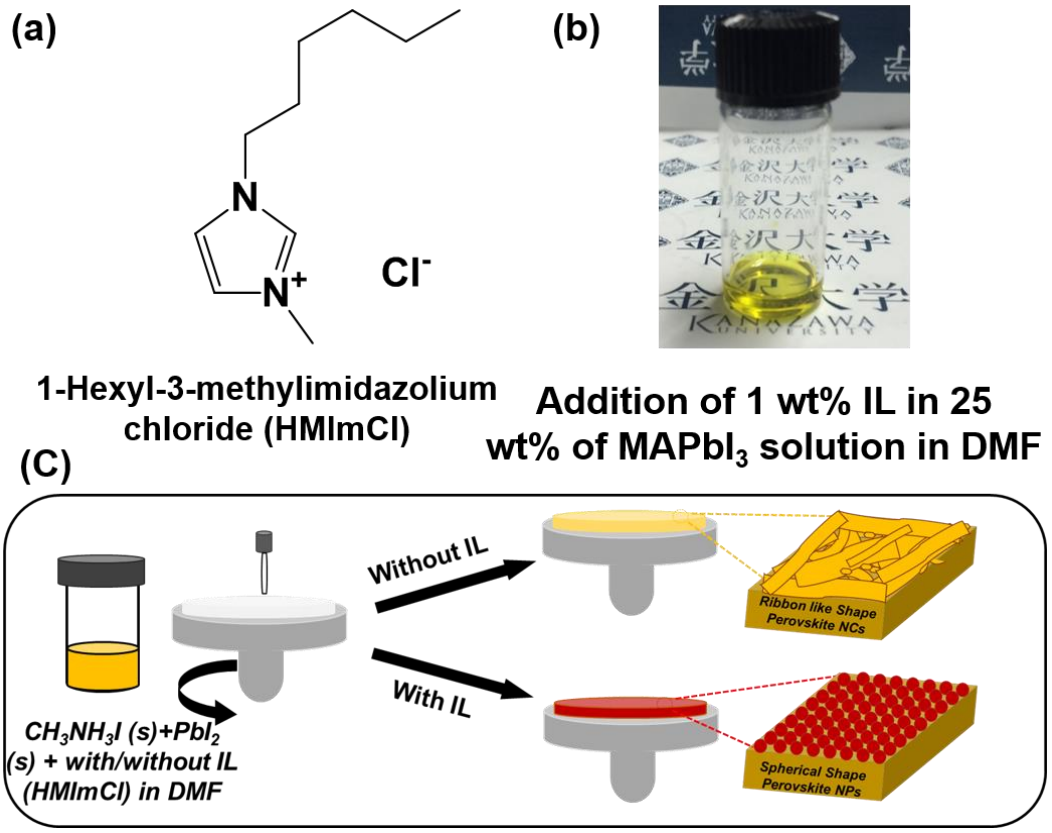

Figure 2.1. (a) Chemical structure of HMImCl. (b) Photograph of a homogeneous solution of $MAPbI_3$ in DMF containing 1 wt% IL. (c) Schematic of perovskite film formation with/without IL.

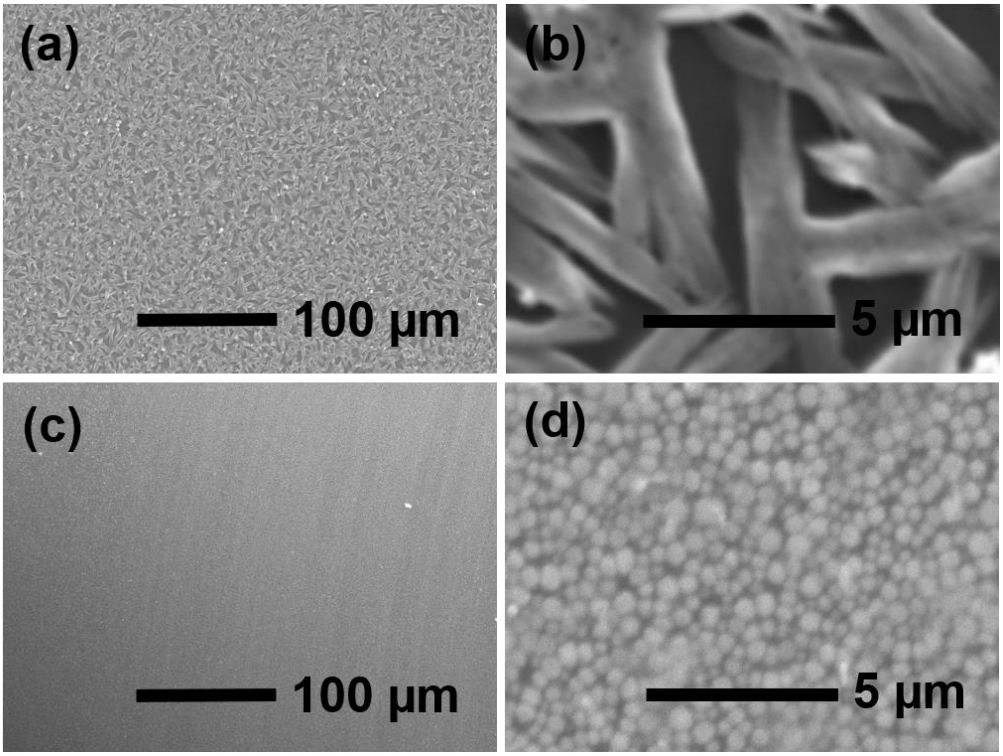

Figure 2.2. The low- and high-magnification SEM images of $MAPbI_3$ films prepared without IL (a, b) and with IL (c, d), respectively.

A uniform air-stable amorphous TiO_x layer with a thickness of 30 nm was prepared, as shown in AFM analysis (Fig. 2.3c). The RMS roughness of the amorphous film was 3.13 nm. The morphologies of the films produced at room temperature (RT) as determined by AFM (Fig. 2.3d). Figure 2.3d reveals that the small clusters formed at RT remained aggregated and was not uniformly distributed. The RMS roughness of the film was 46.5 nm as deposited film.

The EDX-mapping (Fig. 2.4a-f) was performed to address the question of whether the $MAPbI_3$ films, processed with and without IL, are composed of single or multiple phases. The technique allowed us to visualize a two-dimensional map

of the relative location of the different elements in the sample. The color intensity assists to judge the relative amount of element distributed in the surface.

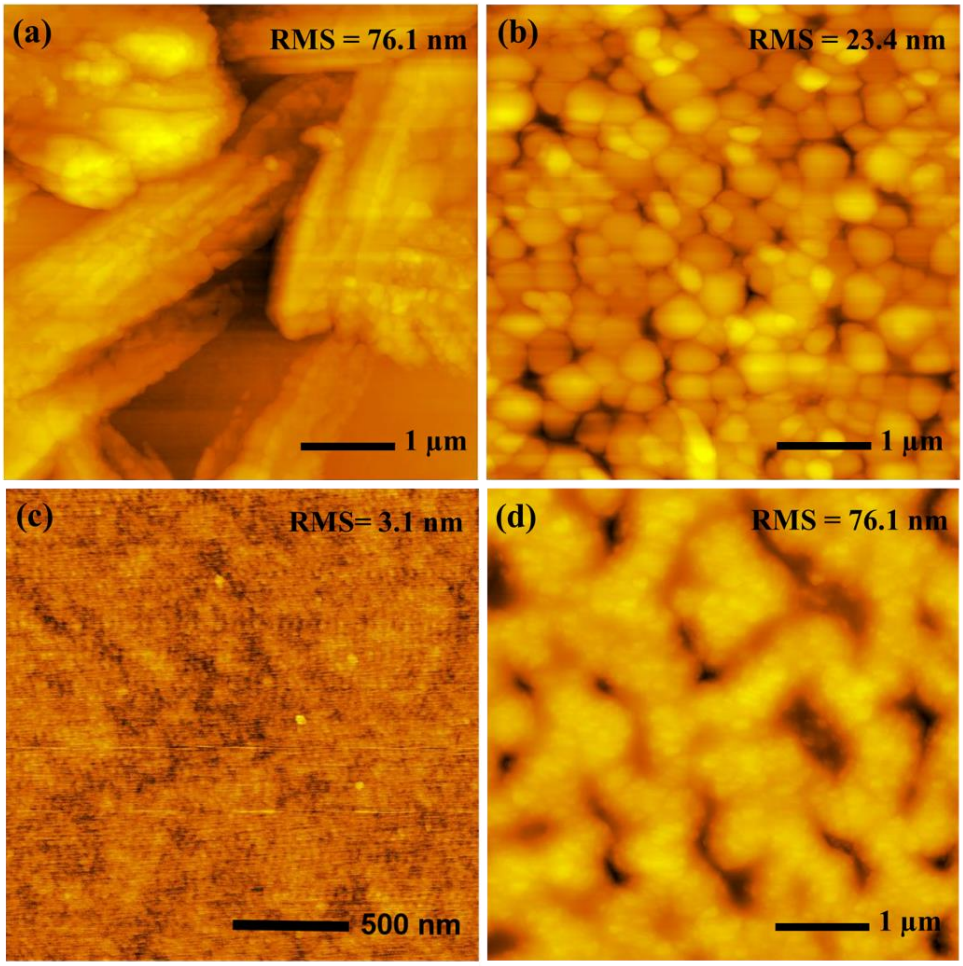

Figure 2.3. AFM images of $MAPbI_3$ films prepared by spin coating (a) without and (b) with the addition of IL to control morphology; (c) air-stable uniform compact TiO_x film prepared by CBD; (d) $MAPbI_3$ small clusters prepared at RT.

The EDX-analysis of $MAPbI_3$ films showed mostly similar in both cases (with/without IL) the ratio Pb to I is around 21/64 in good agreement with a PbI_3 stoichiometry.

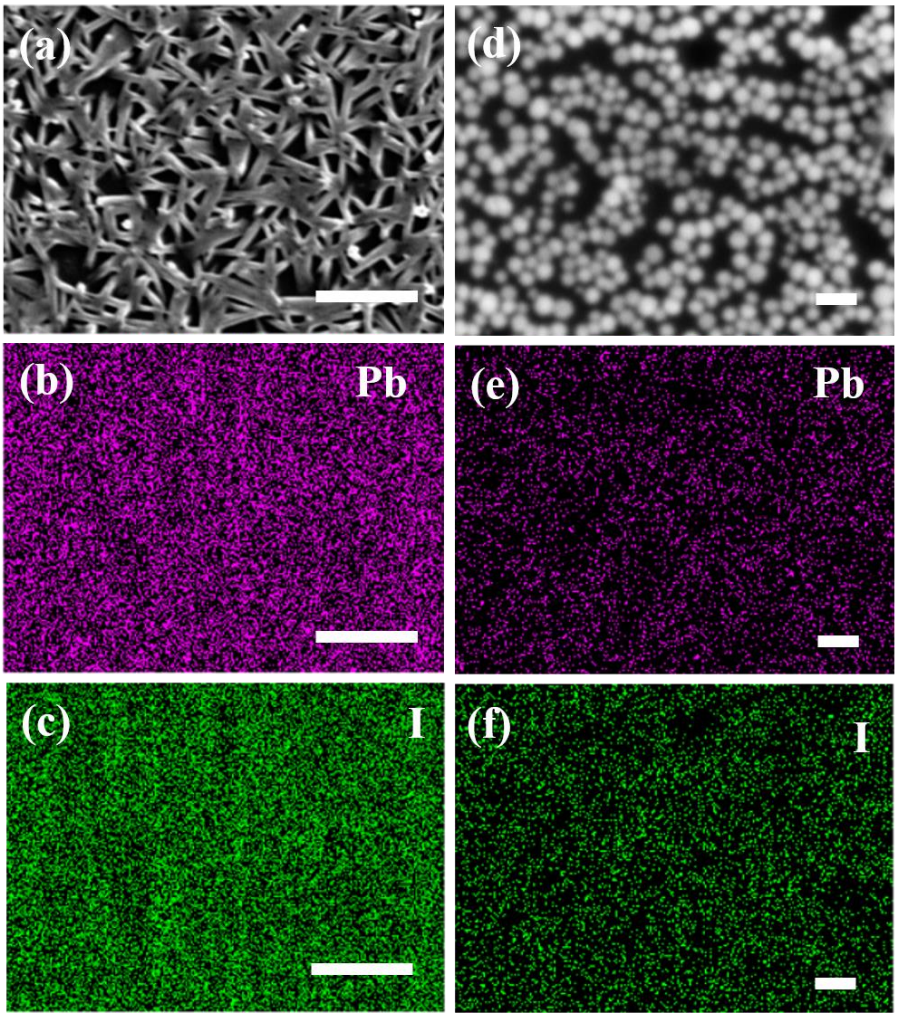

Figure 2.4. (a) The dark field images of $MAPbI_3$ film formed without IL and EDX mapping of (b) lead and (c) iodine (10 µm scale bar for all); (d) the dark field images of $MAPbI_3$ film formed with IL and EDX maps of (e) lead and (f) iodine (2.5 µm scale bar for all).

The XRD patterns of the perovskite films formed with and without IL, recorded at 100 °C, are shown in Fig. 2.5. It has been reported that the complete formation of perovskite film with full surface coverage is achieved at 100 °C [66] and, hence, selected for subsequent experiments. At temperatures lower than 100 °C, the NP films remained aggregated and were not uniformly distributed. Moreover, if the temperature is ≥ 120 °C,

the decomposition of $MAPbI_3$ is initiated and induces poor film coverage.[67] The diffraction peaks of the perovskite films prepared at 100 °C were observed at 2θ = 14.01°, 28.40°, 31.91°, and 40.74° for films both with and without IL, and are assigned to the (110), (220), (310) and (224) crystal planes, respectively. These peak positions are consistent with an orthorhombic crystalline structure in both films.[59, 68] It should be noted that there was no PbI_2 peak at 12.65° in either of the XRD patterns, which indicates the complete consumption of PbI_2. The mean crystallite sizes for the perovskite crystals formed with and without IL were 35.8 and 37.5 nm, respectively, estimated from the full width at half-maximum of the (110) peak using the Scherrer formula. (See Appendix II, Table A2.1). These results indicate that the crystallinity is almost similar, even after the addition of IL.

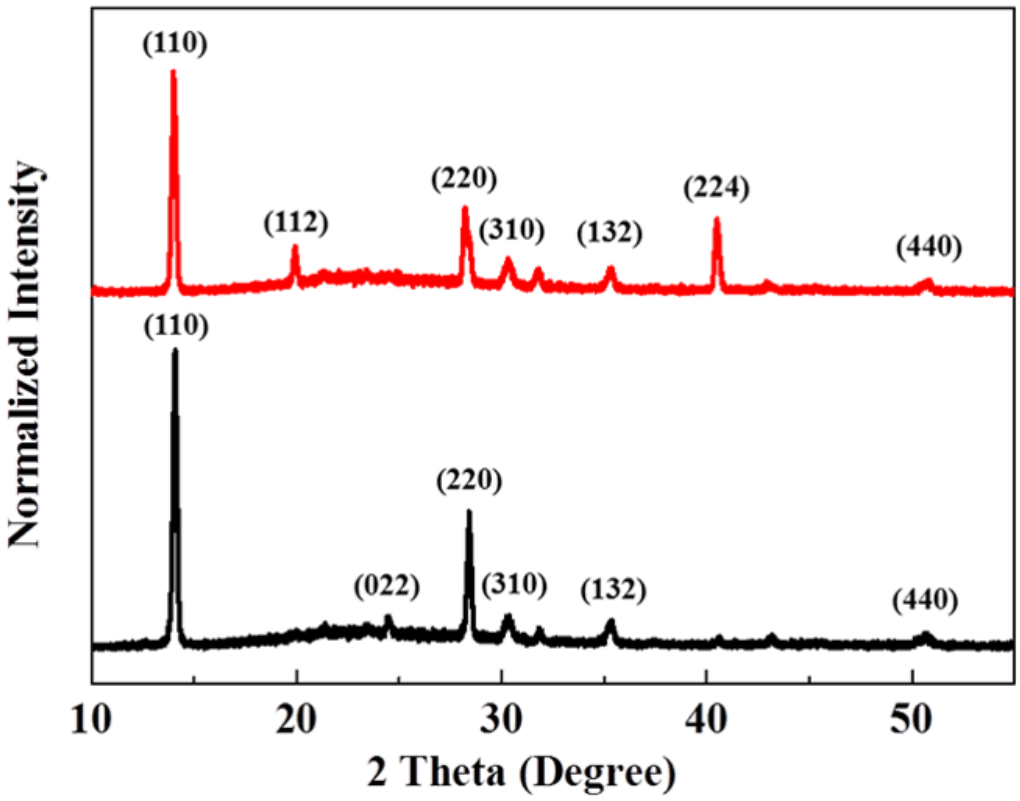

Figure 2.5. The XRD patterns of $MAPbI_3$ films formed with (red color) and without IL (black color).

The UV-Vis spectra of $MAPbI_3$ films, with and without IL, on glass/ITO/TiO_x substrates are shown in Fig. 2.6. The maximum absorption spectrum for DMF is observed at around 263 nm (not shown in Figure), while it is at around 340 nm for only IL. The strong absorption peaks as observed at around 493 and 396 nm in the system with IL correspond to the imidazolium cation and NPs, respectively.[69] The observation of UV-Vis study is further verified using the SEM technique. The film produced without IL absorbed more strongly at > 500 nm than that formed with IL, which can be attributed to the formation of pin holes and incomplete coverage of the $MAPbI_3$ film. In contrast, the film produced with IL showed a curve at < 500 nm, which indicated higher optical

density than that of the film formed without IL. The inset of Fig. 2.6 shows photographs of patterned glass/ITO/TiO_x substrates with $MAPbI_3$ films formed with and without IL. The thin film of $MAPbI_3$ NPs produced with IL was red-brown in color, flat in shape, and the surface coverage was uniform and free of pin-holes. Conversely, the $MAPbI_3$ nanocrystals formed without IL had a non-uniform surface, were scattered, and the film color was shiny gray.

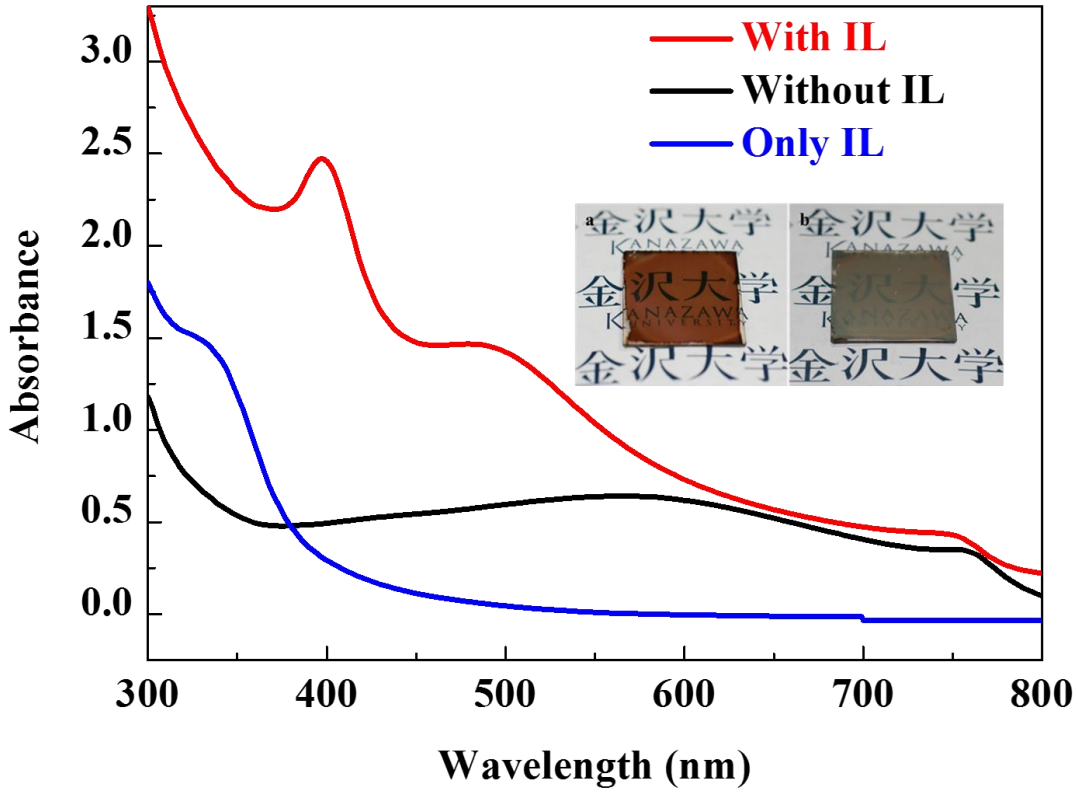

Figure 2.6. The UV-Vis spectra of only IL and $MAPbI_3$ films prepared with and without IL. Inset photographs show $MAPbI_3$ films prepared with (left) and without (right) IL.

2.3.2 Existence of IL within the NP film confirmed by FTIR-analysis

The existence of the IL additive within the $MAPbI_3$ films was confirmed from the FTIR spectra (Fig. 2.7). The FTIR reveals that the IL molecules are adsorbed on the surface of the $MAPbI_3$ NPs as indicated by the absorption bands in the region of 2,650 to 3,000 cm^{-1}, which are assigned to C–H stretching of the imidazolium ring. The observation was similar to a pervious report by Ayi *et al* [69], which confirms that the molecules of IL are absorbed on the surface of the particles thus provides protection during the formation of nanostructured particles. The bands at 3,200–3,300 cm^{-1} along with the bands between 1,500 and 1,700 cm^{-1} can be attributed to N-H stretching and bending vibrational bands.

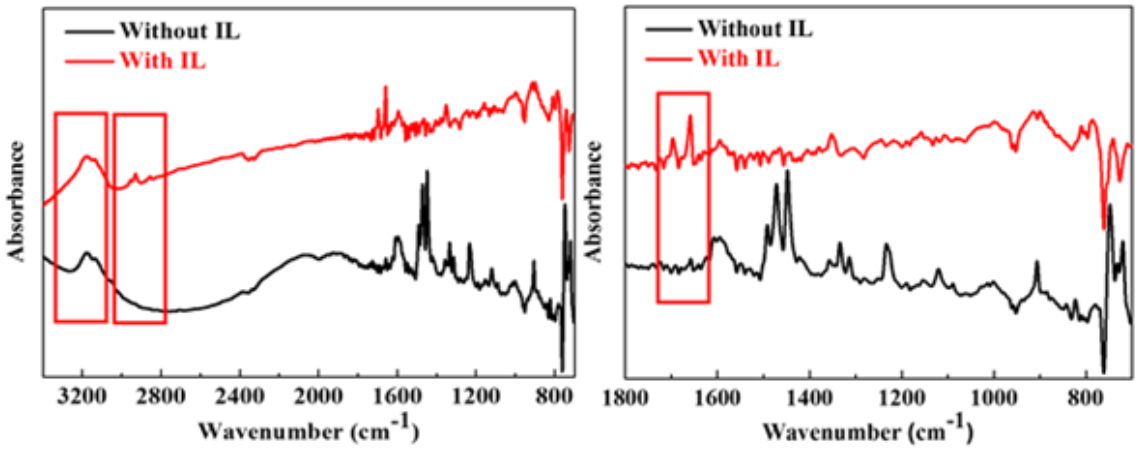

Figure 2.7. The FTIR spectra of $MAPbI_3$ films with and without IL.

The N-H bending vibration reveals that IL molecules intercalated into $MAPbI_3$ NPs films. The findings of both the C-H and N-H deformation modes in the $MAPbI_3$ NPs film assure the successful inclusion of IL.

2.3.3 Formation mechanism of $MAPbI_3$ films and photovoltaic properties

The $MAPbI_3$ nanocrystals formed without IL were ribbon like because of their rapid formation during spin coating caused by the fast evaporation of DMF. Such conditions promoted fast nucleation; therefore, the produced film remained incomplete and non-homogeneous. Jeon *et al*.[70] reported a similar occurrence with $MAPbI_3$ NC formation. The formation mechanism for the $MAPbI_3$ NPs is illustrated in Fig. 2.8. The $MAPbI_3$/DMF/IL solution was spun cast under the optimized conditions. During the spin-coating process, small clusters were formed, followed by homogeneous nucleation to generate NPs. These steps are consistent with the AFM analysis of the deposited film (Fig. 2.3d). Because of intercalation, the IL remained in the film, while the residual fraction of DMF evaporated. Small clusters were bonded to the nucleation sites, which then grew to form uniform spherical $MAPbI_3$ NP films. The $MAPbI_3$ NPs were forced to align perpendicular to the c-axis because of the high boiling point and extremely low vapor pressure of the IL. The surface energy of the prismatic plane was higher than that of the basal plane. In the presence of IL, whenever a crystal grew, it tried to minimize the overall surface energy, which promoted crystal growth in the *c*-axis direction.

Figures 2.9a present the schematic device structure of $MAPbI_3$ solar cells. The current density versus voltage (*J*-*V*) characteristics of $MAPbI_3$ films with/without IL measured at AM 1.5G illumination is shown in Fig. 2.9b. The device without IL showed a short-circuit current density J_{sc} of 11.90 mA/cm^2, V_{oc} = 0.92 V, FF = 0.49, and PCE = 5.10 %. On the contrary, the device with IL

displayed J_{sc} = 4.84 mA/cm^2, V_{oc} = 0.78 V, FF = 0.64, and PCE = 2.44 %. The PCE was lower than the reference material (without IL) presumably due to the presence of IL in the films.

The preliminary results are promising as it is the first report on the fabrication of solar cells based on $MAPbI_3$ NPs. We also expect that the results will open a pathway towards a better understanding for the fabrication, modification and enhancement of the performance of solar cells with $MAPbI_3$ NPs.

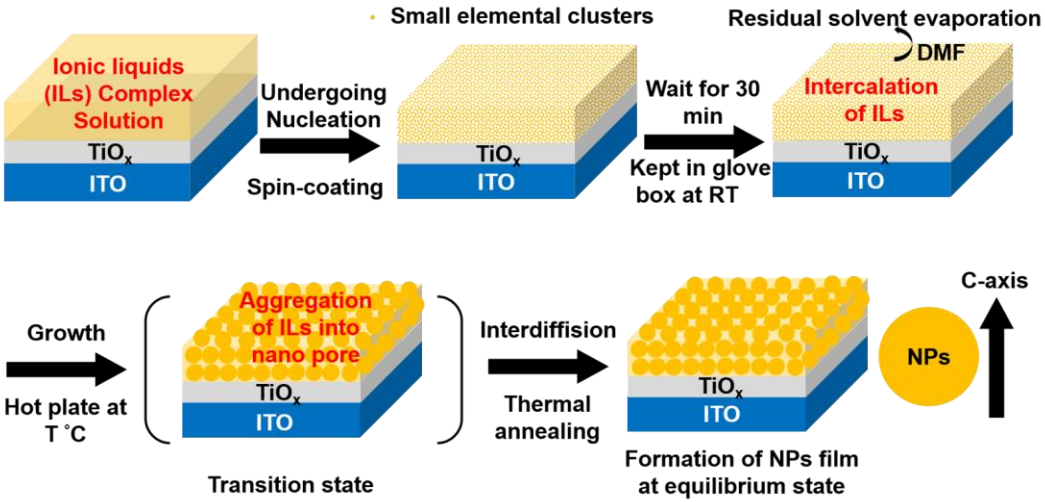

Figure 2.8. Schematic of the formation mechanism of $MAPbI_3$ NPs.

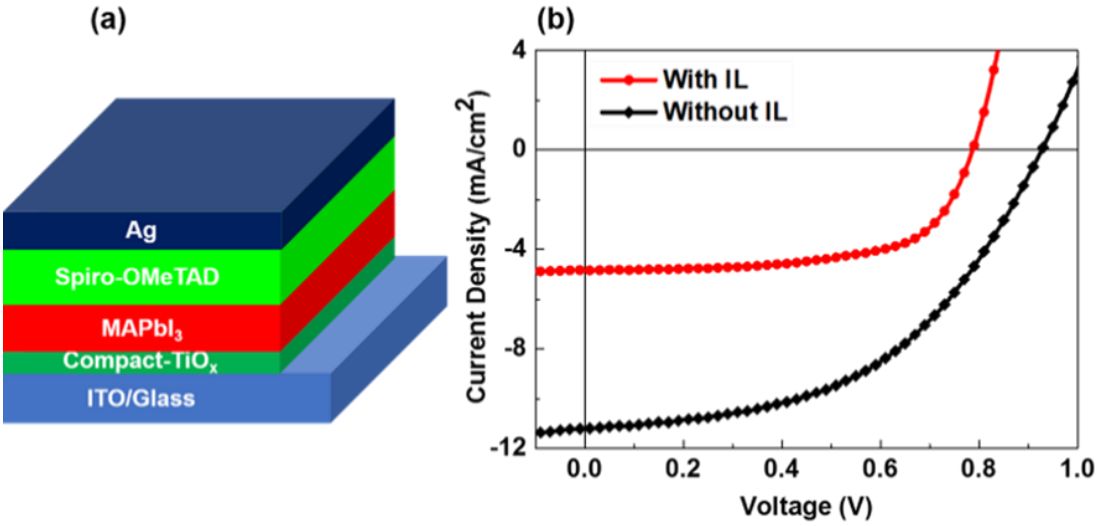

Figure 2.9. (a) Device structure of solar cells based on $MAPbI_3$; (b) The *J-V* characteristics obtained for the solar cells based on $MAPbI_3$ with and without IL.

2.3.4 A non-destructive solvent-assisted washing procedure for preparing $CH_3NH_3PbI_3$ NP films.

In the present case, we assume a hindering effect followed by impact on charge dissociation, transport, and/or recombination on the device performances due to the residual IL content remained on the $MAPbI_3$ NP films. Therefore, we have assumed that a non-destructive solvent-assisted washing procedure is required to be included to remove the IL from $MAPbI_3$ NP film, which is shown schematically in Fig. 2.10. The idea was inspired from the observation for small molecule-$MAPbI_3$ medium by Chen *et al*.[71] It is also reported that the adverse effect of small molecules trapped inside the perovskite sensitizer causing charge recombination can be minimized after solvent washing.[72] We hope that we will be able to ensure the complete removal of IL-contents from the $MAPbI_3$ NP film after

establishing an optimized condition using a suitable solvent, and the efficiency of the resulting solar cell will be improved.

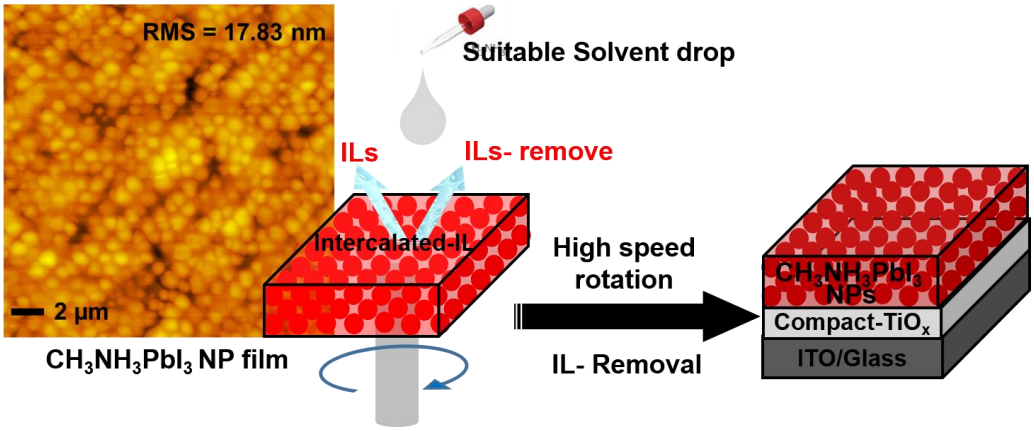

Figure 2.10. Schematic illustration of solvent additive procedure for preparing $MAPbI_3$ NP film.

2.4 Conclusions

We fabricated spherical NPs of $MAPbI_3$ using a simple spin-coating method by incorporating a small amount (1 wt %) of an IL in the spin-coating solution. The $MAPbI_3$ NP thin films were uniform and free of pin holes, and the excellent morphology was due to the addition of IL. The light-absorption property has also been improved. The photovoltaic properties of perovskite solar cells have been studied, and the preliminary performance data indicate that the $MAPbI_3$ NPs could be used to design unique solar cells.

<This page is intentionally left blank to indicate the chapter break>

Chapter Three: Shape-controlled $CH_3NH_3PbI_3$ nanoparticles for planar heterojunction perovskite solar cells

The following chapter describes the use of ionic liquid as additive for shape-controlled $CH_3NH_3PbI_3$ nanoparticles employing a simple spin-coating technique for planar heterojunction perovskite solar cells.[48]

3.1 Introduction

Hybrid organometal halide perovskites like methylammonium lead iodide ($CH_3NH_3PbI_3$) are attracting considerable attention as energy-efficient light-absorbing materials for photovoltaic applications because of their solution processability, tunable bandgaps, strong absorption coefficients and cost effectiveness.[6] Perovskites have shown potential applications in multiple fields, such as, photocatalysis,[32] ferroelectric,[30, 31] superconductor,[27] sensors[28] and thermoelectrics.[35] Semiconductor nanocrystalline pigments are attractive light harvesters due to their sub-wavelength features that enabled quantum size effects, leading to very low reflection and increased photon absorption to provide higher cell efficiency without the need for additional antireflection coatings. Besides, the large surface areas of nanotextured materials allow efficient energy conversion and charge–carrier recombination.[36] Complex shaped perovskite NPs, hereafter refers to NPs, can be of one-dimensional (nanowires, nanotubes, and nanorods),

two-dimensional (nanodiscs, nanoplatelets, nanosheets, etc.), or other complex shaped nanostructures including rod-sheet heterogeneous NPs, etc. Up to the present time, there have been many reports on quantum wells,[38, 39], wires [40], and dots [41] synthesized as organometal halide perovskites. The chemical synthesis approaches to prepare NPs exhibit great potential in manipulating the individual particle characteristics including size, shape, and structure or surface properties. Several chemical synthesis methods have been developed to formulate complex-shaped metal perovskite NPs. The hydrothermal/ solvothermal method,[50, 58, 73] and the wet chemical synthesis[45] method are frequently used. However, the researchers are interested to develop thin-film perovskite materials through simple, cost-effective and precise techniques rather than chemical synthesis. The interest is due to the increasing environmental benefits as achieved from the use of room temperature ionic liquids (RTILs). The RTILs are 'green' liquids with high fluidity, low melting temperature, high boiling point, low toxicity, non-flammability, high ionic conductivity, excellent electrochemical and thermal stability, ability to dissolve a variety of materials, and low vapor pressure.[73]

Thin film organic and inorganic hybrid halide perovskites, turned out to be promising components of next generation solar cells, which has been used as a light-absorber material with 3.8% conversion efficiency, was first reported by Kojima *et al.*[11] The encouraging discovery continued further, incorporating hybrid halide perovskites as light harvesters in solar cells, which increases in the conversion efficiencies up to 20.1%.[74] The planar heterojunction perovskite solar cells attracted more interest than mesostructured perovskite solar cells for photovoltaic applications. Because preparation

of high-quality mesostructed film and compact-TiO_2 layers needs high-temperature processes, which limits their application in simpler architectures[15, 75] The limitation has been circumvented by developing planar heterojunction perovskite solar cells by several groups[68, 76] without a mesoporous TiO_2 layer. Kuwabara *et al.*[61, 62] deposited a uniform, compact and air stable amorphous TiO_x film as an electron collection layer via chemical bath deposition (CBD) at low temperature, which offered a low cost, easy and scalable technique. In this assembly, the amorphous TiO_x layer formed good physical and electronic contacts with the perovskite layer. Low temperature compact-TiO_x layer showed less conformity, which generated direct contact between perovskite layers and the indium tin oxide (ITO) cathode. Schmidt *et al.*[50] reported the synthesis of methylammonium-lead-bromide NPs by a simple spin-coating method on a quartz substrate for use in the solar cells. Moreover, the preparation of methylammonium lead iodide shaped nanowires by a low temperature solution process using a simple slip-coating method [53] have been reported for the fabrication of nanostructured organic lead halide perovskites with the objective of solar cell manufacturing. The control of morphology and crystallization have been the main challenges encountered during nanostructured the perovskite thin film fabrication. Since poor morphology may limit the performance of resulting devices owing to electrical shorting or due to the effects on charge dissociation, transport, and/or recombination[58-60]- an efficient approach to fabricate perovskite films with uniform morphology is required to be developed to design energy-efficient solar cell.

In this work, we used a simple spin coating method to prepare size and shape controlled spherical $CH_3NH_3PbI_3$ NPs by using a 1-hexyl-3-methylimidazolium chloride (HMImCl) ionic liquid (IL) additive as a morphology controller. $CH_3NH_3PbI_3$ precursor in DMF solution, containing IL, produces homogeneous nucleation sites and allows slow crystallization of $CH_3NH_3PbI_3$ formation due to the high boiling point and extremely low vapor pressure of IL, respectively, hence finally producing $CH_3NH_3PbI_3$ NPs with controllable size and shape. The effect of varying percentages (wt %) of IL have also been investigated. In addition, photovoltaic properties have been measured to calculate the power conversion efficiency (PCE) of the NPs in relation to increasing IL contents. It has been observed that the PCE has changed with varying $CH_3NH_3PbI_3$ NPs sizes, shapes and morphology.

3.2 Experimental

3.2.1 Preparation of compact-TiO_x films by CBD

Organic photovoltaic devices were fabricated on commercial ITO patterned glass substrates, which was pre-treated by oxygen plasma treatment for 20 minutes. TiOx film was prepared by CBD according to the procedure described by Kuwabara *et al*.[61] In brief, $TiOSO_4$ (1.6 g) solution was added to diluted H_2O_2 (0.170 g) aqueous solution, and then the mixed solution was diluted just to 50 ml with ultrapure water. This solution was transferred to a screw vial to use as the reaction bath for film deposition. The glass side of the ITO substrate was covered with an imide tape to prevent extra deposition of TiO_x, and then the ITO substrate was immersed into the bath at 80 °C. The solution became cloudy as we applied heat and after appropriate dipping time (6 minutes), starting from this

cloudy point, the immersed ITO substrate was pulled out from the bath. The as-deposited TiO_x film on the ITO was ultrasonicated for 5 minutes in water and heated on a hot plate at 150 °C for 1 hour in air. A 30 nm thin amorphous TiO_x layer was obtained by using one time operation.

3.2.2 Solar cells device fabrication

The PbI_2 (Tokyo Chemical Industry, Tokyo, Japan) (0.144 g) and methylammonium iodide (0.05 g) were mixed in anhydrous DMF (615 µL) (Kanto Chemical, Tokyo, Japan) at 2.89:1 molar ratio followed by shaking at room temperature (RT) for 30 min to prepare the $CH_3NH_3PbI_3$ solution (25 wt %). The 1-hexyl-3-methylimidazolium chloride (HMImCl; Sigma Aldrich, St. Louis, MO) IL was used as the additive at varying concentration in the 25 wt % $CH_3NH_3PbI_3$ solution in DMF. The PbI_2 was dehydrated in vacuum at 450 °C for 3h. A homogeneous layer of amorphous compact-TiOx film was deposited on the ITO-coated glass substrate. The $CH_3NH_3PbI_3$ (25 wt %) was then spun-cast on the TiOx layer at 3000 rpm. A change in the film color, from transparent to brown, was observed during the spin-coating process. The resultant film was left for 30 min in a glove-box at RT to allow slow solvent evaporation, followed by annealing on a hot plate at 100 °C for 10 min to obtain a $CH_3NH_3PbI_3$ NPs of 200 nm thickness. The hole-transporting layer (HTM) was deposited by spin-coating at 4000 rpm using 2,2′,7,7′-tetrakis (N,N-di-p-methoxyphenylamine)-9,9′-spirobifluorene (spiro-OMeTAD) in chlorobenzene (0.058 M) containing 4-tert-butylpridine (0.19 M) and lithium bis (trifuluoromethylsulfonyl) imide (0.031M), tris [2-(1H-pyrazol-1-y1)-4-tert-butylpyridine] cobalt (III) tris [bis(trifluoromethysulfonyl) imide] (5.6 × 10-3 M) as

dopants.[63, 64] After that the films were left on hot plate in the glove box for annealing at 70 °C for 20 min. Finally, the films were placed in a vacuum chamber and 100 nm thick silver electrodes were deposited on the spiro-OMeTAD layer at around 2.83×10^{-4} pa. The active device area showed 4 mm^2. The current densities versus voltage (*J-V*) of the cells have been analyzed under simulated AM 1.5G solar illumination with Keithley 2401 Digital Source Meter. The Scanning Electron Microscope (SEM) and Energy-dispersive X-ray spectroscopy (EDX) (SU1510, Hitachi High-Tech, Tokyo, Japan) were used to analyze the surface morphology and elemental mapping. The Atomic Force Microscopy (AFM) measurement (SII SPI3800N, Seiko, Tokyo, Japan) was used to re-analyze the surface morphology. The UV-Vis absorption spectra of perovskite films were measured using an absorption spectrophotometer (U-3310, Hitachi, Tokyo, Japan). The XRD spectra of the prepared films were measured by using an X-ray Diffractometer (SmartLab, Rigaku, Japan) having an X-ray tube (Cu Kα, λ = 1.5406 Å). Fourier Transform Infrared Spectroscopy (FT/IR-6300, Jasco, Tokyo, Japan) with Infrared Reflection Absorption Spectroscopy (IRRAS) were performed for further analysis of the resulting films.

3.3 Results and discussion

3.3.1 Chemical structure of IL and mixture solution of $CH_3NH_3PbI_3$ and IL

We introduced varying wt % of IL (chemical structure: Fig. 3.1a) as a morphology controlling additive with $CH_3NH_3PbI_3$ in the DMF solution. We obtained a clear yellow-orange colored homogeneous solution having no aggregate or NPs (Fig. 3.1b).

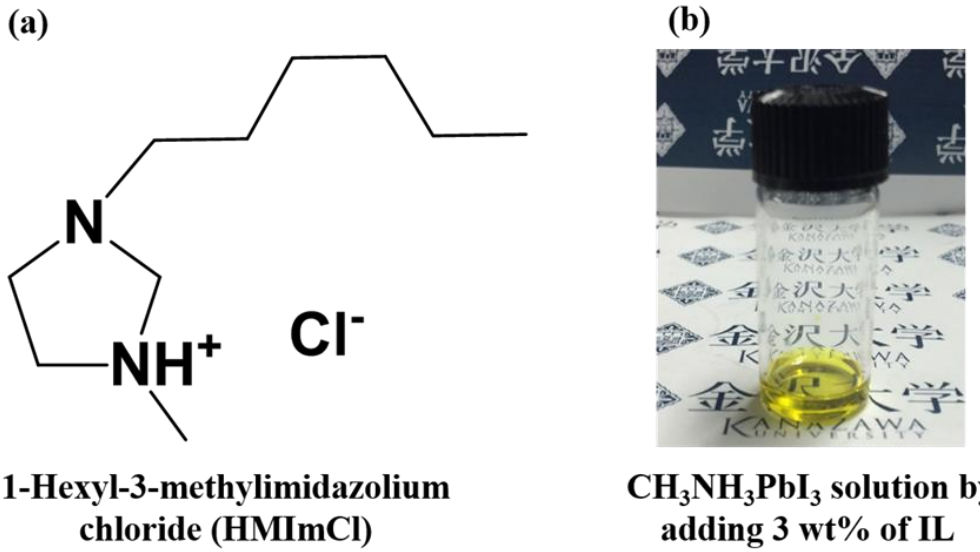

Figure 3.1. (a) Chemical structure of 1-hexyl-3-methylimidazolium chloride (HMImCl), (b) Homogeneous mixture solution of $CH_3NH_3PbI_3$ and IL.

3.3.2 The general concept of IL used as a morphology controller

The concept of IL used as a morphology controlling additive to the solution of $CH_3NH_3PbI_3$ in DMF is simple; however, we hypothesized that the additive essentially important to have an extremely low vapor pressure and high boiling point than DMF (2.9 mm/Hg at room temperature) to minimize the rapid crystallization, as well as it should be adequately miscible with DMF. Hence, the IL have been chosen as a morphology controller due to high boiling point (higher than 300 °C), extremely low vapor pressure of 0.1 mm/Hg at room temperature and have high miscibility with DMF. Therefore, IL could be utilized as an efficient morphology controller.

3.3.3 Size and shape control of perovskite NPs films

$CH_3NH_3PbI_3$ NPs having spherical morphology, was formed as shown in Fig. 3.2 (a, b and c), in the presence of 1, 3 and 7 wt % IL with respective diameters of 540, 350

and 600 nm. In contrary, the addition of high concentration of 10 wt % IL has resulted in irregular aggregation of $CH_3NH_3PbI_3$ blocks as shown in Fig. 3.2d. We observed unchanged shapes but changed morphology of NPs with varying wt % of IL to the solution. The observation was similar to a previous report by Duan *et al*.[77] which confirms that the sizes and morphologies of the crystals depended on the concentration of the ionic liquid.

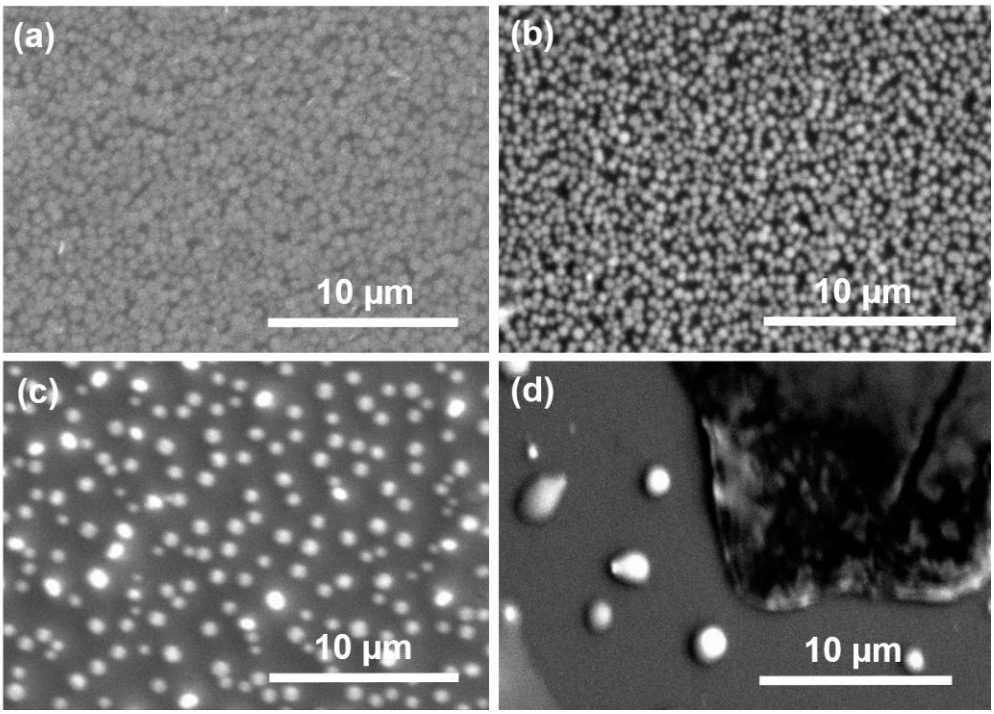

Figure 3.2. The SEM images of the $CH_3NH_3PbI_3$ NPs prepared in the presence of varying concentration of IL: (a) 1 wt %, (b) 3 wt %, (c) 7 wt %, and (d) 10 wt %.

The observation was further confirmed by the AFM analysis. The AFM image (Fig. 3.3e-f), showed the aggregated morphology of NPs with non-uniform distribution for 7 and 10 wt % IL in solution, while the morphology was well developed for 1 and 3 wt % IL in solution as shown in Fig. 3.3c-d, respectively. The root-mean-square (RMS)

roughness of the $CH_3NH_3PbI_3$ films were respectively 21.19, 17.83, 71.25 and 121.29 nm at 1, 3, 7 and 10 wt % of IL. The RMS roughness was smoother with 3 wt % IL in solution as compared to the other compositions. Air stable amorphous compact-TiO_x layer having smooth morphology of 30 nm thickness was achieved in one-time operation as shown in the AFM analysis (Fig. 3.3a). The RMS roughness value of the resulting film was 4.13 nm.

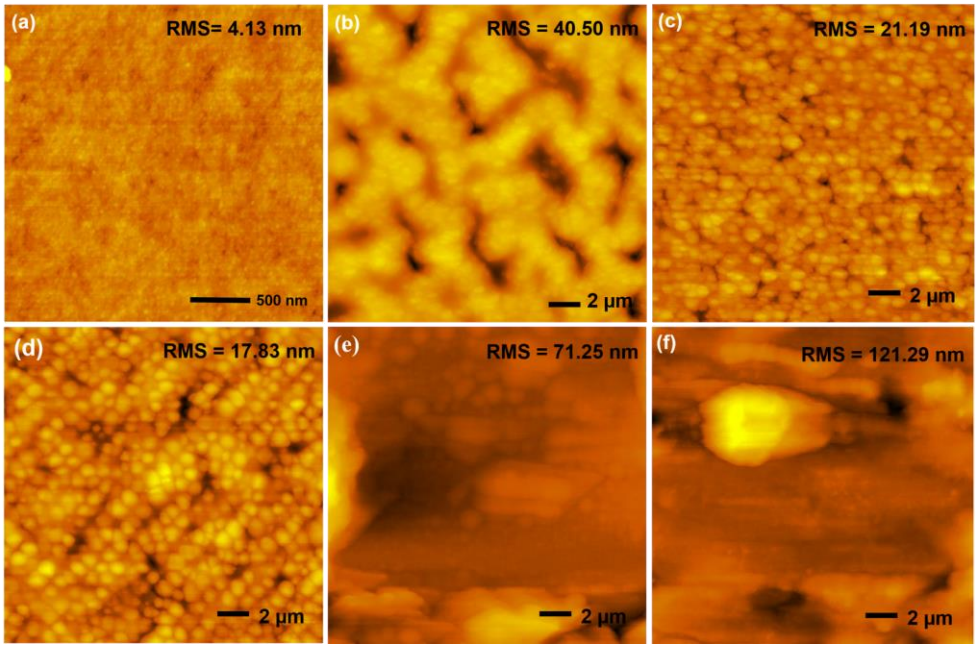

Figure 3.3. The AFM images of (a) TiO_x film; (b) As-deposited $CH_3NH_3PbI_3$ small clusters prepared at RT and $CH_3NH_3PbI_3$ NPs with varying concentration of IL: (c) 1 wt %, (d) 3 wt %, (e) 7 wt %, and (f) 10 wt %.

3.3.4 Effect of annealing temperature on the NPs properties

The effect of annealing temperature on the nanoparticles properties was clarified by including varying temperatures of 3 wt % IL condition. The morphologies of the films

produced at room temperature (RT), 70, and 130 °C were different from that obtained at 100 °C, as determined by AFM (Fig. 3.4). It is found that the annealing temperatures

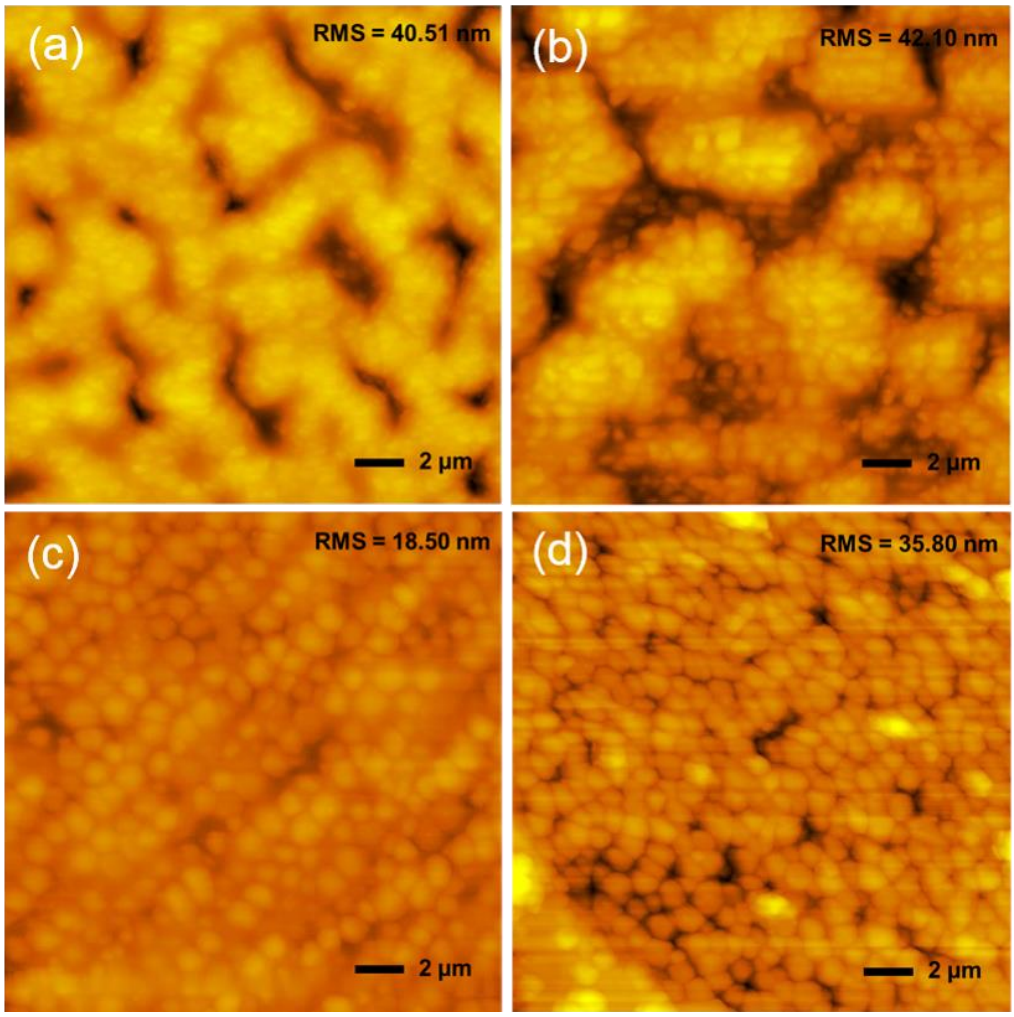

Figure 3.4. AFM images of $CH_3NH_3PbI_3$ NP films prepared by annealing at (a) RT, (b) 70, (c) 100, and (d) 130 °C for 10 min.

play an important role in the formation of resulting NPs. Figure 3.4 reveals that the NPs formed at RT and 70 °C remained aggregated and were not uniformly distributed. However, individual $CH_3NH_3PbI_3$ NPs were fabricated at 100 and 130 °C. The RMS roughness of the films were 40.51, 42.10, 18.50, and 35.80 nm at annealing temperatures

of RT, 70, 100, and 130 °C, respectively. The RMS roughness of the film annealed at 100 °C was lower than that of the films annealed at RT, 70, and 130 °C. Increasing the annealing temperature to 130 °C, the resulting $CH_3NH_3PbI_3$ NPs adopts a large size, inhomogeneous and leaky film. Hence, it can be clearly indicated that the morphology and size of the resulting film formed is significantly influenced by the annealing temperatures. However, when the annealing temperature was below the 80 °C, we obtained aggregated and non-uniform film. We attributed it to the slow transformation rates. In the practical case, if the annealing temperature is set greater than 120 °C, it would accelerate the decomposition of $CH_3NH_3PbI_3$ and induce poor film coverage.[67] Therefore, the perovskite films are mostly prepared by thermal annealing at 100 °C, which is reported to promote full surface coverage film and can provide sufficient energy for perovskite phase formation.[66]

3.3.5 Composition of NPs

The NPs processed with varying wt % of IL may be composed of single or multiple phases. We performed the EDX-mapping (Fig. 3.5a-i) to visualize a two-dimensional map of the relative location of the different elements in the sample to determine the phases. The color intensity assisted to judge the relative amount of element distributed on the surface. The EDX-analysis of $CH_3NH_3PbI_3$ NP showed mostly single phase in all the cases (1, 3 and 7 wt % IL). The ratio Pb to I was around 20/61 which is in good agreement with a PbI_3 stoichiometry.

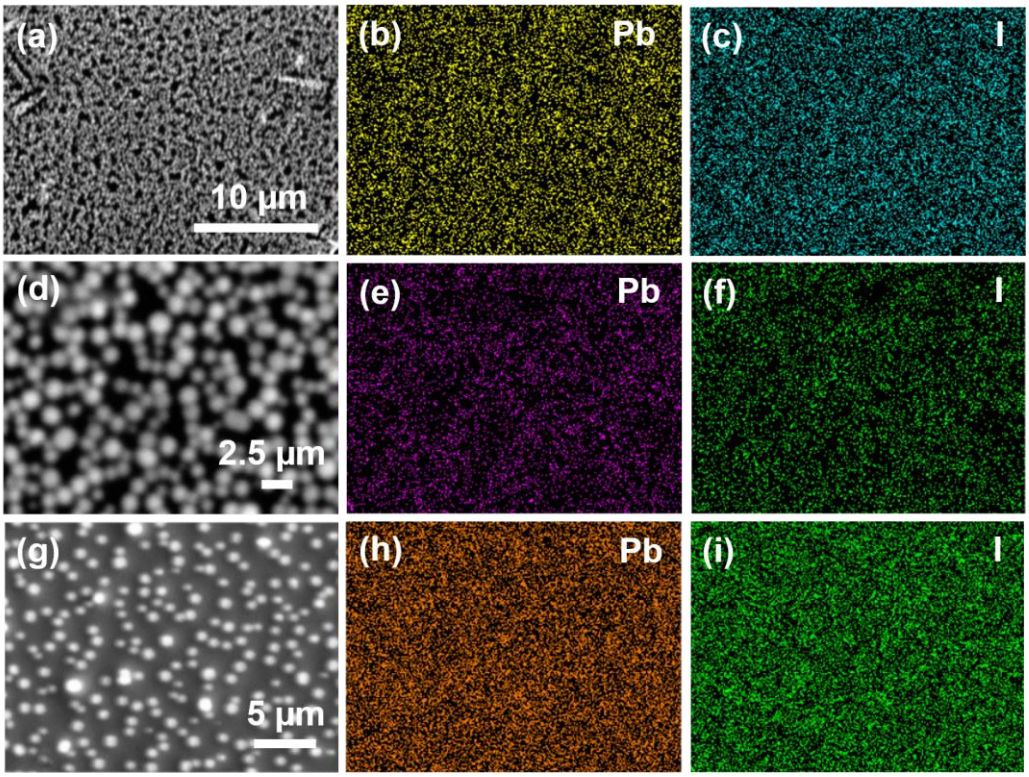

Figure 3.5. (a) The dark field images of $CH_3NH_3PbI_3$ NP formed with 1 wt % IL and EDX mapping of (b) lead and (c) iodine (10 µm scale bar for all); (d) the dark field images of $CH_3NH_3PbI_3$ NP formed with 3 wt % IL and $CH_3NH_3PbI_3$ EDX maps of (e) lead and (f) iodine (2.5 µm scale bar for all); (g) the dark field images of $CH_3NH_3PbI_3$ NP formed with 7 wt % IL and EDX maps of (h) lead and (i) iodine (5 µm scale bar for all).

3.3.6 Crystallinity, FTIR spectra, and absorption of Perovskite NPs

The XRD patterns (Fig. 3.6) of perovskite films for NPs as prepared by using varying wt % of ILs showed peaks mostly similar to that of $CH_3NH_3PbI_3$ bulk. The diffraction peaks with IL were obtained at 2θ = 14.01, 28.40 and 40.44°, which were assigned respectively to the (110), (220) and (224) crystal planes. The peak positions confirmed an orthorhombic crystalline structure.[68, 78] There was a tiny peak at 12.65°, corresponding to a low-level impurity of PbI_2 at 7 wt % IL. It should be noted that

aforementioned peak in the XRD patterns (with IL) indicated the complete consumption of PbI_2 within the process. The mean crystalline sizes for the $CH_3NH_3PbI_3$ NPs, with (1, 3 and 7 wt % IL) were 35.8, 38.0, and 44.0 nm, respectively as estimated by using the Scherer's formula from the full width at half-maximum of the (110) primary peak. The results indicated a similar crystallinity; nevertheless, the wt % of IL was varied. The film obtained with 10 wt % IL in solution showed the primary peak at 30.45°, which could be assigned to $CH_3NH_3PbI_3$ (310) crystal plane.

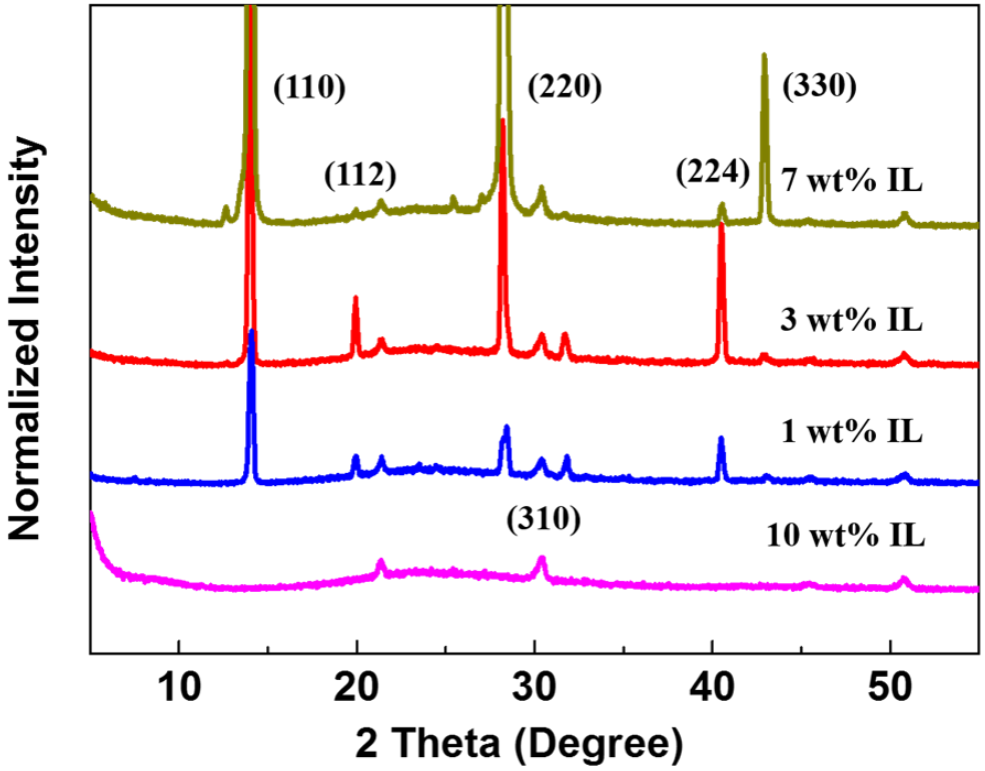

Figure 3.6. The XRD patterns of $CH_3NH_3PbI_3$ films processed with varying wt % of IL.

The existence of IL additive within the $CH_3NH_3PbI_3$ films was confirmed by the FTIR spectra (Fig. 3.7). The FTIR reveals that the IL molecules have been adsorbed on

the surface of the $CH_3NH_3PbI_3$ NPs. It was indicated by the absorption bands in the region of 2,650 to 3,000 cm^{-1}, which have been assigned to C–H stretching of the imidazolium ring. The observation was similar to a pervious report by Ayi *et al*. [69] which

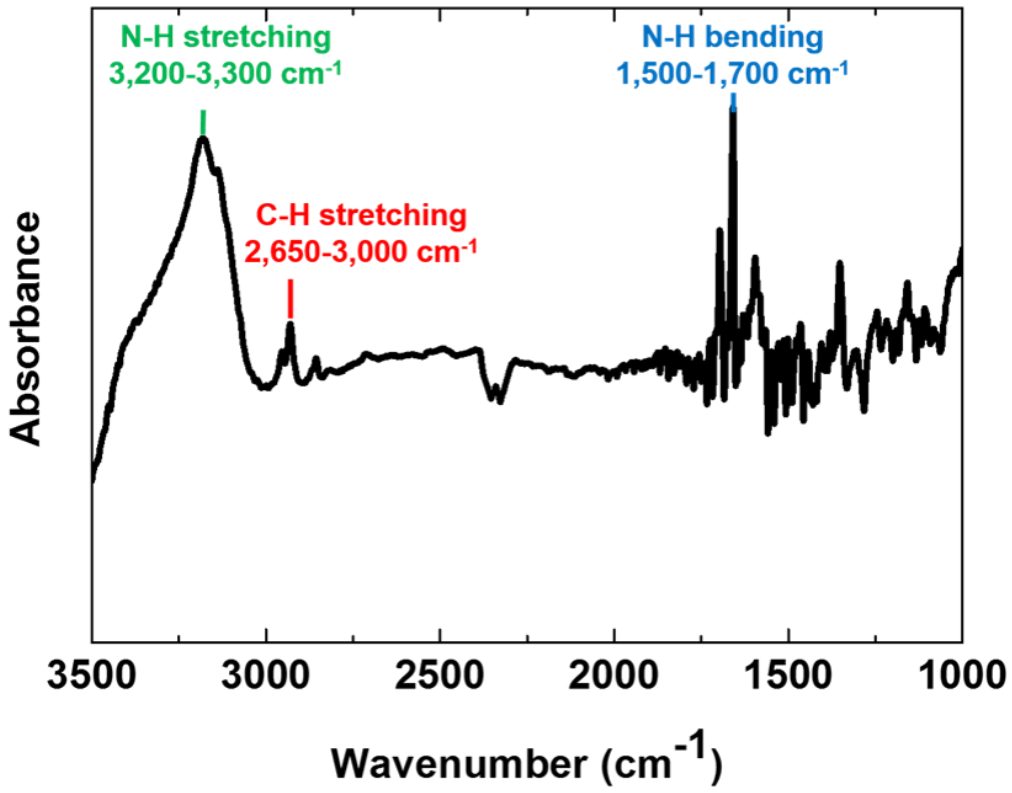

. **Figure 3.7.** The FTIR spectra of $CH_3NH_3PbI_3$ NPs film

confirmed that the molecules of IL were absorbed on the surface of the particles and provided protection during the formation of nanostructured particles. The bands at 3,200–3,300 cm^{-1} along with the bands between 1,500 and 1,700 cm^{-1} were attributed to N-H stretching and bending vibrational bands. The N-H bending vibration revealed that IL molecules intercalated with $CH_3NH_3PbI_3$ NPs films. The findings of both the C-H and

N-H deformation modes in the $CH_3NH_3PbI_3$ NPs film assured the retention of IL molecules.

The UV-Vis spectra of $CH_3NH_3PbI_3$ films with varying wt % of IL cast on glass/ITO/ compact-TiO_x substrates are shown in Fig. 3.8. The absorption spectrum of DMF was discovered at around 263 nm (not shown in Figure), while it was at 340 nm for only IL. The optical properties of $CH_3NH_3PbI_3$ NPs depend on the size and the shape of the particles. The absorption peaks were observed at around 493, 550, 520 and 525 nm in the system with 1, 3, 7 and 10 wt % IL, respectively, which corresponded to NPs, in accordance with the observation from Ayi, *et al.*[69] The sharp absorption peaks for the spherical NPs also indicated a fairly uniform shape and size of NPs.

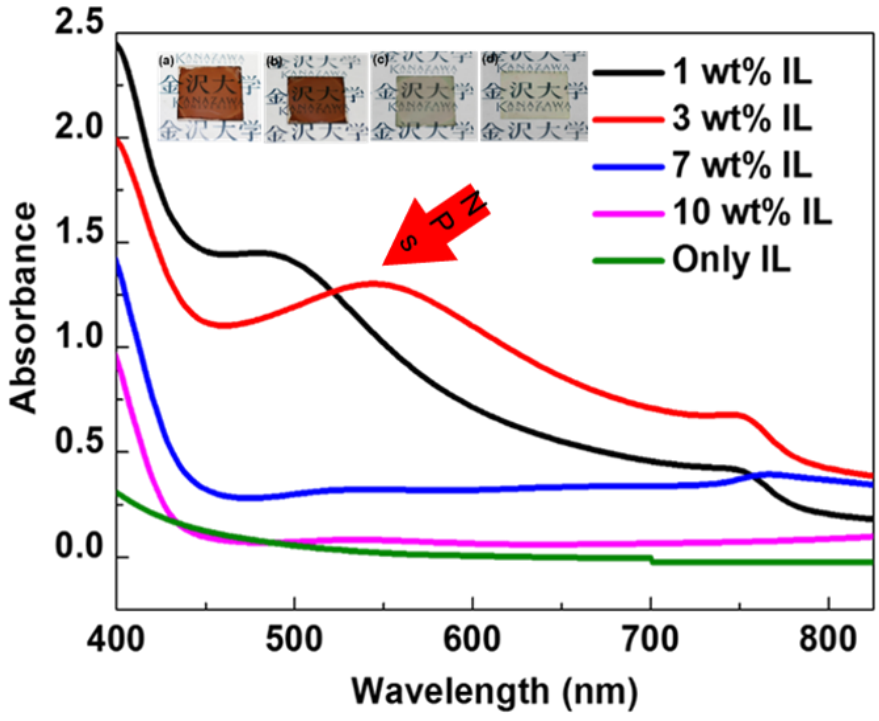

Figure 3.8. The UV-Vis spectra of the $CH_3NH_3PbI_3$ films processed with varying wt % of IL as well as only IL. Inset photographs show $CH_3NH_3PbI_3$ films prepared with varying concentration of IL: (a) 1 wt %, (b) 3 wt %, (c) 7 wt %, and (d) 10 wt %.

3.3.7 Calculation of viscosity of IL-DMF liquid solution

It was clear that the concentration of IL played a vital role on the sizes, shapes and morphologies of the $CH_3NH_3PbI_3$ NPs. A uniform $CH_3NH_3PbI_3$ NPs with well-defined morphologies have been obtained in the presence of a small amount of IL as additive (Figure 3.2a-d). When the amount of the IL increased to 7 wt %, we obtained spherical $CH_3NH_3PbI_3$ NPs (Fig. 3.2c) having approximately 600 nm diameter. In contrast, 3 wt % of IL was the optimum condition leading to the formation of uniform $CH_3NH_3PbI_3$ NPs with a well-controlled spherical NPs with approximate diameter of 350 nm (Fig. 3.2b). However, when the amount of IL was increased to 10 wt %, we obtained amorphous $CH_3NH_3PbI_3$ blocks formed by irregular aggregation of small particles (Fig. 3.2d). We attributed it to the viscosity of the IL-DMF medium. A similar observation for IL-water medium was reported by Wu *et al.*[79] and the exponential expression used to express such characteristics were modified to fit into our system:

$$\eta = \eta_{\mathrm{IL}} \cdot \exp\left[{}^{-x_c}/_{a}\right] \qquad (3.1)$$

In Eq (3.1), x_c is the mole fraction of DMF, a is a characteristic constant of the mixture, and η_{IL} is the viscosity of the pure IL. The empirical equation point out that the viscosity of IL-DMF mixtures is increased exponentially when the mole fraction of DMF (x_c) is decreased. When the amount of IL is increased, the viscosity of the system

increases and the diffusion of the resulting complexes hindered. The resulting uniform thin film with good morphology was due to the presence of the IL.

3.3.8 Proposed formation mechanism and photovoltaic properties of perovskite NPs

The mechanism of $CH_3NH_3PbI_3$ film formation is illustrated in Fig. 3.9a and b. Due to first evaporation of the DMF solvent during spin-coating process, the $CH_3NH_3PbI_3$ crystal forms too rapidly and difficulty of obtaining perovskite films with good coverage and controllable morphology. Such condition promoted first nucleation; thus, the produced film remained inhomogeneous and incomplete. Eperon *et al*.[67] reported a similar occurrence with the $CH_3NH_3PbI_3$ nanocrystals formation. On the other hand, for the films fabricated using the DMF-IL additive system, the $CH_3NH_3PbI_3$-DMF/IL mixture was homogenized, and the spin coating was applied at the optimized conditions. We have assumed that during spin coating process, the high boiling point and an extremely low vapor pressure of IL would prevent the rapid crystal formation of $CH_3NH_3PbI_3$ and produced homogenous nucleation via the remaining IL in the film. The steps have been confirmed from the AFM analysis of the deposited film (Fig. 3.3b). The IL remained in the resulting film due to the intercalation while the residual fraction of DMF evaporated. The small clusters were bonded to the nucleation sites, and then endure growth to the large particles with controllable size and shape. Thus, finally enabling the resulting spherical $CH_3NH_3PbI_3$ NPs with controllable size and shape. The growth

direction of $CH_3NH_3PbI_3$ NPs were forced along with the perpendicular to the crystalline c-axis.

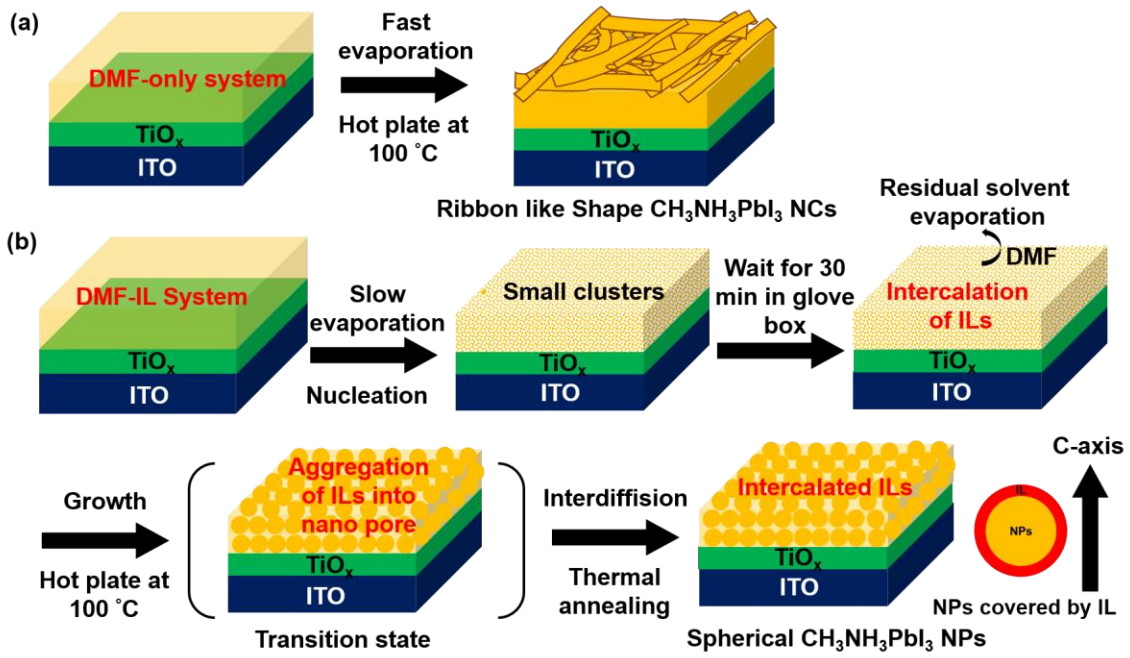

Figure 3.9. Schematic illustration of formation mechanism of $CH_3NH_3PbI_3$ film in (a and b) DMF-only and DMF-IL system.

Figure 3.10a showed the device configuration of solar cells based on $CH_3NH_3PbI_3$ NPs. The current density versus voltage (*J-V*) characteristics of $CH_3NH_3PbI_3$ NPs based solar cells as obtained by using the varying concentration of IL (1, 3 and 7 wt %) and were measured at AM 1.5G illuminations are shown in Figure 3.10b. The photovoltaic devices prepared with 1 wt % IL-doped $CH_3NH_3PbI_3$ NPs showed a short-circuit current density (J_{sc}) of 4.84 mA/cm^2. An increase in the J_{sc} value to 5.74 mA/cm^2 was observed for the photovoltaic device prepared using 3 wt % IL-doped $CH_3NH_3PbI_3$ NPs, while the J_{sc} value is decreased to 2.56 mA/cm^2 for 7 wt % doping of IL. The power conversion

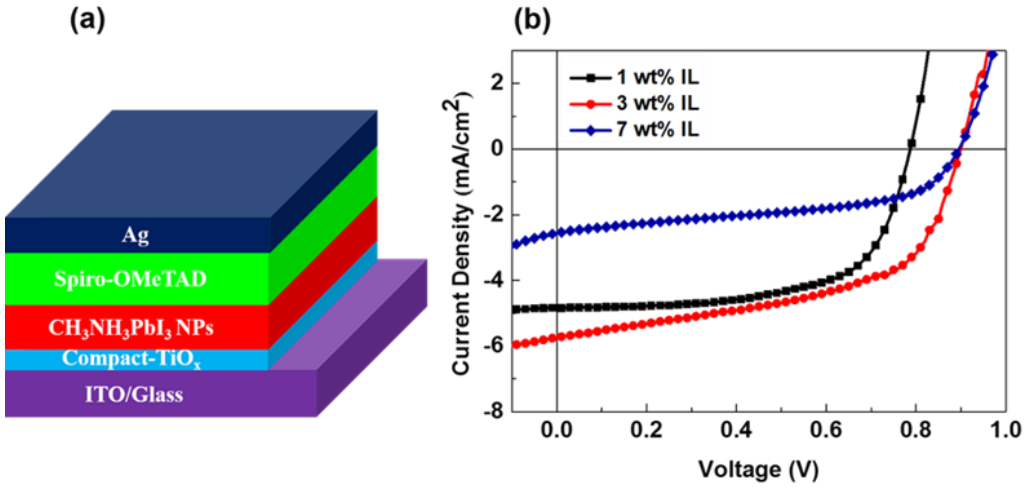

Figure 3.10. (a) Device configuration of solar cells based on $CH_3NH_3PbI_3$ NPs; (b) The *J-V* characteristics obtained for the solar cells based on $CH_3NH_3PbI_3$ NPs.

Table 3.1. Summary of cell performances of ITO/Compact-TiO_x/$CH_3NH_3PbI_3$ NPs/Spiro-OMeTAD/Ag.

Weight % of IL	J_{sc} (mA/cm^2)	V_{oc} (V)	FF (%)	PCE (%)
1	4.84	0.78	0.64	2.44
3	5.74	0.89	0.55	2.81
7	2.56	0.89	0.50	1.14

efficiency (PCE) is also followed the similar trend of the J_{sc} values, showing a higher PCE of 2.81% for the photovoltaic device of 3 wt % IL-doped $CH_3NH_3PbI_3$ NPs. All the parameters measured to study the performances of solar cells are summarized in Table 3.1. Optimization of the concentration with the 3 wt % of IL, we achieved $CH_3NH_3PbI_3$

NPs having more uniform shape, size, morphology which showed maximum PCE. Currently, we assume a hindering effect followed by the impact on charge dissociation, transport, and/or recombination on the device performances due to the residual IL content within the $CH_3NH_3PbI_3$ NPs. Hence, performance improvement experiments are underway to ensure the complete removal of IL-contents from the $CH_3NH_3PbI_3$ NPs films.

3.4 Conclusions

We succeeded to prepare $CH_3NH_3PbI_3$ NPs with better morphology by introducing an ILs of varying wt % by using a simple spin-coating method. The results showed that the size and shape of NPs can be controlled or modified by using varying wt % of IL as additive in the DMF solvent medium. The small-sized $CH_3NH_3PbI_3$ NPs (~350 nm) with superior optical absorption properties have been obtained with 3 wt % of IL in the medium, as compared to the other compositions with wt % of 1, 7 and 10. As a result, a maximum PCE of 2.81% was obtained with the solar cell using 3wt % of IL in a solution.

<This page is intentionally left blank to indicate the chapter break>

Chapter Four: Viscosity Effects of Ionic Liquids as Additive on $CH_3NH_3PbI_3$ Nanoparticles and their Photovoltaic Properties

The following chapter describes the effect of viscosity of ionic liquids that are playing a significant role in controlling the morphology of resulting NPs.

4.1 Introduction

Organolead iodide perovskite such as methylammonium lead iodide ($CH_3NH_3PbI_3$) are attractive alternative to silicon-based solar cells due to its ability towards solution-processable and low cost, with a tunable bandgap and strong absorption coefficients for thin-film photovoltaic applications.[6] The efficiency of perovskites as a light-absorber material with 3.8 % conversion efficiency was first reported by Kojima *et al.*[11] The encouraging discovery has been continued further to achieve a notable 22.01 % conversion efficiency until the date.[24] Perovskite materials in particular show a various and rich form of functionalities and properties and find utility in several applications such as piezoelectrics,[80] thermoelectrics,[35] sensors,[28] photocatalysis,[32] and ferroelectrics.[30, 31] Semiconductor nanostructures are engaging lightweight harvesters as a result of their sub-wavelength features that enable quantum size effects, leading to very low reflection

and increased photon absorption to produce higher cell efficiency while not the necessity for added antireflection coatings. In addition, the large surface areas of nanotextured materials enable efficient energy conversion and charge-carrier recombination.[36]

Chemical synthetic techniques area unit advantageous for large-scale tailored production of anisotropic perovskite NPs, which may be promptly assembled into nanostructured bulk perovskite materials with highly efficient properties for practical applications. Many chemical synthetic strategies are developed to organize complex-shaped metal perovskite NPs, as well as the hydrothermal/ solvothermal techniques [42-44] and wet chemical synthesis[45] method are frequently used. On the other hand, researchers are interested in developing thin-film perovskite materials by easy, efficient, and precise techniques as an alternate to chemical synthesis.

Shahiduzzaman *et al*.[47, 48] reported the preparation of $CH_3NH_3PbI_3$ NPs for the first time using a simple spin-coating method by incorporating a small amount (1~10 wt %) of an ionic liquid (IL) 1-hexyl-3-methylimidazolium chloride in 25 wt % solution of $CH_3NH_3PbI_3$ in N,N-dimethylformamide (DMF) onto the compact-TiO_x/ITO substrates. The $CH_3NH_3PbI_3$ NP thin films were uniform and free of pin holes, and the excellent morphology was due to the addition of IL. Besides, another interesting highly efficient nanostructures is based on NWs of perovskite. Im *et al*.[49] stated an efficient $CH_3NH_3PbI_3$ NWs perovskite solar cells with a PCE of 14.71% was fabricated for the first time by a two-step spin-coating method. The preparation of $CH_3NH_3PbI_3$ NWs with the diameter range from 30 to 200 nm employing two-step spin-coating technique by coating the PbI_2 layer with an IPA solution of CH_3NH_3I (MAI) in the presence of a small amount (50~100

µL) of polar aprotic solvent (DMF). Moreover, Schmidt *et al*.,[50] demonstrated that the synthesis of highly crystalline 6 nm sized methylammonium lead bromide ($CH_3NH_3PbBr_3$) NPs by a straightforward spin-coating technique on a quartz substrate with the target of fabricating nanostructured perovskite to be used within the solar cells. Furthermore, Horvath *et al*. reported $CH_3NH_3PbI_3$ nanowires with mean diameter of 50 and 400 nm and length up to 10 µm have been prepared by a low-temperature solution process employing a slip-coating method [53] for solar cells. Likewise, Ha *et al.*[54] described the highly crystalline $CH_3NH_3PbI_3$ nano-platelets employing van der waals epitaxial growth followed by thermally intercalating methylammonium halides on muscovite mica. The resultant $CH_3NH_3PbI_3$ platelets show wonderful optical properties with an electron diffusion length of over 200 nm that is approximately twofold higher than that of the solution-processed film, suggesting significant promise in photovoltaics and optoelectronics.

The control of morphology and crystallization are the key challenges encountered in perovskite-thin films and have an effect on the quality of the resulting films. Since non-uniform morphology may limit device performance as a result of electrical shorting, or effects on charge dissociation/transport/recombination.[58-60] Ionic liquids (IL) are able to offer in the creation of nanostructured materials, because of their unique properties such as negligible vapor pressure, wide temperature range in liquid state, good dissolving ability, excellent electrochemical and thermal stability, high ionic conductivity, low toxicity, non-flammability etc. Owing to their outstanding properties, IL have been promoted effectively in the preparation of NPs.[81]

In the present study, we used a simple spin-coating technique to fabricate $CH_3NH_3PbI_3$ NPs by employing varying ILs, i.e. Tetrabutylammonium chloride [TBAM][CL], 1-benzyl-3-methylimidazolium chloride [BMIM][CL], and 1-allyl-3-methylimidazolium chloride [AMIM][CL] as morphology controller. The effect of varying ILs has also been investigated.

4.2 Experimental

Organic photovoltaic devices were fabricated on indium tin oxide (ITO) patterned glass substrates, which was pre-treated by oxygen plasma treatment for 20 min prior to use. Compact-TiOx layer was prepared by chemical bath deposition (CBD) according to the procedure represented by Kuwabara *et al*.[61] A compact-TiOx amorphous layer (30 nm) was obtained by employing one-time operation. Lead iodide (PbI_2; Tokyo Chemical Industry) (0.144 g) and methylammonium iodide (MAI) (0.05 g) were mixed in anhydrous DMF (615 µL) (Kanto Chemical, Tokyo, Japan) at 2.89:1 molar ratio followed by shaking at room temperature for 30 min to prepare a clear $CH_3NH_3PbI_3$ solution with the concentration of 25 wt%. At the concentration of 3 wt% of ionic liquids (IL; Sigma Aldrich, St. Louis, MO) were used as the morphology-controlling additive in the 25 wt% $CH_3NH_3PbI_3$ solution in DMF. The 25 wt % solution of $CH_3NH_3PbI_3$ was then spin-cast on the compact-TiO_x layer at 3000 rpm. A change in the film color, from transparent to deep peach, was observed throughout the spin-coating process. The resultant film was left for 30 min in a glove-box at RT to permit slow solvent evaporation, followed by annealing on a hot plate at 100 °C for 10 min to get a $CH_3NH_3PbI_3$ NPs film with a thickness of 200 nm. The hole-transporting layer (HTM) was placed by employing spin-

coating at 4000 rpm 2,2′,7,7′-tetrakis (*N*,*N*-di-*p*-methoxyphenylamine)-9,9′-spirobifluorene (spiro-OMeTAD) in chlorobenzene (0.058 M) containing 4-tert-butylpridine (0.19 M) and lithium bis (trifuluoromethylsulfonyl) imide (0.031M), tris [2-(1H-pyrazol-1-y1)-4-tert-butylpyridine] cobalt (III) tris [bis(trifluoromethysulfonyl) imide] (5.6 × 10-3 M) as dopants[63, 64]. The films were annealed at 70 °C for 20 min in hot plate. All the fabrication process was performed in an N_2-filled glove box. The films were transferred in a vacuum chamber and 100 nm thick silver electrodes were deposited on the spiro-OMeTAD layer with a pressure at around 2.83×10^{-4} pa.

4.3 Results and discussion

4.3.1 Chemical structures of ILs

The chemical structures of [TBAM][CL], [BMIM][CL], and [AMIM][CL] are shown in Fig. 4.1a-c, respectively. We introduced 3 wt % of IL to the solution of

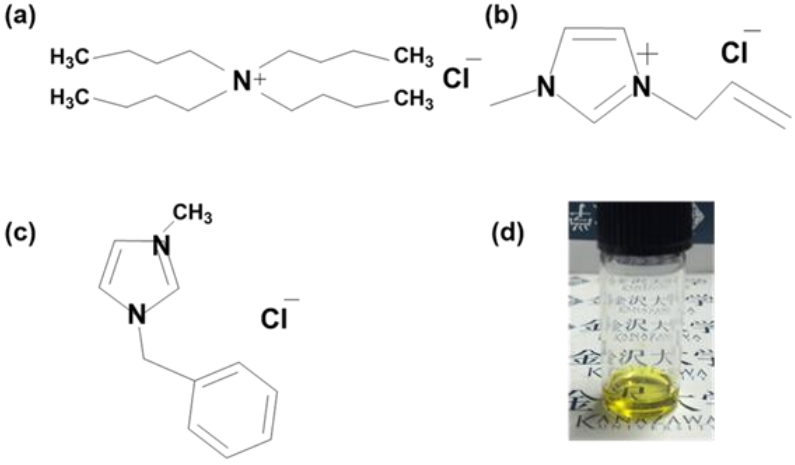

Figure 4.1. Chemical structure of different ILs of (a) [TBAM][CL], (b) [AMIM][CL], and (c) [BMIM][CL]; (d) mixture solution of $CH_3NH_3PbI_3$ and 3 wt % of IL.

$CH_3NH_3PbI_3$ in DMF as a morphology-controlling additive. The IL-doped solution of $CH_3NH_3PbI_3$ was a clear yellow-orange colored homogeneous solution having no aggregate or NPs (Fig. 4.1d).

4.3.2 Morphology

Figure 4.2b-d revealed that the three distinct types of nanostructures were distributed on the TiO_x substrates by employing three different types of ILs as shown in AFM images. Figure 4.2c-d showed the morphology of NPs with aggregated disc, rod like shapes, respectively, for [BMIM][CL], and [AMIM][CL] IL in solution, while the morphology was well controlled spherical shape and average diameter of 500 nm for [TBAM][CL] IL in solution as shown in Fig. 4.2b. The RMS roughness of the $CH_3NH_3PbI_3$ films was respectively 21.6, 22.2, and 23.1 nm at [TBAM][CL], [BMIM][CL], and [AMIM][CL] IL, respectively.

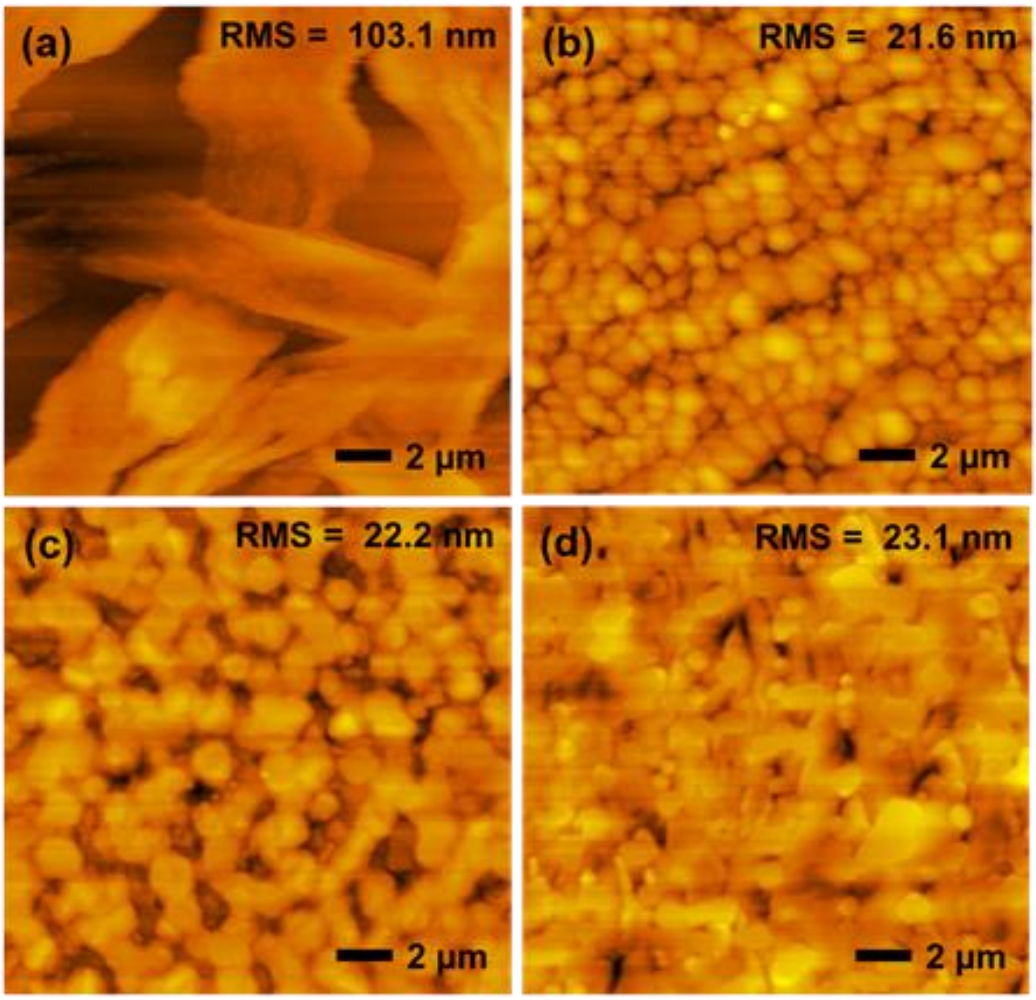

Figure 4.2. AFM images of (a) Perovskite film without IL and $CH_3NH_3PbI_3$ NPs in the presence of varying ILs: (b) [TBAM][CL], (c) [BMIM][CL], and (d) [AMIM][CL].

The film processed without IL is composed of non-uniform large crystals with ribbon like shape as shown in Fig. 4.2a. The RMS roughness value of the resulting film was 103.1 nm. This RMS data supports that the formation of a smooth uniform NP film by addition of IL in the spin-coating solution.

4.3.3 X-ray diffraction analysis

The XRD patterns of perovskite films for NPs as prepared by using varying ILs showed peaks, mostly the same as that of $CH_3NH_3PbI_3$ bulk as shown in Fig. 4.3. The

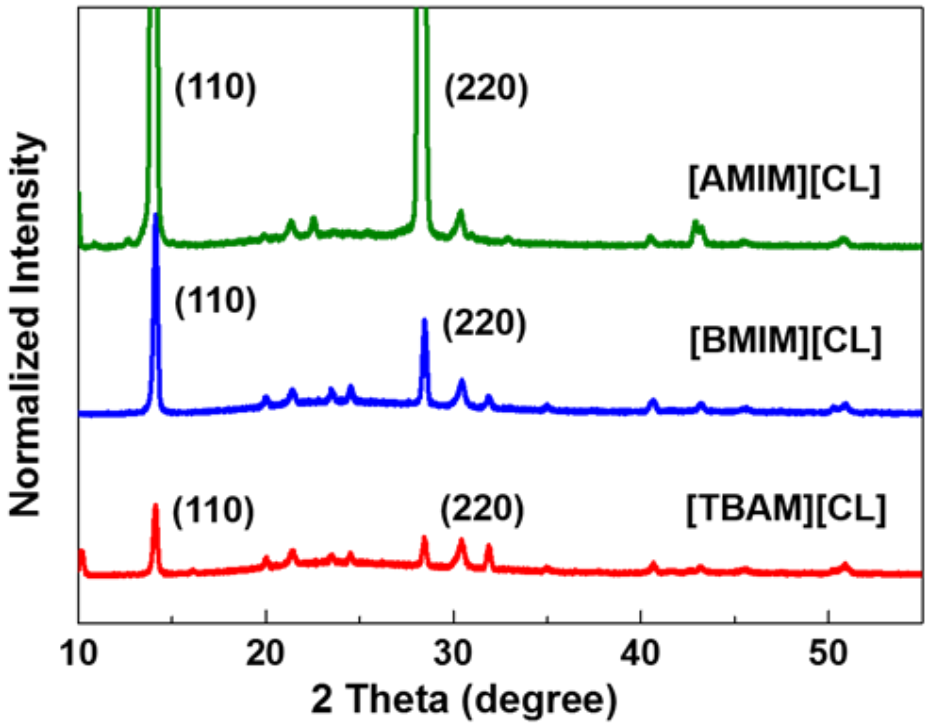

Figure 4.3. XRD patterns of $CH_3NH_3PbI_3$ NPs films processed with different ILs.

diffraction peaks with IL were obtained at 2θ = 14.01, 28.40 and 40.44 °, that were appointed severally to the (110), (220) and (224) crystal planes. The peak positions confirmed an orthorhombic crystalline structure.[59, 78] The mean crystalline sizes for the $CH_3NH_3PbI_3$ NPs, with [TBAM][CL], [BMIM][CL], and [AMIM][CL] ILs were 35.3, 34.0, and 33.5 nm, severally as estimated using Scherer's formula and the full-width at half-maximum of the (110) primary peak. The results indicated that the higher

crystallinity was observed by incorporation of [TBAM][CL] IL in solution as compare to other ILs based perovskite NPs.

4.3.4 FTIR analysis

The presence of IL at intervals the $CH_3NH_3PbI_3$ films were confirmed by the FTIR spectra as shown in Fig. 4.4. The FTIR reveals that the IL molecules are adsorbed on the surface of the $CH_3NH_3PbI_3$ NPs. It was indicated by the absorption bands in the region of 2,650 to 3,000 cm^{-1} that are allotted to C–H stretching of the imidazolium ring. The observation was the same as a pervious report by Ayi *et al.*[69] that confirmed that the molecules of IL were absorbed on the surface of the particles and provided protection throughout the formation of nanostructured particles. The bands at 3,200–3,300 cm–1 in conjunction with the bands between 1,500 and 1,700 cm-1 were attributed to N-H stretching and bending vibrational bands. The N-H bending vibration revealed that IL molecules intercalated with $CH_3NH_3PbI_3$ NPs films. The findings of each of the C-H and N-H deformation modes within the $CH_3NH_3PbI_3$ NPs film assured the retention of IL molecules. A series of 8 ILs was tested, including [TBAM][CL], [BMIM][CL], [AMIM][CL], 1-hexayl-3-methylimidazolium chloride ([HMIM][CL]), 1-ethyl-3-methylimidazolium acetate ([EMIM][AC]), 1-ethyl-3- methylimidazolium bis (trifluoromethanesulfonyl) imide ([EMIM][TFSI]),

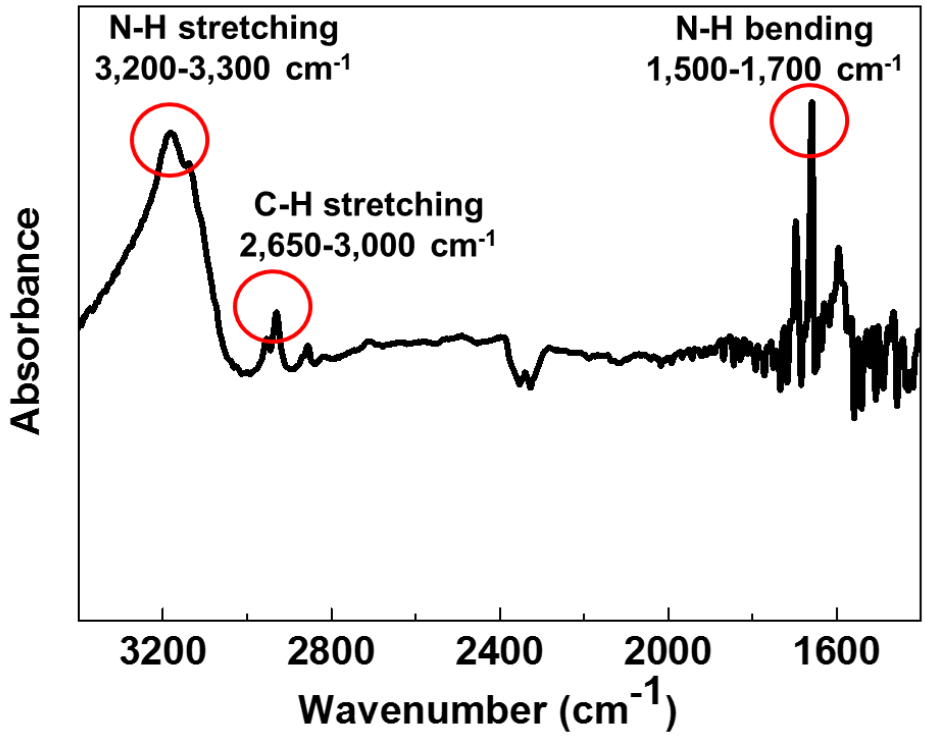

Figure 4.4. The FTIR spectra of $CH_3NH_3PbI_3$ NPs film.

1, 3-didecyl-2-methylimidazolium chloride ([DMIM][CL]), and Trihexytetradycyl phosphonium dicyanamide ($[P_{6,6,6,14}]$[DCA]). Among 8 ILs, [EMIM][AC], [EMIM][TFSI], [DMIM][CL], and $[P_{6,6,6,14}]$[DCA] are not dissolved in 25 wt % solution of $CH_3NH_3PbI_3$ in DMF, thus not forming NPs. We measured the viscosity of 8 ILs and found low viscosity of ILs along with completely dissolved in $CH_3NH_3PbI_3$ solution are playing a significant role in forming NPs. Viscosity parameter of several ILs has been presented in Table 4.1. The viscosity of ILs is a very important parameter due to its strong effect on resultant solution. Lower viscosity means the lower intermolecular attractive forces of IL additive to overcome for the liquid molecules to separate. The

resulting uniform thin film with good morphology was due to the low viscosity of IL and completely dissolve in $CH_3NH_3PbI_3$ solution.

Table 4.1. Viscosity measurement data for different ILs (3 wt %) in DMF.

Ionic Liquids (ILs)	Viscosity	Torque	Temp.	Dissolve in perovskite solution
[TBAM][CL]	0.89	29.2	24.3	Yes
[BMIM][CL]	0.90	29.3	24.2	Yes
[AMIM][CL]	0.95	32.2	24.4	Yes
[HMIM][CL]	0.89	29.2	24.3	Yes
[EAMIM][AC]	1.08	35.3	24.4	Not dissolve
[EMIM][TFSI]	2.53	80.1	24.8	Not dissolve
[DMIM][CL]	1.50	37.2	24.4	Not dissolve
$[P_{6,6,6,14}]$[DCA]	1.80	40.1	24.4	Not dissolve

4.3.5 UV-vis analysis

The UV-vis spectra of $CH_3NH_3PbI_3$ NP films with varying IL cast on glass/ITO/ compact-TiO_x substrates are shown in Fig. 4.5. The optical properties of $CH_3NH_3PbI_3$ NPs depend on the size and the shape of the resultant particles. The absorption peaks were observed at around 480, 500, and 530 nm in the system with [BMIM][CL], [TBAM][CL], and [AMIM][CL], respectively, which corresponded to NPs, in accordance with the observation from Ayi, *et al.*[69] and shahiduzzaman *et al.*[48] The sharp absorption peak for the NPs also indicated a fairly uniform shape and size of NPs.

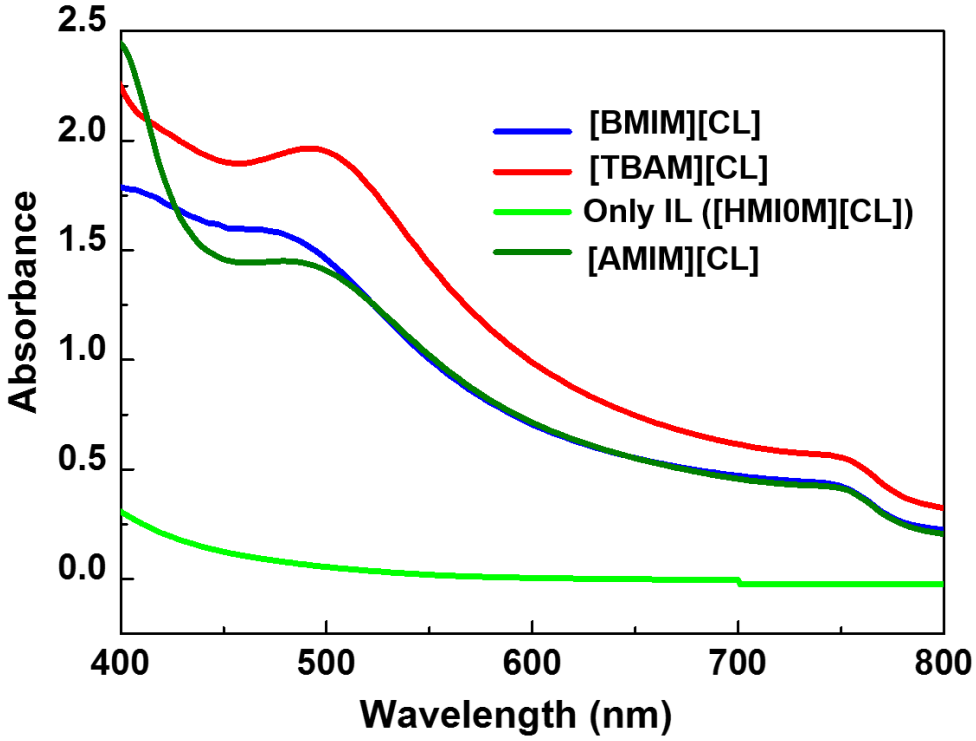

Figure 4.5. UV-vis spectra of $CH_3NH_3PbI_3$ NPs films processed with different ILs.

In our previous study[47, 48], we proposed formation mechanism of $CH_3NH_3PbI_3$ NPs films. Addition of the IL in the reaction media facilitates the formation of homogenous nucleation sites and prevents rapid crystal formation of $CH_3NH_3PbI_3$. The resultant NPs thin film with good morphology as shown in Fig. 4.2 (b, c, and d) was due to the addition of ILs, which possesses high boiling point, extremely low vapor pressure, high ionic conductivity, and thermal stability.

4.3.6 Photovoltaic properties

Figure 4.6a present the schematic device structure of PHJ $CH_3NH_3PbI_3$ NPs solar cells. The current density *versus* voltage (*J-V*) characteristics of $CH_3NH_3PbI_3$ NPs solar cells as obtained by employing varying ILs ([TBAM][CL], [BMIM][CL], and [AMIM][CL]) and were measured at AM 1.5G illuminations as shown in Figure 4.6b.

Table 4.2. Performance of cells with the structure ITO/compact-TiO_x/$CH_3NH_3PbI_3$ NP/Spiro-OMeTAD/Ag.

Varying ILs	J_{sc} (mA/cm^2)	V_{oc} (V)	FF (%)	PCE (%)
[TBAM][CL]	8.49	0.91	0.51	3.93
[BMIM][CL]	7.77	0.90	0.50	3.56
[AMIM][CL]	4.57	0.86	0.42	1.34

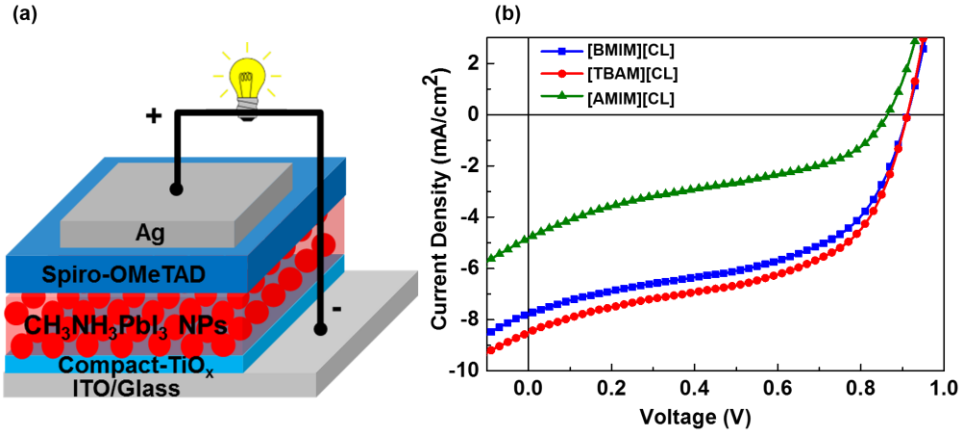

Figure 4.6. (a) Device configuration of $CH_3NH_3PbI_3$ NPs solar cells; (b) The *J-V* characteristics achieved for the solar cells based on $CH_3NH_3PbI_3$ NPs.

The photovoltaic devices prepared with [BMIM][CL] IL-doped $CH_3NH_3PbI_3$ NPs showed a short-circuit current density (J_{sc}) of 7.77 mA/cm^2. An increase in the J_{sc} value to 8.49 mA/cm^2 was observed for the photovoltaic device prepared using [TBAM][CL] IL-doped $CH_3NH_3PbI_3$ NPs, while the J_{sc} value is decreased to 4.57 mA/cm^2 for [AMIM][CL] doping of IL. The power conversion efficiency (PCE) is also followed the similar trend of the J_{sc} values, showing a higher PCE of 3.93 % for the photovoltaic device of [TBAM][CL] IL-doped $CH_3NH_3PbI_3$ NPs. All the parameters measured to study the performances of solar cells are summarized in Table 4.2. We achieved $CH_3NH_3PbI_3$ NPs by adding [TBAM][CL] IL, having more uniform shape, size, morphology which showed maximum PCE. Currently, we assume a hindering effect followed by the impact on charge dissociation, transport, and/or recombination on the device performances due to the residual IL content within the NPs films. Thus, the performance enhancement investigates are underway to ensure the complete removal of IL-contents from the $CH_3NH_3PbI_3$ NPs films.

4.4 Conclusions

We well succeeded to prepare $CH_3NH_3PbI_3$ NPs with improved morphology by adding varying ILs employing a spin-coating technique. The results showed that the size and shape of NPs can be controlled or modified by using low viscosity of IL as the morphology controller in the DMF solvent medium. The uniform shape, and size of $CH_3NH_3PbI_3$ NPs with the respective diameter of 500 nm along with higher crystallinity, superior optical absorption properties are obtained with [TBAM][CL] IL in the medium, as compared with other ILs of [BMIM][CL], and [AMIM][CL]. Hence, the highest PCE

of 3.93 % was achieved with the solar cell prepared by incorporating [TBAM][CL] IL in a solution.

<This page is intentionally left blank to indicate the chapter break>

Chapter Five:
Enhanced photovoltaic performance of perovskite solar cells *via* modification of surface characteristics using a fullerene interlayer

The following chapter describes the use of fullerene (C_{60}) interlayers with thickness of 0, 3, 7, and 10 nm between TiO_x and $CH_3NH_3PbI_3$ layers and investigate the effect of the thickness of the C_{60} interlayer on the morphology and power conversion efficiency of the resulting devices.[82]

5.1 Introduction

Hybrid organometal halide perovskites such as methylammonium lead iodide ($CH_3NH_3PbI_3$) are attracting considerable attention as energy-efficient light-absorbing materials for photovoltaic applications because they are solution processable and cost effective, with a tunable bandgap and strong absorption coefficients.[6] Thin film organic–inorganic hybrid halide perovskites, first reported by Kojima *et al.*,[11] show promise as light-absorption components for solar cells, achieving an initial conversion efficiency of 3.8%. This encouraging discovery led to hybrid halide perovskites being included as light harvesters in solar cells that showed conversion efficiencies of up to 20.1%.[74] Many planar heterojunction (PHJ) perovskite solar cells in which the perovskite layer is inserted between a hole-transport layer of poly(3,4-

ethylenedioxythiophene):poly(styrenesulfonate), and an electron-transport layer of [6,6]-phenyl-C_{61}-butyric acid methyl ester (PCBM) have been reported.[58, 60, 76, 83]

PHJ perovskite solar cells have attracted more interest than mesostructured perovskite solar cells for photovoltaic applications. This is because preparation of high-quality mesostructured films and compact titanium dioxide (TiO_2) layers involves high-temperature processes, which limits their application in simpler architectures.[15, 75] Several groups have circumvented this limitation by developing PHJ perovskite solar cells without a mesoporous TiO_2 layer.[76, 78] In addition, wang *et al*.,[21] has been reported that a low-temperature processed nano-composites of pristine graphene nanoflakes and anatase-TiO_2 nanoparticels as an electron collection layer, which significantly enhanced the photovoltaic performance of perovskite solar cells.

Kuwabara *et al*.[61] deposited a uniform, compact and air-stable amorphous titanium oxide (TiO_x) film as an electron collection layer for solar cells via chemical bath deposition (CBD) at low temperature, demonstrating the utility of this inexpensive, simple and scalable technique. In this assembly, the compact-TiO_x layer formed good physical and electronic contacts with the perovskite layer. In addition, the compact-TiO_x layer formed at low temperature, which allowed direct contact between the perovskite layer and indium tin oxide (ITO) cathode. The resulting increase in charge carrier recombination led to a large leakage current as well as decreases in short-circuit current density (J_{sc}) and fill factor (FF).

Increasing the electron transport between perovskite and compact-TiO_x layers has become an important goal to collect more electrons and enhance the efficiency of PHJ

perovskite solar cells. The surface energy of devices naturally varies following interface modification,[84] and has its own effect on device performance. In the case of PHJ solar cells, morphology can play a major role in tuning surface energy.

In this work, we modify the surface characteristics of air-stable amorphous TiO_x layers by inserting fullerene (C_{60}) as an interlayer in PHJ solar cells and investigate the effect of the thickness of the C_{60} interlayer on the morphology and power conversion efficiency (PCE) of the resulting devices. Varying the thickness of the C_{60} interlayer between 0 and 10 nm allows us to control the surface energy of the cells over a wide range of values. A correlation between the surface energy and PCE in PHJ solar cells is established, offering the possibility to enhance device performance. PCE is enhanced by the increased photocurrent that is obtained by tuning surface energy through optimization of morphology.

5.2 Experimental

5.2.1 Preparation of compact-TiO_x films by chemical bath deposition (CBD):

Indium tin oxide (ITO)-patterned glass substrates, which were pre-treated in oxygen plasma for 20 min prior to use. Compact-TiO_x films were prepared by CBD according to the procedure described by Kuwabara *et al.*[61] In brief, a titanium (IV) oxysulfate ($TiOSO_4$) solution was added to a dilute aqueous solution of hydrogen peroxide (H_2O_2) and then the mixed solution was diluted to 50 mL with ultrapure water. The concentrations of H_2O_2 and $TiOSO_4$ were adjusted to 0.03 M, respectively. This solution was transferred to a screw-top vial to use as the reaction bath for substrate deposition. The glass side of the ITO substrate was covered with an imide tape to avoid extra

deposition of TiO_x, and then the ITO substrate was immersed in the bath at 80 °C. The solution became cloudy during heating and after an appropriate dipping time starting from this clouding point, the ITO substrate was removed from the bath. The as-deposited TiO_x film on the ITO substrate was cleaned by ultrasonication in water for 3 min, and then heated on a hot plate at 150 °C in air for 1 h. A thin amorphous compact-TiO_x layer (30 nm thick) was obtained by this process. We repeated this procedure once more to obtain a 60-nm-thick amorphous TiO_x layer. A C_{60} interlayer with a thickness of 0, 3, 7, or 10 nm was then thermally evaporated on the TiO_x amorphous layer in a vacuum chamber at 2.7×10^{-4} Pa.

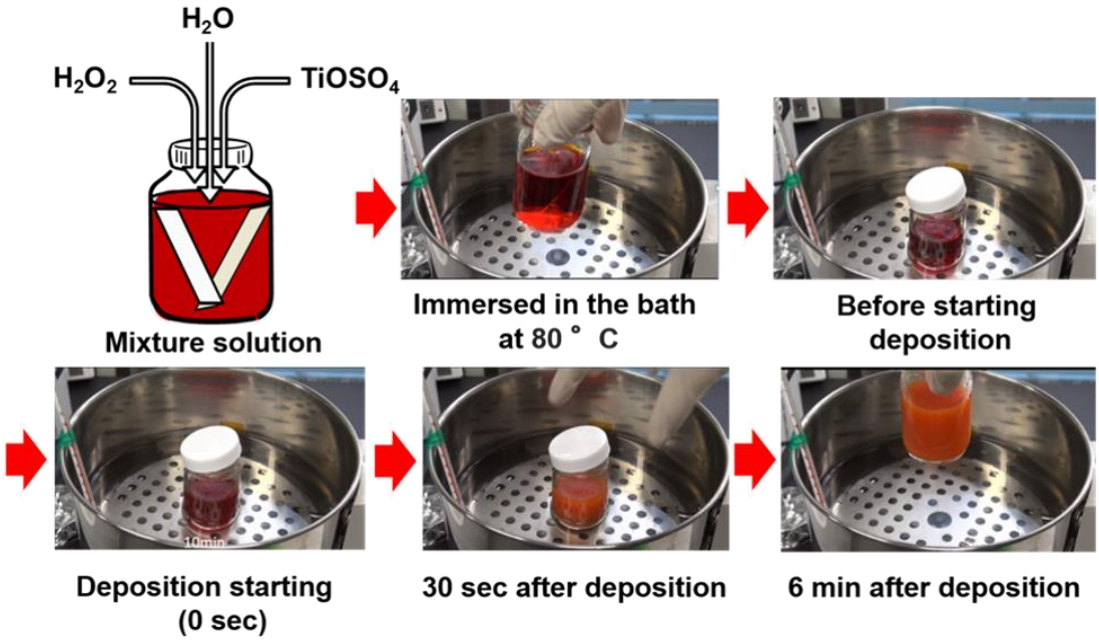

Figure 5.1. Photographs before and after the hydrolysis in the CBD for the deposition of titanium oxide (TiO_x).

5.2.2 Solar cells device fabrication

Then, PbI_2 (0.144 g) and methylammonium iodide (MAI) (0.05 g) were dissolved in N,N-dimethylformamide (615 µL) by shaking at room temperature for 30 min to produce a clear $CH_3NH_3PbI_3$ solution with a concentration of 25 wt %. The solution was then spin cast onto the C_{60}/TiO_x layer. The resulting films were left to dry at room temperature in a glove box for 30 min to allow slow solvent evaporation. The films were then thermally annealed at 100 °C for 10 min in a glove box under an inert environment. The hole-transporting layer consisting of 2,2′,7,7′-tetrakis(N,N-di-p-methoxyphenylamine)-9,9′-spirobifluorene (spiro-OMeTAD) in chlorobenzene (0.058 M) containing 4-*tert*-butylpyridine (0.19 M), lithium bis(trifluoromethylsulfonyl)imide (0.031M), and tris[2-(1H-pyrazol-1-yl)-4-*tert*-butylpyridine]cobalt(III) tris[bis(trifluoromethylsulfonyl)imide] (5.6×10^{-3} M) as dopants was deposited by spin coating at 4000 rpm.[63, 64] The films were annealed at 70 °C for 20 min on a hot plate in the glove box. Finally, the films were transferred in a vacuum chamber and 100-nm-thick silver electrodes were deposited on the spiro-OMeTAD layer at 2.83×10^{-4} Pa. The active device area was 4 mm^2. The current density *versus* voltage (*J*-*V*) characteristics of the cells were measured under simulated AM 1.5G solar illumination.

5.3 Results and discussion

5.3.1 Schematic diagram of PHJ perovskite solar cells and energy level of materials

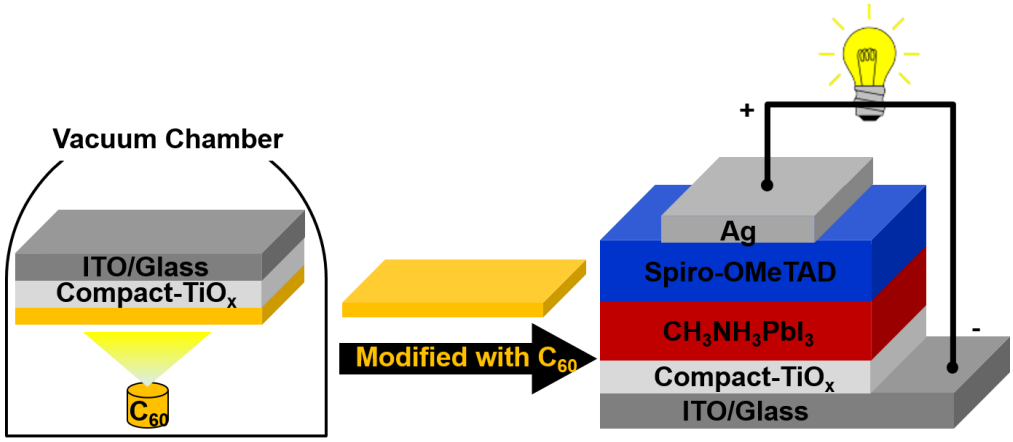

Figure 5.2. Presents schematic illustration of the device structure of PHJ perovskite solar cells.

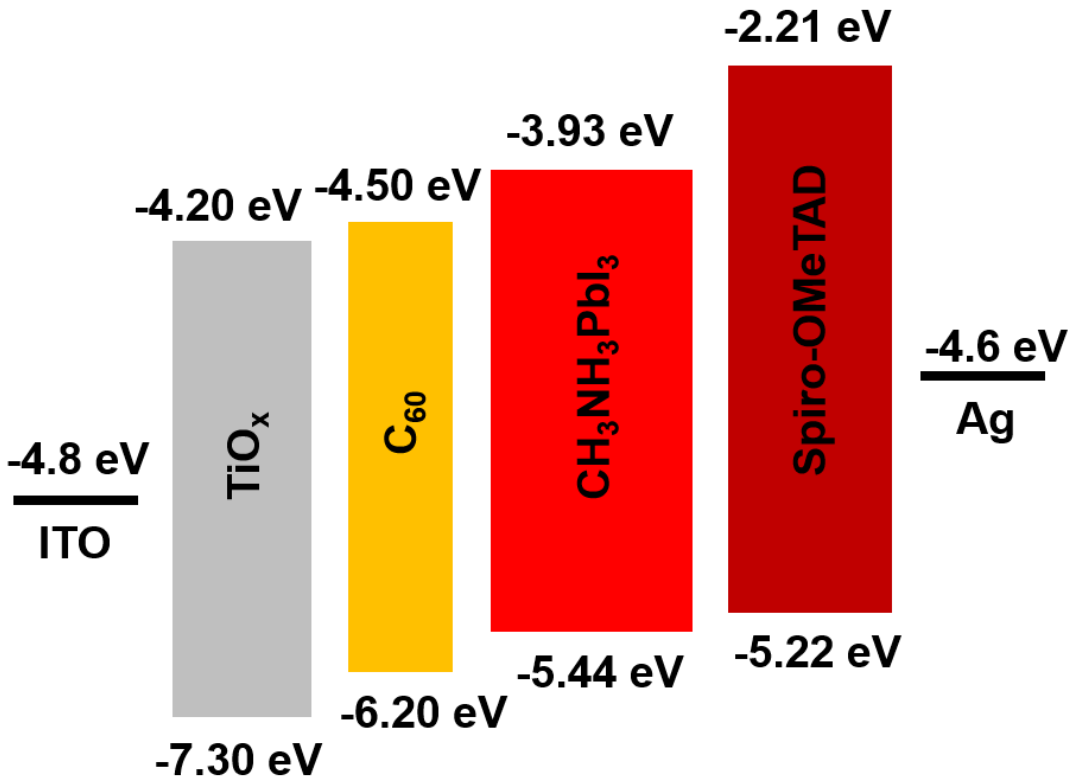

Figure 5.3. Lowest unoccupied molecular orbital (LUMO) and highest occupied molecular orbital (HOMO) energy levels of the materials and work functions of ITO and Ag electrodes in the perovskite hybrid solar cells.

5.3.2 Fabrication steps of PHJ perovskite solar cells

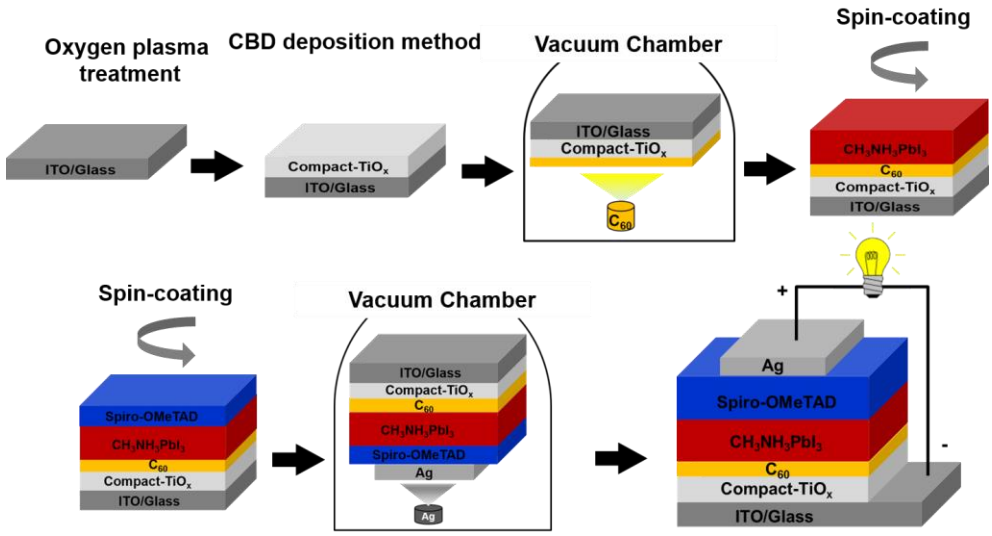

Figure 5.4. Schematic diagram of PHJ perovskite solar cells.

5.3.3 Morphology and crystallinity

The atomic force microscope (AFM) image in Fig. 5.5(a) reveals that a uniformly distributed, compact-TiO_x amorphous layer with a thickness of 60 nm was obtained from two deposition cycles. The root-mean-square (RMS) roughness of this film was 4.21 nm. Fig. 5.5(b), (c) and (d) show the uniformly distributed morphologies of the C_{60} interlayers with thicknesses of 3, 7 and 10 nm, respectively, which have respective RMS roughness values of 4.12, 3.31 and 8.28 nm. The RMS roughness was smoother with 7 nm C_{60} film as compare to the other film thickness. The better morphology of 7 nm C_{60} interlayer can be collected electrons more efficiently at the $CH_3NH_3PbI_3$/compact-TiO_x interface, thus degrading the interfacial barrier. As compared to other conditions, the morphology becomes more rough (Figure 5.5 b and d), which is expected to reduce the interfacial area. The resultant reduction of charge generation then will degrade the J_{SC} (and hence

also the PCE). The variation of the device performance with respect to the surface energy observed in Figure 5.9, 5.10, and 5.11 can be explained in terms of morphology. The films without C_{60} showed incomplete surface coverage and were composed of non-uniform large ribbon-like crystals (Fig. 5.6(a)).

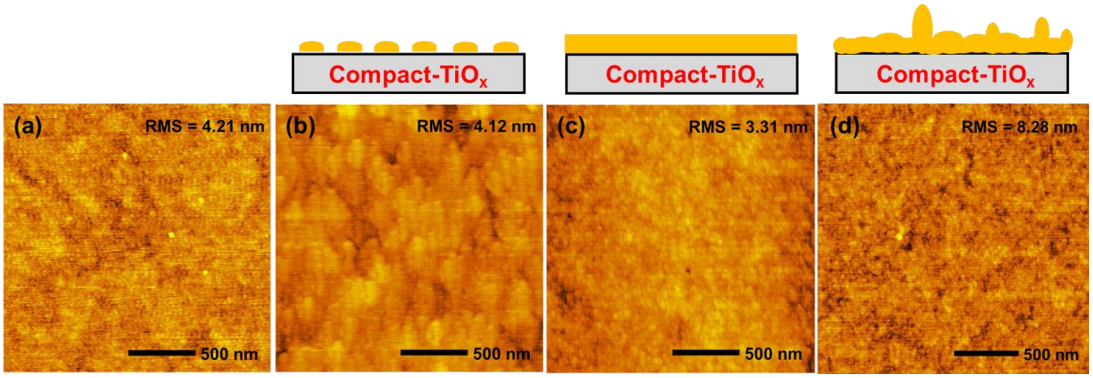

Figure 5.5. The AFM images of (a) TiO_x film; and C_{60} with varying thickness (nm): (b) 3, (c) 7, and (d) 10.

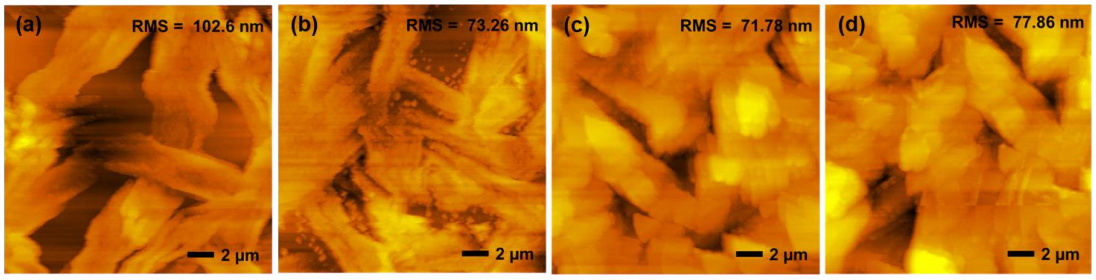

Figure 5.6 The AFM images of the perovskite film prepared in the presence of varying C_{60} thickness (nm): (a) 0, (b) 3, (c) 7, and (d) 10.

RMS roughness values of the $CH_3NH_3PbI_3$ films with and without a 7-nm-thick C_{60} layer were 71.78 and 102.60 nm, respectively, so the 7-nm-thick C_{60} interlayer decreased the roughness of the overlying $CH_3NH_3PbI_3$ film. To produce highly efficient PHJ perovskite solar cells, it has been shown that uniform morphology and high crystallinity are very important.[72, 85] In this respect, both the morphology (Fig. 5.5c) and crystallinity (Fig. 5.7)

of perovskite solar cells have been improved by inclusion of a C_{60} interlayer. The enhanced crystallization facilitates the more charge transfer efficiency between interlayer and the $CH_3NH_3PbI_3$.

X-ray diffraction (XRD) patterns of the perovskite films formed with and without a C_{60} interlayer are depicted in Fig. 5.7. Diffraction peaks were observed at $2\theta = 14.01°$, 28.40°, 31.91°, and 40.74° for films both with and without C_{60}, and are assigned to the (110), (220), (310) and (224) crystal planes, respectively, of $CH_3NH_3PbI_3$. These peak positions are consistent with an orthorhombic crystalline structure in both films.[78] It should be noted that there was no peak from PbI_2 at 12.65° in either of the XRD patterns, which indicated the complete consumption of PbI_2. The mean crystallite sizes for the perovskite crystals formed with and without a C_{60} interlayer were 37.8 and 36.5 nm, respectively, as estimated from the full width at half-maximum of the (110) peaks using the Scherrer formula.

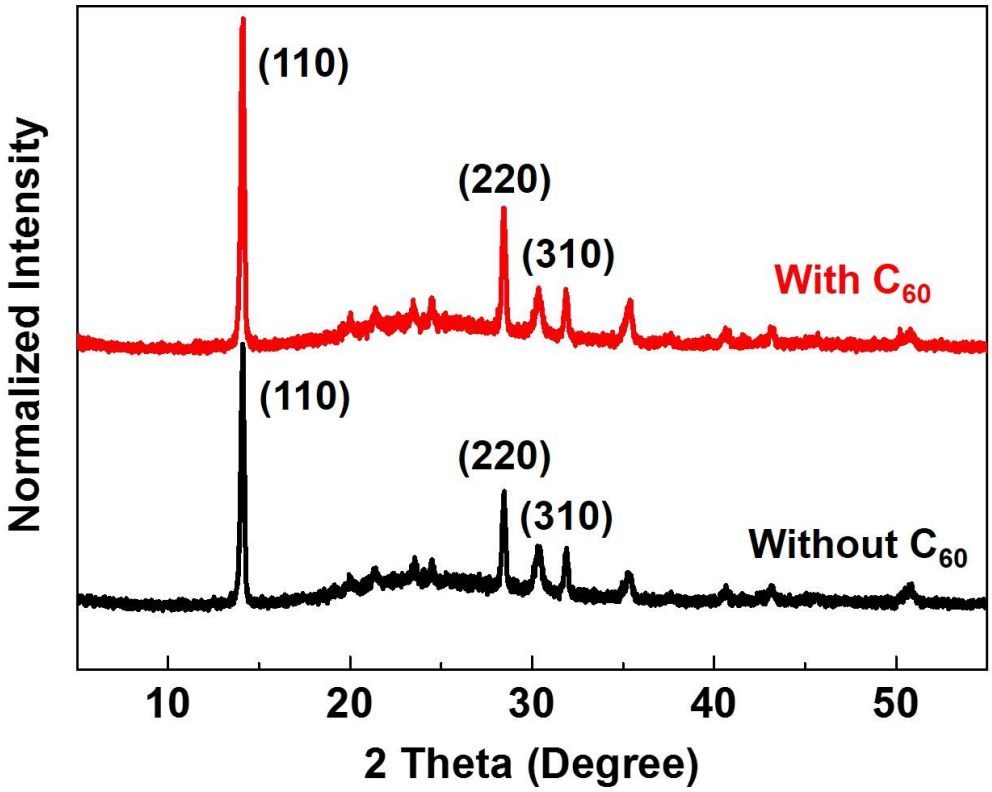

Figure 5.7. XRD patterns of $CH_3NH_3PbI_3$ films with and without a C_{60} interlayer.

5.3.4 Contact angle measurements and the relationship between photovoltaic properties and surface energy

The water droplets shown in Fig. 5.8(a-d) illustrate how surface treatment changed the surface energy from high to low by varying the thickness of the C_{60} layer on TiO_x. These changes in surface energy have been used to control the wettability and optimize the morphology of the films. Water contact angles were measured at three different points on each film surface and an average value is reported. The water contact angle of TiO_x prepared without C_{60} was moderate (10.2°). The water contact angle was lower for the 7-nm-thick C_{60} interlayer (8°) than those of the other thicknesses such as 3 nm (12.2°) and

10 nm (10.6°) because of the more uniform morphology of the 7-nm-thick C_{60} interlayer, as was evident in AFM images. The poor wettability of films might be another avenue to further improve the PCE of solar cells. Using C_{60} interlayers of different thickness, the surface energy of the compact-TiO_x layer could be controlled between 43 and 51.5 mJ m^{-2}. The surface energy of a TiO_x film without C_{60} was 56 mJ m^{-2}. The actual values of the contact angles used to calculate the surface energy of each film are provided in (Table 5.1).

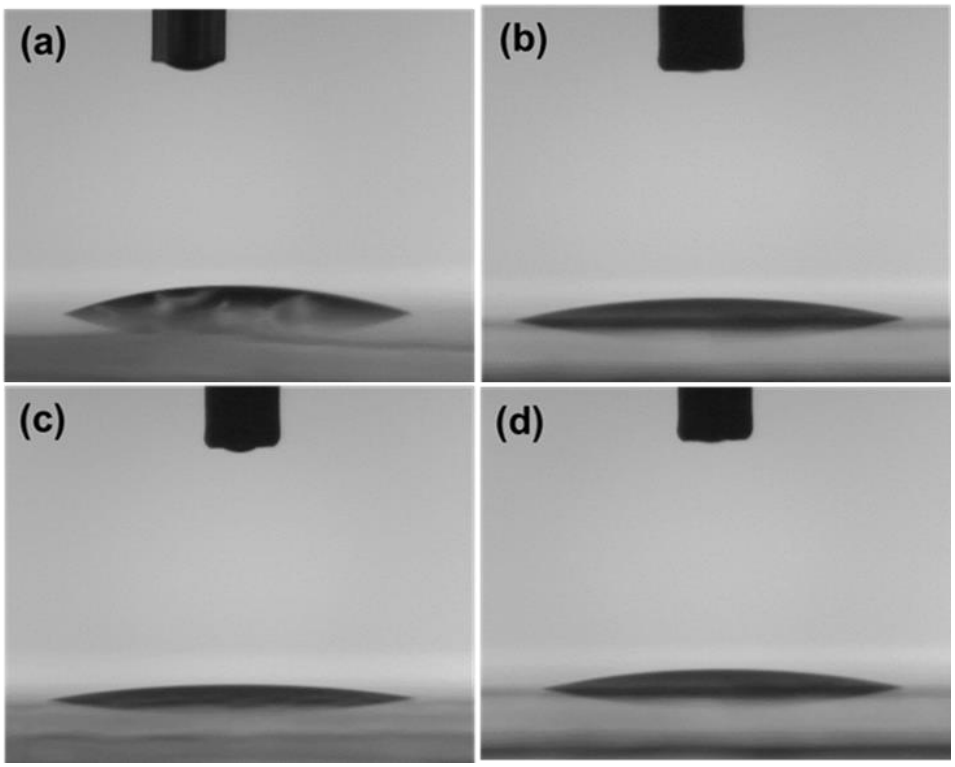

Figure 5.8. Optical images of the contact angles of a (a) TiO_x film, and C_{60} layers with a thickness of (b) 3, (c) 7, and (d) 10 nm.

Table 5.1. Contact angles and surface energy values.

Film Thickness / nm		Contact Angle (θ) / °			Surface free energy / mJ m^{-2}		
		Formamide (FA)	H_2O	(Diiodomethane) DIM	LW	AB	γ^{total}
0	ITO_TiO_x	7.6	10.2	13.4	50	6.5	56.5
3	ITO_TiO_x_C_{60}	74.2	12.2	91	43	0	43
7	ITO_TiO_x_C_{60}	45.0	8.0	76.5	50.3	1.2	51.5
10	ITO_TiO_x_C_{60}	59.5	10.6	86	48.1	0	48.1

Surface energy calculation is presented in appendix v.

$CH_3NH_3PbI_3$ solar cells with the structure shown in Fig. 5.2 were then fabricated to evaluate device performance as a function of surface energy. Figure 5.9 (a), (b) and (d) show J_{sc}, FF and PCE of the cells, respectively, as a function of TiO_x surface energy in the range from 43 to 51.5 mJ m^{-2}. J_{sc}, FF and PCE all exhibited the same overall trend with respect to surface energy, with maximum values at an intermediate surface energy. The highest PCE (9.51%), J_{sc} (15.17 mA/cm^2) and FF (0.69) were observed for the device with a surface energy of 51.5 mJ m^{-2} containing a 7-nm-thick C_{60} interlayer. The optimized morphology obtained by surface-energy modification enhanced the photocurrent of the corresponding solar cell. In contrast, the open circuit voltage (V_{oc}) did not show any significant changes with respect to the surface energy, as shown in Figure 5.9b. AFM analysis verified the correlation between the surface energy and phase morphology of the PHJ solar cells.

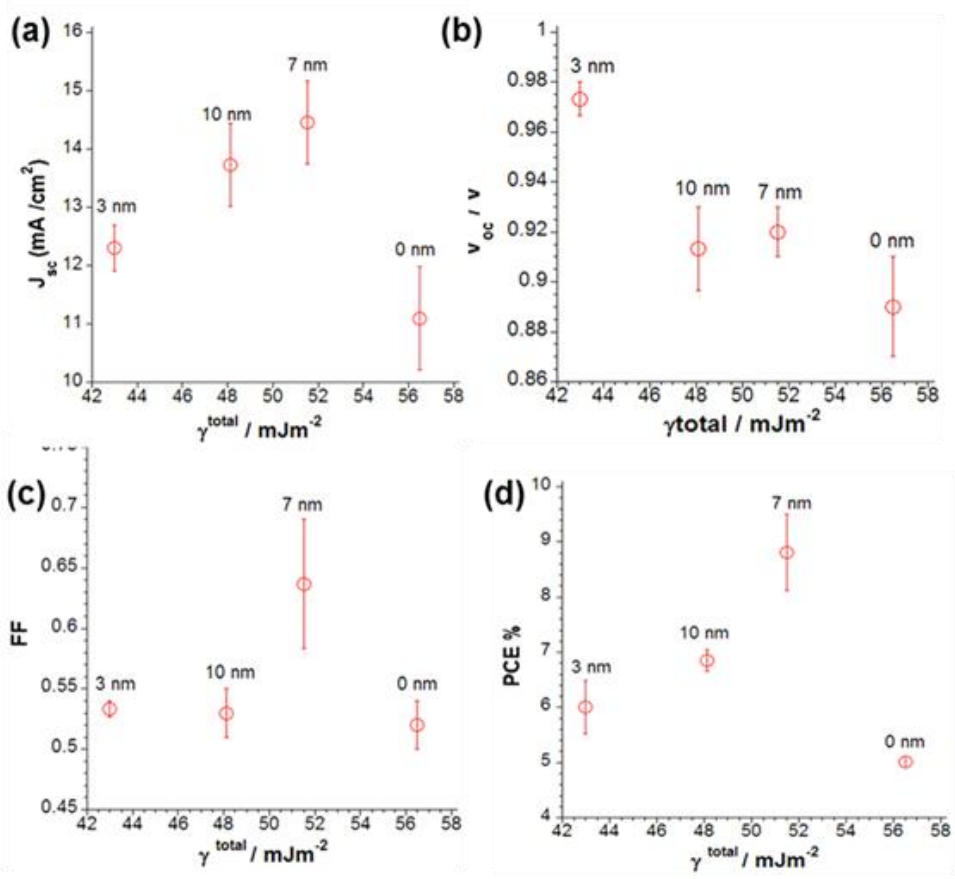

Figure 5.9. Characteristics of $CH_3NH_3PbI_3$ solar cells as a function of the surface energy of the C_{60} layer: (a) short-circuit current density, J_{sc}, (b) open-circuit voltage, V_{oc}, (c) fill factor, FF, and (d) power conversion efficiency, PCE. Error bars show plus-or-minus one standard deviation from the mean.

5.3.5 Photovoltaic Characterization

Figure 5.10 further compares the device characteristics of the PHJ $CH_3NH_3PbI_3$ solar cells by showing *J-V* curves measured for cells with and without a C_{60} interlayer. A solar cell with similar architecture fabricated using PCBM as the interlayer instead of C_{60} was used as a reference. The device without a C_{60} interlayer exhibited a J_{sc} of 11.98 mA/cm^2, V_{oc} of 0.91 V, FF of 0.49, and PCE of 5.12%. Such poor device performance

was caused by a contact barrier that prevented efficient electron injection at the interface between $CH_3NH_3PbI_3$ and TiO_x, which led to a large leakage current and the recombination of charge carriers. Conversely, incorporation of a 7-nm-thick C_{60} interlayer caused J_{sc} to increase to 15.17 mA/cm^2, while it was 13.47 mA/cm^2 for the device with a 10-nm-thick PCBM interlayer. The FF was enhanced from 0.49 to 0.69 and 0.55 upon the inclusion of 7-nm-thick C_{60} and 10-nm-thick PCBM layers, respectively. The enhancement of J_{sc} and FF induced by the 7-nm-thick C_{60} interlayer was attributed to the lowering of the injection barrier at the interface between $CH_3NH_3PbI_3$ and compact TiO_x, which decreased the series resistance from 25.75 to 7.39 Ωcm^2.

This result indicates that the incorporation of a C_{60} interlayer on the TiO_x/ITO glass substrate enhanced charge carrier extraction from the perovskite layer to the ITO electrode, which led to the improvement of J_{sc} and PCE of the resulting films. PCE increased considerably from 5.12% to 9.51% upon the insertion of a 7-nm-thick C_{60} interlayer between the $CH_3NH_3PbI_3$ and TiO_x layers.

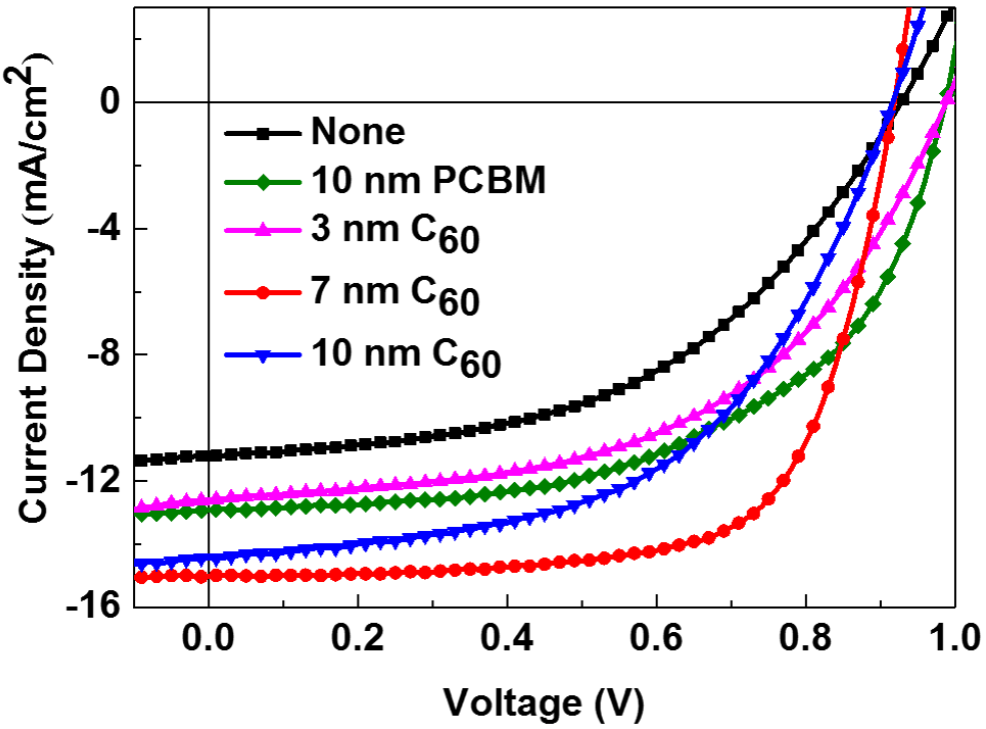

Figure 5.10. *J-V* characteristics of the device with and without C_{60} interlayer for different thicknesses.

Incident photon-to-current conversion efficiency (IPCE) curves of devices with and without interlayers are presented in Fig. 5.11. The enhanced PCEs of the devices with a C_{60} or PCBM layer are consistent with the higher IPCE values of these devices than that of the cell without an interlayer. The photocurrents determined from the IPCE data were 11.02, 13.12 and 15.17 mA/cm^2 for cells without an interlayer, and with an interlayer of PCBM (10 nm) and C_{60} (7 nm), respectively. The PHJ $CH_3NH_3PbI_3$ solar cells exhibited

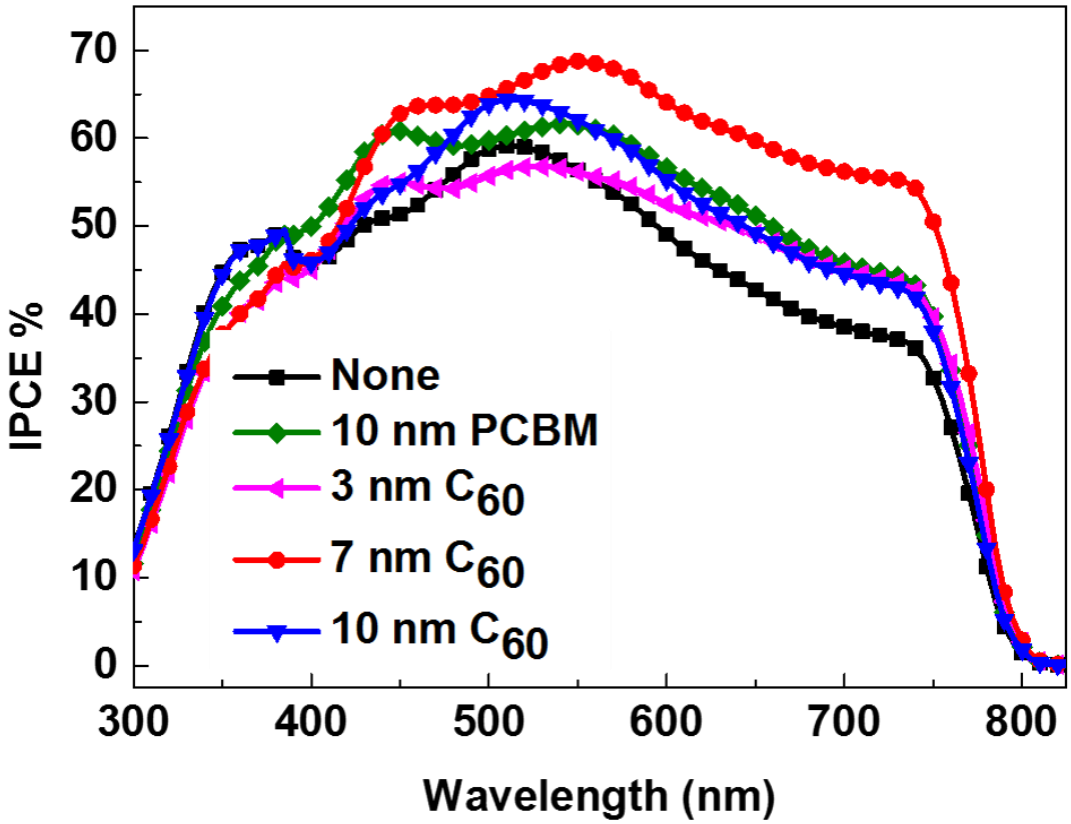

Figure 5.11. Incident photon to current conversion efficiency (IPCE) spectra of the device with and without C_{60} interlayer for different thicknesses.

a spectral response that extended from the visible to the near-infrared region with a broad, flat peak intensity of absorption around 60%–70% at approximately 380–750 nm. The higher IPCE value of the device with a 7-nm-thick C_{60} layer in the visible-to-near-infrared wavelength region than those of the other devices suggests that the 7-nm-thick C_{60} interlayer collect electrons more efficiently at the $CH_3NH_3PbI_3/TiO_x$ interface because it successfully lowers the interfacial energy barrier.

Table 5.2. Performance of cells with the structure ITO/compact-TiO_x/C_{60} or $CH_3NH_3PbI_3$/Spiro-OMeTAD/Ag.

Interlayer	J_{sc} (mA/cm^2)	V_{oc} (V)	FF (%)	PCE (%)	Rs (Ω.cm^2)
None	11.98	0.91	0.49	5.12	25.75
10 nm of PCBM	13.47	0.98	0.55	7.04	10.32
3 nm of C_{60}	12.70	0.98	0.52	6.49	18.49
7 nm of C_{60}	15.17	0.93	0.69	9.51	7.39
10 nm of C_{60}	14.44	0.91	0.53	7.04	15.03

The effect of incorporation of a C_{60} interlayer on the performance enhancement of PHJ perovskite solar cells was clarified by including C_{60} interlayers of different thickness. The parameters of these solar cells are summarized in Table 5.2. The results from these measurements strongly supported our concept that manipulating the surface energy of the C_{60} interlayer can enhance device performance. The above discussion indicates a clear relationship between surface energy, perovskite film morphology and PCE.

5.4 Conclusions

We tuned the surface energy of TiO_x films by introducing C_{60} interlayers of varying thickness into PHJ perovskite solar cells to enhance their PCE. The surface energy of the C_{60} interlayer strongly affected the resulting device performance. The highest PCE was observed for the device fabricated with a 7-nm-thick C_{60} interlayer, which had a surface energy of 51.5 mJ m^{-2}. The C_{60} interlayer between the perovskite and TiO_x layers

increased the content of photogenerated charge carrier sites and lowered the accumulation and trapping of photogenerated charges at the TiO_x interface. These effects increased J_{sc}, FF and PCE of the cells containing a C_{60} interlayer compared with those of solar cells without an interlayer. The maximum PCE of 9.51 % for the device with a 7-nm-thick C_{60} interlayer can be attributed to its low series resistance caused by better energy level alignment with the contacts, which lowered the interfacial barrier.

<This page is intentionally left blank to indicate the chapter break>

References

1. J. Newton, *Uncommon Friends: Life with Thomas Edison, Henry Ford, Harvey Firestone, Alexis Carrel, and Charles Lindbergh*, Mariner Books, Harcourt Brace Jovanovich, San Diego, CA, 1989.
2. M. A. Green, *Solar Cells: Operating Principles, Technology, and System Applications*, Prentice-Hall, Inc., Englewood Cliffs, New Jersey, 1982.
3. A. Luque, ed., *Handbook of Photovoltaic Science and Engineering*, John Wiley & Sons, Inc., 2010.
4. S. M. Sze, *John Wiley & Sons*, 1936, **Second edition** 790.
5. R. Kawano, H. Matsui, C. Matsuyama, A. Sato, M. A. B. H. Susan, N. Tanabe and M. Watanabe, *J. Photoch. Photobio. A*, 2004, **164**, 87-92.
6. H. J. Snaith, *J. Phys. Chem. Lett.*, 2013, **4**, 3623-3630.
7. Y.-C. Hsiao, T. Wu, M. Li, Q. Liu, W. Qin and B. Hu, *J. Mater. Chem. A*, 2015, **3**, 15372-15385.
8. J. M. Ball, S. D. Stranks, M. T. Horantner, S. Huttner, W. Zhang, E. J. W. Crossland, I. Ramirez, M. Riede, M. B. Johnston, R. H. Friend and H. J. Snaith, *Energ. Environ. Sci.*, 2015, **8**, 602-609.
9. D. Shi, V. Adinolfi, R. Comin, M. Yuan, E. Alarousu, A. Buin, Y. Chen, S. Hoogland, A. Rothenberger, K. Katsiev, Y. Losovyj, X. Zhang, P. A. Dowben, O. F. Mohammed, E. H. Sargent and O. M. Bakr, *Science*, 2015, **347**, 519-522.
10. G. Hodes, *Science*, 2013, **342**, 317-318.
11. A. Kojima, K. Teshima, Y. Shirai and T. Miyasaka, *J. Am. Chem. Soc.*, 2009, **131**, 6050-6051.
12. J.-H. Im, C.-R. Lee, J.-W. Lee, S.-W. Park and N.-G. Park, *Nanoscale*, 2011, **3**, 4088-4093.

13. H.-S. Kim, C.-R. Lee, J.-H. Im, K.-B. Lee, T. Moehl, A. Marchioro, S.-J. Moon, R. Humphry-Baker, J.-H. Yum, J. E. Moser, M. Grätzel and N.-G. Park, *Sci. Rep.*, 2012, **2**, 591.
14. M. M. Lee, J. Teuscher, T. Miyasaka, T. N. Murakami and H. J. Snaith, *Science*, 2012, **338**, 643-647.
15. J. H. Heo, S. H. Im, J. H. Noh, T. N. Mandal, C.-S. Lim, J. A. Chang, Y. H. Lee, H.-j. Kim, A. Sarkar, K. NazeeruddinMd, M. Gratzel and S. I. Seok, *Nat. Photon.*, 2013, **7**, 486-491.
16. J. H. Noh, S. H. Im, J. H. Heo, T. N. Mandal and S. I. Seok, *Nano Lett.*, 2013, **13**, 1764-1769.
17. J. Burschka, N. Pellet, S.-J. Moon, R. Humphry-Baker, P. Gao, M. K. Nazeeruddin and M. Grätzel, *Nature*, 2013, **499**, 316–319.
18. D. Liu and T. L. Kelly, *Nat. Photon.*, 2014, **8**, 133-138.
19. J. A. Christians, R. C. M. Fung and P. V. Kamat, *J. Am. Chem. Soc.*, 2014, **136**, 758-764.
20. S. Ye, W. Sun, Y. Li, W. Yan, H. Peng, Z. Bian, Z. Liu and C. Huang, *Nano Lett.*, 2015, **15**, 3723-3728.
21. J. T.-W. Wang, J. M. Ball, E. M. Barea, A. Abate, J. A. Alexander-Webber, J. Huang, M. Saliba, I. Mora-Sero, J. Bisquert, H. J. Snaith and R. J. Nicholas, *Nano Lett.*, 2014, **14**, 724-730.
22. K. Wojciechowski, M. Saliba, T. Leijtens, A. Abate and H. J. Snaith, *Energ Environ. Sci.*, 2014, **7**, 1142-1147.
23. H. Zhou, Q. Chen, G. Li, S. Luo, T.-b. Song, H.-S. Duan, Z. Hong, J. You, Y. Liu and Y. Yang, *Science*, 2014, **345**, 542-546.
24. Best Research-Cell Efficiencies., (accessed 2016).
25. R. F. Service, *Science*, 2014, **344**, 458-458.
26. S. r. spectrum, https://en.wikipedia.org/wiki/Solar_irradiance.

27. T. He, Q. Huang, A. P. Ramirez, Y. Wang, K. A. Regan, N. Rogado, M. A. Hayward, M. K. Haas, J. S. Slusky, K. Inumara, H. W. Zandbergen, N. P. Ong and R. J. Cava, *Nature*, 2001, **411**, 54–56.
28. S. Yasuhiro, F. Yoshiki, A. Hiromichi and S. Tetsuro, in *Fundamentals and Applications of Chemical Sensors*, American Chemical Society, 1986, vol. 309, pp. 83–100.
29. S. Tao and J. T. S. Irvine, *Nat. Mater.*, 2003, **2**, 320–323.
30. M. E. Lines and A. M. Glass, in *Principles and Applications of Ferroelectrics and Related Materials (Monographs on Physics)*, Clarendon Press, Oxford, England, 1977.
31. P. M. Rørvik, T. Grande and M.-A. Einarsrud, *Adv. Mater.*, 2011, **23**, 4007–4034.
32. H. Kato and A. Kudo, *J. Phys. Chem. B*, 2001, **105**, 4285–4292.
33. J. Suntivich, H. A. Gasteiger, N. Yabuuchi, H. Nakanishi, J. B. Goodenough and Y. Shao-Horn, *Nat. Chem.*, 2011, **3**, 546–550.
34. Y. Zhao, L. Xu, L. Mai, C. Han, Q. An, X. Xu, X. Liu and Q. Zhang, *P. Natl. Acad. Sci. USA*, 2012, **109**, 19569–19574.
35. L. Bocher, M. H. Aguirre, D. Logvinovich, A. Shkabko, R. Robert, M. Trottmann and A. Weidenkaff, *Inorg. Chem.*, 2008, **47**, 8077–8085.
36. M. C. Beard, J. M. Luther and A. J. Nozik, *Nat. Nanotechnol.*, 2014, **9**, 951–954.
37. Y. Mao, T.-J. Park and S. S. Wong, *Chem. Commun.*, 2005, DOI: 10.1039/B509960A, 5721–5735.
38. T. Ishihara, J. Takahashi and T. Goto, *Phys. Rev.*, 1990, **42**.
39. J. Calabrese, N. L. Jones, R. L. Harlow, N. Herron, D. L. Thorn and Y. Wang, *J. Am. Chem. Soc.*, 1991, **113**, 2328–2330.
40. S. Wang, D. B. Mitzi, C. A. Feild and A. Guloy, *J. Am. Chem. Soc.*, 1995, **117**, 5297–5302.
41. Y. Takeoka, K. Asai, M. Rikukawa and K. Sanui, *Chem. Lett.*, 2005, **34**, 602–603.
42. T. Yang, Z. D. Gordon and C. K. Chan, *Cryst. Growth Des.*, 2013, **13**, 3901–3907.

43. Z. Deng, Y. Dai, W. Chen, X. Pei and J. Liao, *Nanoscale Res. Lett.*, 2010, **5**, 1217–1221.

44. W. Dong, B. Li, Y. Li, X. Wang, L. An, C. Li, B. Chen, G. Wang and Z. Shi, *J. Phys. Chem. C*, 2011, **115**, 3918–3925.

45. N. C. Pramanik, S. I. Seok and B. Y. Ahn, *J. Colloid Interf. Sci.*, 2006, **300**, 569–576.

46. A. P. Bartlett, M. Pichumani, M. Giuliani, W. González−Viñas and A. Yethiraj, *Langmuir*, 2012, **28**, 3067–3070.

47. M. Shahiduzzaman, K. Yamamoto, Y. Furumoto, T. Kuwabara, K. Takahashi and T. Taima, *RSC Adv.*, 2015, **5**, 77495-77500.

48. S. Md, Y. Kohei, F. Yoshikazu, K. Takayuki, T. Kohshin and T. Tetsuya, *Jpn. J. Appl. Phys.*, 2016, **55**, 02BF05.

49. J.-H. Im, J. Luo, M. Franckevičius, N. Pellet, P. Gao, T. Moehl, S. M. Zakeeruddin, M. K. Nazeeruddin, M. Grätzel and N.-G. Park, *Nano Lett.*, 2015, **15**, 2120-2126.

50. L. C. Schmidt, A. Pertegás, S. González-Carrero, O. Malinkiewicz, S. Agouram, G. Mínguez Espallargas, H. J. Bolink, R. E. Galian and J. Pérez-Prieto, *J. Am. Chem. Soc.*, 2014, **136**, 850-853.

51. L. Sun, J. J. Choi, D. Stachnik, A. C. Bartnik, B.-R. Hyun, G. G. Malliaras, T. Hanrath and F. W. Wise, *Nat. Nano.*, 2012, **7**, 369-373.

52. A. Kojima, M. Ikegami, K. Teshima and T. Miyasaka, *Chem. Lett.*, 2012, **41**, 397-399.

53. E. Horváth, M. Spina, Z. Szekrényes, K. Kamarás, R. Gaal, D. Gachet and L. Forró, *Nano Lett.*, 2014, **14**, 6761–6766.

54. S. T. Ha, X. Liu, Q. Zhang, D. Giovanni, T. C. Sum and Q. Xiong, *Adv. Opt. Mater.*, 2014, **2**, 838-844.

55. M. I. B. Utama, M. d. l. Mata, C. Magen, J. Arbiol and Q. Xiong, *Adv. Funct. Mater.*, 2013, **23**, 1636-1646.

56. M. I. B. Utama, Z. Peng, R. Chen, B. Peng, X. Xu, Y. Dong, L. M. Wong, S. Wang, H. Sun and Q. Xiong, *Nano Lett.*, 2011, **11**, 3051-3057.
57. M. Gillet, R. Delamare and E. Gillet, *J. Cryst. Growth.*, 2005, **279**, 93-99.
58. J. Y. Jeng, Y. F. Chiang, M. H. Lee, S. R. Peng, T. F. Guo, P. Chen and T. C. Wen, *Adv. Mater.*, 2013, **25**, 3727-3732.
59. P.-W. Liang, C.-Y. Liao, C.-C. Chueh, F. Zuo, S. T. Williams, X.-K. Xin, J. Lin and A. K. Y. Jen, *Adv. Mater.*, 2014, **26**, 3748–3754.
60. P. Docampo, J. M. Ball, M. Darwich, G. E. Eperon and H. J. Snaith, *Nat. Commun.*, 2013, **4**, 2761.
61. T. Kuwabara, H. Sugiyama, M. Kuzuba, T. Yamaguchi and K. Takahashi, *Org. Electron.*, 2010, **11**, 1136–1140.
62. K. Yamamoto, Y. Zhou, K. T, K. Takahashi and T. Taima, presented in part at the Photovoltaic Specialist Conference (PVSC), 2014 IEEE 40th, Denver, CO, 8-13 June, 2014.
63. A. Wakamiya, M. Endo, T. Sasamori, N. Tokitoh, Y. Ogomi, S. Hayase and Y. Murata, *Chem. Lett.*, 2014, **43**, 711-713.
64. A. Dualeh, T. Moehl, N. Tétreault, J. Teuscher, P. Gao, M. K. Nazeeruddin and M. Grätzel, *ACS Nano*, 2014, **8**, 362-373.
65. M. Xiao, F. Huang, W. Huang, Y. Dkhissi, Y. Zhu, J. Etheridge, A. Gray-Weale, U. Bach, Y.-B. Cheng and L. Spiccia, *Angew. Chem.*, 2014, **53**, 9898–9903.
66. A. Dualeh, N. Tétreault, T. Moehl, P. Gao, M. K. Nazeeruddin and M. Grätzel, *Adv. Funct. Mater.*, 2014, **24**, 3250-3258.
67. G. E. Eperon, V. M. Burlakov, P. Docampo, A. Goriely and H. J. Snaith, *Adv. Funct. Mater.*, 2014, **24**, 151-157.
68. Q. Chen, H. Zhou, Z. Hong, S. Luo, H.-S. Duan, H.-H. Wang, Y. Liu, G. Li and Y. Yang, *J. Am. Chem. Soc.*, 2013, **136**, 622–625.
69. A. A. Ayi, C. A. Anyama and S. S. Etuk, *J. Appl. Chem.*, 2014, **2**, 26–32.
70. Y.-J. Jeon, S. Lee, R. Kang, J.-E. Kim, J.-S. Yeo, S.-H. Lee, S.-S. Kim, J.-M. Yun and D.-Y. Kim, *Sci. Rep.*, 2014, **4**, 6953.

71. C.-C. Chen, Z. Hong, G. Li, Q. Chen, H. Zhou and Y. Yang, *J. Photon. Energy*, 2015, **5**, 057405-057405.

72. N. J. Jeon, J. H. Noh, Y. C. Kim, W. S. Yang, S. Ryu and S. I. Seok, *Nat. Mater.*, 2014, **13**, 897-903.

73. K. R. Seddon, *Nat. Mater.*, 2003, **2**, 363-365.

74. G. Niu, X. Guo and L. Wang, *J. Mater. Chem. A*, 2015, DOI: 10.1039/C4TA04994B, 8970-8980.

75. H.-S. Kim, C.-R. Lee, J.-H. Im, K.-B. Lee, T. Moehl, A. Marchioro, S.-J. Moon, R. Humphry-Baker, J.-H. Yum, J. E. Moser, M. Gratzel and N.-G. Park, *Sci. Rep.*, 2012, **2**, 591-597.

76. J. You, Z. Hong, Y. Yang, Q. Chen, M. Cai, T.-B. Song, C.-C. Chen, S. Lu, Y. Liu, H. Zhou and Y. Yang, *ACS Nano*, 2014, **8**, 1674-1680.

77. X. Duan, J. Lian, J. Ma, T. Kim and W. Zheng, *Cryst. Growth Des.*, 2010, **10**, 4449-4455.

78. Q. Chen, H. Zhou, Z. Hong, S. Luo, H. S. Duan, H. H. Wang, Y. Liu, G. Li and Y. Yang, *J. Am. Chem. Soc.*, 2014, **136**, 622-625.

79. L. Wu, J. Lian, G. Sun, X. Kong and W. Zheng, *Eur. J. Inorg. Chem.*, 2009, **2009**, 2897-2900.

80. R. E. Cohen, *J. Phys. Chem. Solids*, 2000, **61**, 139-146.

81. A. Nan and J. Liebscher, *Ionic Liquids as Advantageous Solvents for Preparation of Nanostructures*, INTECH Open Access Publisher, 2011.

82. M. Shahiduzzaman, K. Yamamoto, Y. Furumoto, T. Kuwabara, K. Takahashi and T. Taima, *Chem. Lett.*, 2015, **44**, 1735-1737.

83. Q. Wang, Y. Shao, Q. Dong, Z. Xiao, Y. Yuan and J. Huang, *Energ Environ. Sci.*, 2014, **7**, 2359-2365.

84. J. S. Kim, J. H. Park, J. H. Lee, J. Jo, D.-Y. Kim and K. Cho, *.Appl. Phys. Lett.*, 2007, **91**, 112111.

85. M. Liu, M. B. Johnston and H. J. Snaith, *Nature*, 2013, **501**, 395-398.

Appendix II

for

Ionic liquid-assisted growth of methylammonium lead iodide spherical nanoparticles by a simple spin-coating method and photovoltaic properties of perovskite solar cells

2.1. Crystalline size calculated from Scherrer Equation

Scherer equation relating the crystalline size and broadening of the XRD peak:

$$D_{XRD} = (K\times \lambda)/(\beta \cos \theta/2) \qquad \text{(Eq. A2.1)}$$

Where d (nm) is the mean size of the crytalline domain (crystalline size) of the nanoparticles, K is the constant crystalline shape factor (dimentionless) which has the typical value of 0.9 (its depend on the shape of nanoparticles), λ (nm) is the X-ray wavelength, β (rad) is the full peak width at half maximum intensity (FWHM) and θ (rad) is the peak possition (Bragg angle). K = 0.9 and λ = 0.154 nm were used to calculate the mean crystalline size (d) of the nanoparticles.

2.2. Peak parameters of perovskites

Table A2.1. Peak parameters used to calculate the mean crystalline size in films formed with and without IL using the Scherrer formula.

Parameter	Perovskite films	
	With IL	Without IL
FWHM (B)	0.2401	0.2227
Bragg Angle (θ) Primary peak	14.01	14.08
X-ray wavelength (λ)	1.54	1.54
Constant (K)	0.9	0.9
D_{XRD} (nm)	35.8	37.5

Appendix V

for

Enhanced photovoltaic performance of perovskite solar cells *via* modification of surface characteristics using a fullerene interlayer

5.1. Investigation of the effect of C_{60} with DMF solvent in term of morphology of the resultant C_{60} layer.

We investigated the effect of C_{60} with DMF solvent in term of morphology of the resultant C_{60} layer. The C_{60} layer were first deposited on glass substrates. The C_{60} films were then spin coating in a DMF solution. The atomic force microscopy (AFM) image in Fig. A5.1. reveals that a uniformly distributed, C_{60} layer was stably remained after DMF solvent treatment. That means the C_{60} layer cannot be removed after spin coating of the perovskite solution.

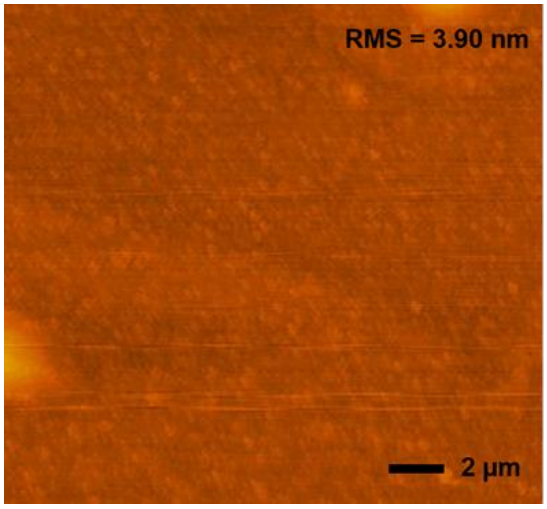

Figure A5.1. AFM image of C_{60} film treatment by DMF solvent.

5.2. SEM image of perovskite

Figure A5.2. reveals that the films processed without C_{60} have incomplete surface coverage, and are composed of non-uniform large crystals with a discrete shape. These observations are similar to those in a previous report by Xiao *et al.*,[65] which confirms that the non-uniformity in the perovskite film was caused by the rapid evaporation of DMF during spin coating.

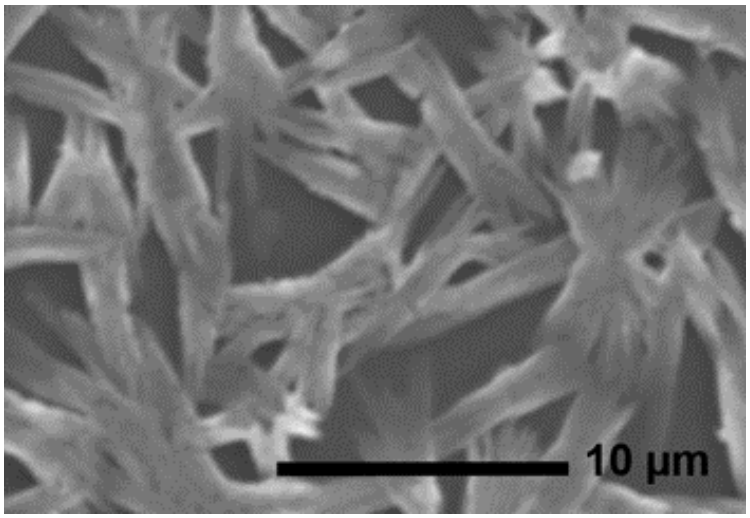

Figure A5.2. SEM images of $TiO_x/CH_3NH_3PbI_3$ film.

5.3. Calculations of surface energy

Table A5.1. Equations for the calculation of surface energy

Young-Dupre equation

$$W_{SL} = \gamma_L(1 + cos\theta) \quad \text{..... (I)}$$

In acid-base theory, the work of adhesion is defined by the following equations,

$$W_{SL} = 2\sqrt{\gamma_S^{LW}\gamma_L^{LW}} + 2\sqrt{\gamma_S^{+}\gamma_S^{-}} + 2\sqrt{\gamma_S^{-}\gamma_S^{+}} = \gamma_L(1+\cos\theta) \quad \text{(II)}$$

Where,

W_{SL} = Work over adhesion

LW = Lifshitz-van der waals component (Non-polar interaction)

AB = Acid-Base component (polar interaction)

γ_S^{total} = Surface energy

$$\gamma_S^{AB} = 2\sqrt{\gamma_S^{+}\gamma_S^{-}}$$

$$\gamma_S^{total} = \gamma_S^{LW} + \gamma_S^{AB}$$

<This page is intentionally left blank to indicate the chapter break>

APPENDIX A: LIST OF PUBLICATIONS

A list of the accomplished research reports (published, accepted or presented) under the supervision of Dr. Tetsuya Taima during my doctoral course tenure (October, 2013–September, 2016) in the Kanazawa University, Japan is compiled in this section.

JOURNAL ARTICLES

1) Kouhei Yamamoto, Yoshikazu Furumoto, Md. Shahiduzzaman, Takyuki Kuwabara, Kohshin Takahashi and Tetsuya Taima*, Degradation mechanism for planar heterojunction perovskite solar cells, *Japanese Journal of Applied Physics, Vol. 55,* pp. 04ES07-4, March, 2016.
2) Md. Shahiduzzaman*, Kohei Yamamoto, Yoshikazu Furumoto, Takayuki Kuwabara, Kohshin Takahashi and Tetsuya Taima*, Shape-controlled $CH_3NH_3PbI_3$ nanoparticles for planar heterojunction perovskite solar cells, *Japanese Journal of Applied Physics, Vol. 55,* pp. 02BF05-7, January, 2016.
3) Md. Shahiduzzaman*, Kohei Yamamoto, Yoshikazu Furumoto, Takayuki Kuwabara, Kohshin Takahashi, and Tetsuya Taima*, Enhanced photovoltaic performance of perovskite solar cells via modification of surface characteristics using a fullerene interlayer, *Chemistry. Letters*, Vol. 44, No. 12, pp. 1735-1737, December, 2015.
4) M. Shahiduzzaman*, Kohei Yamamoto, Yoshikazu Furumoto, Takayuki Kuwabara, Kohshin Takahashi, and Tetsuya Taima*, Ionic liquid-assisted growth of methylammonium lead iodide spherical nanoparticles by a simple spin-coating method and photovoltaic properties of perovskite solar cells, *RSC advances*, Vol. 5, pp. 77495-77500, September, 2015.

[*] represents the corresponding author.

JAPANESE PATENT

1) 當摩, モハマド　シャヒドゥザマン (**Md. Shahiduzzaman**), 山本, 微粒子化ペロブスカイト膜及びそれを用いた機能性素子; *In English*: (*Nanoparticles of perovskite and its application to electric devices)*" 特願, 2015-110392.

PROCEEDINGS

1) Tetsuya Taima*, M. Shahiduzzaman*, Kohei Yamamoto, Yoshikazu Furumoto, Takayuki Kuwabara, and Kohshin Takahashi, "Planer heterojunction type perovskite solar cells based on TiOx compact layer fabricated by chemical bath deposition", Proc. of SPIE Vol. 9749, Oxide-based Materials and Devices VII, 97491G-1(February 27, 2016); doi:10.1117/12.2217737.
2) Md. Shahiduzzaman*, Kohei Yamamoto, Yoshikazu Furumoto, Takayuki Kuwabara, Kohshin Takahashi and Tetsuya Taima*, "Shape-Controlled Preparation of MAPbI3 Nanoparticles by Ionic Liquid-Assisted Simple Spin-coating Method with Tunable Optical Absorption", SSDM 2015, Sapporo, JAPAN/ Sep, 2015, pp. 528.
3) Kouhei Yamamoto, Md. Shahiduzzaman, Yoshikazu Furumoto, Takyuki Kuwabara, Kohshin Takahashi and Tetsuya Taima*, "Degradation mechanism for Planar Heterojunction Perovskite Solar Cells", SSDM 2015, Sapporo, JAPAN/ Sep, 2015, pp. 658.
4) Md. Shahiduzzaman*, K. Yamamoto, Y. Furumoto, Takayuki Kuwabara, Kohshin Takahashi, Tetsuya Taima*, "Ionic Liquid-Assisted Growth for Spherical Nanoparticles of Methylammonium Lead Iodide (MAPbI3) by Simple Spin Coating Method", EM-NANO 2015, Toki Mesi, JAPAN/ June, 2015, pp. 58.

CONFERENCE PAPERS

1) Md. Shahiduzzaman, Kohei. Yamamoto, Yoshikazu. Furumoto, Takayuki Kuwabara, Kohshin Takahashi, Tetsuya Taima, "Fabrication, Characterization and Photovoltaic Properties of $CH_3NH_3PbI_3$ nanoparticles", Solid State Devices and Materials (SSDM) 2016, Tsukuba, JAPAN/ Sep, 2016.

2) Kyosuke Yonezawa, Kohei. Yamamoto, Md. Shahiduzzaman, Yoshikazu. Furumoto, Keitarou Hamada, Teresa S. Ripolles, Takayuki Kuwabara, Kohshin Takahashi, Shuzi Hayase, Tetsuya Taima, "Planar Heterojunction-type Inorganic

$CsPbI_3$ Perovskite Solar Cells Using Evaporation Method", Kanazawa Univ. 2016, Kanazawa, JAPAN/ July, 2016.

3) Kohei Nojiri, Md. Shahiduzzaman, Kohei. Yamamoto, Yoshikazu. Furumoto, Takayuki Kuwabara, Kohshin Takahashi, Tetsuya Taima, "Interpenetrating Heterojunction Photovoltaic Cells Based on C_{60} Nano-Crystallized Thin Films", Organic Molecular Electronics (ISOME) 2016, Nigata, JAPAN/ May, 2016.
4) Md. Shahiduzzaman, Kohei. Yamamoto, Yoshikazu. Furumoto, Takayuki Kuwabara, Kohshin Takahashi, Tetsuya Taima, "$CH_3NH_3PbI_3$ Nanoparticles: Chemical Approach towards Controllable Shape and their Photovoltaic Properties", 2016 E-MRS Spring Meeting, Lille, France/ May, 2016.
5) Tetsuya Taima, M. Shahiduzzaman, Kohei Yamamoto, Yoshikazu Furumoto, Takayuki Kuwabara, and Kohshin Takahashi, "Planer heterojunction type perovskite solar cells based on TiO_x compact layer fabricated by chemical bath deposition", SPIE photonics west, San Francisco, USA/Feb, 2016. (***Invited talk has been given by M. Shahiduzzaman***)
6) Kouhei Yamamoto, Md. Shahiduzzaman, Yoshikazu Furumoto, Takyuki Kuwabara, Kohshin Takahashi and Tetsuya Taima, "Planar Heterojunction Perovskite Solar Cells using Vapor sequential depositions method in term of Low Cost and High Stability", Pacifichem 2015, Hawaii, USA/ Dec, 2015.
7) Md. Shahiduzzaman, Kohei. Yamamoto, Yoshikazu. Furumoto, Takayuki Kuwabara, Kohshin Takahashi, Tetsuya Taima, "Enhanced Photovoltaic Performance of Planar Heterojunction Perovskite Solar Cells via Insertion of a Fullerene Interlayer", 2015 MRS Fall Meeting & Exhibit, Boston, USA/ Nov, 2015.
8) Md. Shahiduzzaman, Takayuki Kuwabara, Kohshin Takahashi and Tetsuya Taima, "Growth of $CH_3NH_3PbI_3$ Nanoparticles with Controllable Shape and Photovoltaic Properties of Perovskite Solar Cells", 3rd RSET symposium, Kanazawa, JAPAN/ Nov, 2015.
9) Md. Shahiduzzaman, Kohei Yamamoto, Yoshikazu Furumoto, Takayuki Kuwabara, Kohshin Takahashi and Tetsuya Taima, "Shape-Controlled

Preparation of $MAPbI_3$ Nanoparticles by Ionic Liquid-Assisted Simple Spin-coating Method with Tunable Optical Absorption", Solid State Devices and Materials (SSDM) 2015, Sapporo, JAPAN/ Sep, 2015.

10) Kouhei Yamamoto, Md. Shahiduzzaman, Yoshikazu Furumoto, Takyuki Kuwabara, Kohshin Takahashi and Tetsuya Taima, "Degradation mechanism for Planar Heterojunction Perovskite Solar Cells", Solid State Devices and Materials (SSDM) 2015, Sapporo, JAPAN/ Sep, 2015.
11) Md. Shahiduzzaman, Kohei Yamamoto, Yoshikazu Furumoto, Takayuki Kuwabara, Kohshin Takahashi and Tetsuya Taima, "Shape-Controlled $CH_3NH_3PbI_3$ Nanoparticles for Planar Heterojunction Perovskite Solar Cells", JSAP Autumn meeting 2015, Nagoya, JAPAN/ Sep, 2015.
12) Md. Shahiduzzaman, K. Yamamoto, Y. Furumoto, Takayuki Kuwabara, Kohshin Takahashi, Tetsuya Taima, "Ionic Liquid-Assisted Growth for Spherical Nanoparticles of Methylammonium Lead Iodide ($MAPbI_3$) by Simple Spin Coating Method", EM-NANO 2015, Toki Mesi, JAPAN/ June, 2015.
13) Tham Adhikari, Jean-Michel Nunzi, Olivier Lebel, Md. Shahiduzzaman, Tetsuya Taima, "Novel Materials for Fabrication and development of Photovoltaic Devices", Annual forum on Material Chemistry 2015, Queen's University, CANADA/April, 2015.
14) Tham Adhikari, Jean-Michel Nunzi, Olivier Lebel, Md. Shahiduzzaman, Tetsuya Taima, "Dual Light Absorption in Perylene diimide-glass /Organometallic Halide Composite Thin Film", Annual forum on Material Chemistry 2015, Queen's University, CANADA/April, 2015.